Use of X-ray Absorption Spectrometry to Determine Diffusion Coefficients in Low-Permeability Shale:

Queenston Formation Shale

Golrokh Hafezian

Thesis submitted to the University of Ottawa
in partial Fulfillment of the requirements for the
Master's degree in Earth and Environmental Sciences

Department of Earth and Environmental Sciences

Faculty of Science

University of Ottawa

Abstract

A new spectrometric technique for measuring diffusion coefficients of Ordovician Queenston Formation shale from the Michigan Basin of southwest Ontario, Canada is presented; in this case pore diffusion coefficients (D_p) were determined for the conservative (iodide, I^-) and reactive (cesium, Cs^+) tracers in porous media. Furthermore, diffusion-reaction parameters such as Cation exchange capacity (CEC) were obtained for the reactive tracer, Cs^+ by the reactive-transport modeling.

The principle of X-ray absorption spectrometry (XAS) is based on the attenuation of high atomic number of diffusive species (e.g. $Cs^+$and I^-) in porous media, allowing for the quantification of the resulting spatial changes. The technique employs a 1.1 mm collimated X-ray beam to resolve the tracer presence in a slice; small region of a rotating sample for a fixed time.

The x-ray beam is incident on a sample of porous rock while the transmitted beam is detected on the opposite side of the sample, allowing acquisition of a transmitted X-ray energy spectrum vs intensity (counts).

Additional analyses such as mineralogical studies by scanning electron microscopy with energy dispersive X-ray spectroscopy (SEM-EDS) were conducted to improve the understanding of solute transport.

The comparison of the data obtained by the XAS method indicating a good agreement with established radiography and other conventional diffusion methods provide an alternate approach for quantifying diffusion coefficient of porous media.

Acknowledgments

I would like to express my sincere gratitude to my supervisor, Dr. Tom Al. This work could not happen without his continuous support and guidance as well as his valuable advice throughout the project. His feedback and guidance helped me for the entire research time and during the writing of my thesis.

I was pleased to be working with smart and hardworking researcher, Samuel Morfin, who I would like to thank for the time, energy, and support he provided to me through the entire project. His patience and determination helped me achieve all necessary research skills regarding the laboratory works. I also would like to express my gratitude to the other members of the lab namely Dominique Bower for the comradery of this journey.

Thanks to the Master's Scholarship from the NWMO which I received. This financial support was extremely helpful to complete my study.

Thanks to my old friends, Hamed and Ramina. Your friendship, energy and support has made my time at Ottawa some of the best years of my life. I wish you all the very best.

Finally, my special thanks go to my wonderful parents for their unstoppable love and support as well as my lovely brother, Amir Mahdi who always have supported me in this path.

Table of Contents

List of Tables

List of Figures

CHAPTER 1 – Introduction

Some of the radioactive components in spent nuclear fuel are soluble, thus if released into the environment, they can be transported in groundwater. Therefore, several countries plan to dispose of radioactive waste in a deep geologic repository (DGR), where low-permeability rocks can provide an effective barrier against solute migration. The principal mechanisms that control this migration are advection and diffusion. Advection tends to take place in locations with relatively high permeability, while diffusive transport dominates low permeability systems, e.g. clay-rich sedimentary rocks (Croisé et al., 2004; Oscarson et al., 1990; Tidwell et al., 2000; Van Brakel and Heertjes, 1974; Van Loon et al., 2003).

Diffusion and advection behavior in sedimentary rocks have been investigated in both field and laboratory experiments (Feenstra et al., 1984; Foster, 1975; Hendry et al., 2009; Hölttä et al., 1996; Palut et al., 2003; Tevissen et al., 2004; Tidwell et al., 2000; Wersin et al., 2008; Young and Ball, 1998). Similarly, mathematical models have been developed to simulate transport in saturated rocks, where transport is affected by both advection and matrix diffusion. The results of model simulations indicate that rocks with diffusion-dominated transport have a considerable capacity for isolating radioactive contaminants. For this reason, low-permeability rocks have received wide attention in the context of isolating radioactive waste.(Boving and Grathwohl, 2001; Patera et al., 1990).

Studies (Garcıa-Gutiérrez et al., 2001; Jakob et al., 2009) have indicated that the transport properties or behavior of diffusing species within pore media depend on the charge, ionic radius, and hydration energy. These determine the tendency toward conservative (non-reactive with minerals surfaces) or reactive (reactive with minerals surfaces) properties of solutes during transport, thereby affecting the rate of transport. Conservative tracers (e.g. isotopes of H and O on the water molecule such as deuterium, HDO, tritium, HTO, and H218O; and anionic tracers such as Cl^-, Br^- and I^-, and reactive tracers (e.g. Cs^+ and Sr^{+2}) are commonly used in through-diffusion (Garcıa-Gutiérrez et al., 2001; Gurumoorthy and Singh, 2004; Oscarson et al., 1992; Savoye et al., 2010; Van Loon et al., 2003; Van Loon et al., 2007; Xiang et al., 2016; Xiang et al., 2013) , in-

diffusion (Boving and Grathwohl, 2001; Cave et al., 2009; Cormenzana et al., 2003; Garcıa-Gutiérrez et al., 2001; Nunn et al., 2018; Oscarson et al., 1992), and out-diffusion experiments (Sardini et al., 2003; Van Loon et al., 2007; Waber and Smellie, 2008).

Parameters measured from these experiments include the effective diffusion coefficient (D_e), tracer-accessible porosity (ϕ_{tr}), tortuosity factor (τ_f) and the pore diffusion coefficient (D_p). The transport of reactive species is relatively slow because they are attenuated by reaction processes, such as ion exchange, precipitation and dissolution, and surface complexation; all of which may be influenced by changing redox conditions (Fuller et al., 2014; Fuller et al., 2015; Garcıa-Gutiérrez et al., 2001; Oscarson et al., 1994; Steefel et al., 2003; Tachi et al., 2011).

X-ray absorption techniques can provide unique insights into temporal and spatial variations of solute diffusion that cannot be obtained from conventional techniques such as through-diffusion which generally provide an estimate of the bulk, or whole-sample properties. Radiography (Cave et al., 2009; Loomer et al., 2013), X-ray computed tomography (Agbogun et al., 2013a; Agbogun et al., 2013b; Clausnitzer and Hopmans, 2000; Cnudde and Boone, 2013), and synchrotron-source X-ray computed microtomography (Altman et al., 2005; Flannery et al., 1987) techniques are the most commonly used X-ray absorption methods for characterizing diffusion properties of rocks (Altman et al., 2004; Cave et al., 2009; Loomer et al., 2013). However, most of these methods are subject to beam-hardening artifacts, because the X-ray sources are characterized by a wide range of photon energies (Ketcham and Carlson, 2001). These artifacts can be mistakenly interpreted as variations in sample properties. X-ray absorption spectrometry has not been employed up until now for rock diffusion studies, but it offers the advantage that measurements can be conducted in a specific photon energy range, and should therefore avoid beam-hardening artifacts.

1.1. Background

1.1.1. Solute transport in saturated porous media

Diffusive transport in a saturated porous medium at steady state is explained by Fick's first law (Fig. 1.1):

$$J_i = -D(\frac{dC}{dx_i}) \quad (1.1)$$

Where:

J_i = mass flux of solute in the i direction (mol m^{-2} s^{-1})

D = diffusion coefficient ($m^2 s^{-1}$)

C = solute concentration (mol m^{-3})

dC/dx_i = concentration gradient with respect to the i coordinate direction (mol m^{-3} m^{-1})

i = spatial coordinate x, y or z.

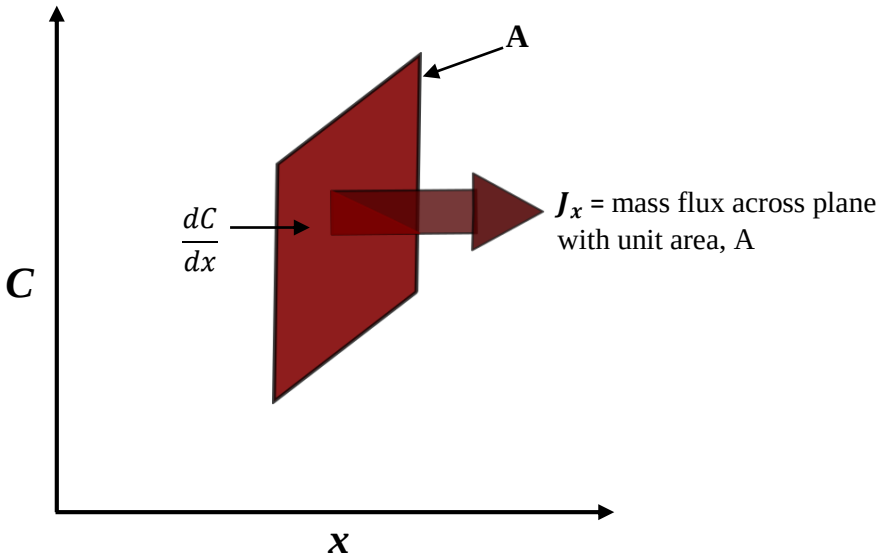

Figure 1.1. The diffusion flux in direction x across plane

In the case of steady-state conditions, the concentration gradient is linear, but that condition is preceded by a non-steady period during which the gradient is non-linear and continuously changing as shown in Figure 1.2. In this case, the solute mass flux can be represented by Fick's second law (Fetter et al., 2017):

$$\frac{\partial C}{\partial t} = D\frac{\partial^2 C}{\partial x^2} \tag{1.2}$$

Where:

t = represents time.

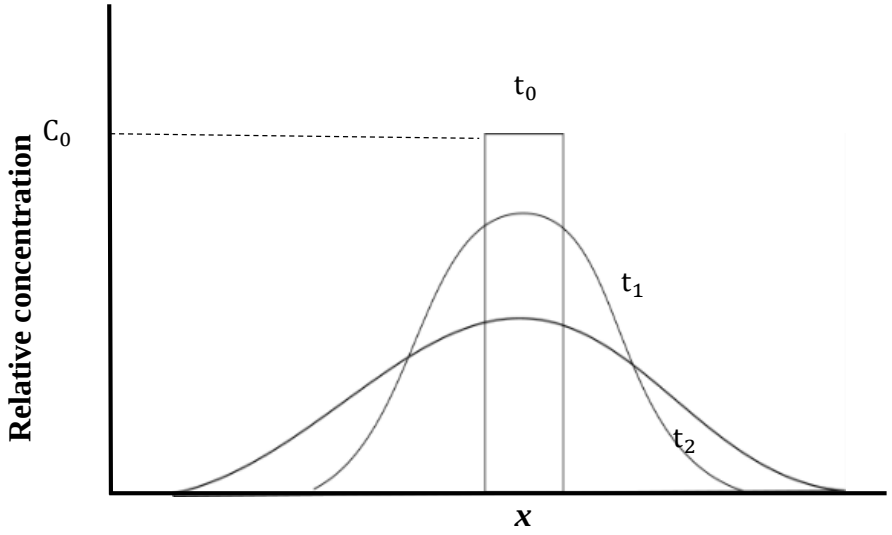

Figure 1.2. Evolution of solute distribution by diffusion with initial concentration of C_0 at time t_0 (modified from Fetter et al. (2017)).

The definition of D requires some refinement. In contrast to diffusion in free water, diffusive transport of a conservative solute in saturated porous media occurs within pore spaces where solutes must follow available pathways of length, Le that are generally longer than a straight-line path of length, L. To account for this in Fick's laws, the free-water diffusion coefficient (D_0) is multiplied by a tortuosity factor (τ_f), which is the ratio of constrictivity (δ) to tortuosity (τ) (Van Brakel and Heertjes, 1974). The product is defined as the pore diffusion coefficient (D_p):

$$D_P = D_0 \cdot \tau_f \quad (1.3)$$

where:

D_P and D_0 have units of $[m^2 s^{-1}]$

$\tau_f = {}^{\delta}/_{\tau}$; $0 < \tau_f \leq 1$

$\tau = \left({}^{L_e}/_{L}\right)^2$

$\delta =$ is a geometric factor that accounts for the effects of constricted pathways along the diffusive path in the pore space.

In addition to the effect of τ, diffusive transport of a conservative solute in saturated porous media is also affected by variations in the total connected pore volume, or porosity (ϕ). This is taken into account by multiplying D_p by the solute - or tracer-accessible porosity (ϕ_{tr}), giving the effective diffusion coefficient (D_e):

$$D_e = \phi_{tr} \cdot D_0 \cdot \tau_f = \phi_{tr} \cdot D_p \quad (1.4)$$

When the diffusing solutes are not influenced by size/ion exclusion in porous media; $\phi_{tr} \approx \phi$.

In the case of reactive solutes, the solute mass balance is a combination of the dissolved and adsorbed/precipitated mass which is accounted for with the rock capacity factor, α. The ratio D_e to α defines the apparent diffusion coefficient (D_a) which accounts for diffusion and retardation due to reaction processes.

$$D_a = {}^{D_e}/_{\alpha} \quad (1.5)$$

The rock capacity factor is defined by (Bradbury and Green, 1985) as follows:

$$\alpha = \phi_{tr} + \rho_b \cdot K_d \quad (1.6)$$

where:

ρ_b = bulk density of porous medium [kg m^{-3}]

K_d = distribution coefficient [$m^3 kg^{-1}$].

Values for K_d are determined experimentally, and then included in reactive-transport simulations of solute transport (Jakob et al., 2009; Maes et al., 2008; Melkior et al., 2005; Oscarson et al., 1994). The α term can be incorporated into Fick's second law (Vilks and Miller, 2007) to describe concentration variations due to diffusion as a function of space and time within a porous medium:

$$\frac{\partial C}{\partial t} = \frac{D_e}{\alpha} \cdot \frac{\partial^2 C}{\partial x^2} \quad (1.7)$$

The attenuation of transport rates by reaction processes is referred to as retardation, which is commonly quantified by a retardation factor, R_f (Bradbury and Green, 1985):

$$R_f = 1 + (\rho_b / \phi) \cdot K_d \quad (1.8)$$

Alternatively, retardation may be quantified in reactive-transport codes using a mass-action approach. This explicitly accounts for mass transfers between the aqueous and solid phase, using equilibrium constants or selectivity coefficients (Mayer, 1999; Parkhurst and Appelo, 2013; Steefel et al., 2015; Van Loon et al., 2009; Zachara et al., 2002).

1.1.2. X-ray absorption

An X-ray source utilizes a high-voltage (V_s) electrical field between a cathode and anode to accelerate electrons across the cathode-anode gap, causing electrons to reach high speeds before contacting the anode, which is referred to as the target (commonly tungsten). When electrons collide with the anode, X-rays are generated in two ways (Fig. 1.3). Bremsstrahlung radiation (German term for "braking radiation") occurs when electrons approach atomic nuclei in the anode

and they are decelerated. Bremsstrahlung radiation is emitted in a continuum up to a maximum energy which is defined by V_s. Characteristic X-rays are generated when the accelerated electrons collide with and eject shell electrons from the anode material, creating electron vacancies. These vacancies are filled by outer-shell electrons, simultaneously producing X-rays with energies that are equal to the energy difference between the higher and lower energy shells and therefore characteristic of the anode material (Clausnitzer and Hopmans, 2000; Wildenschild et al., 2002).

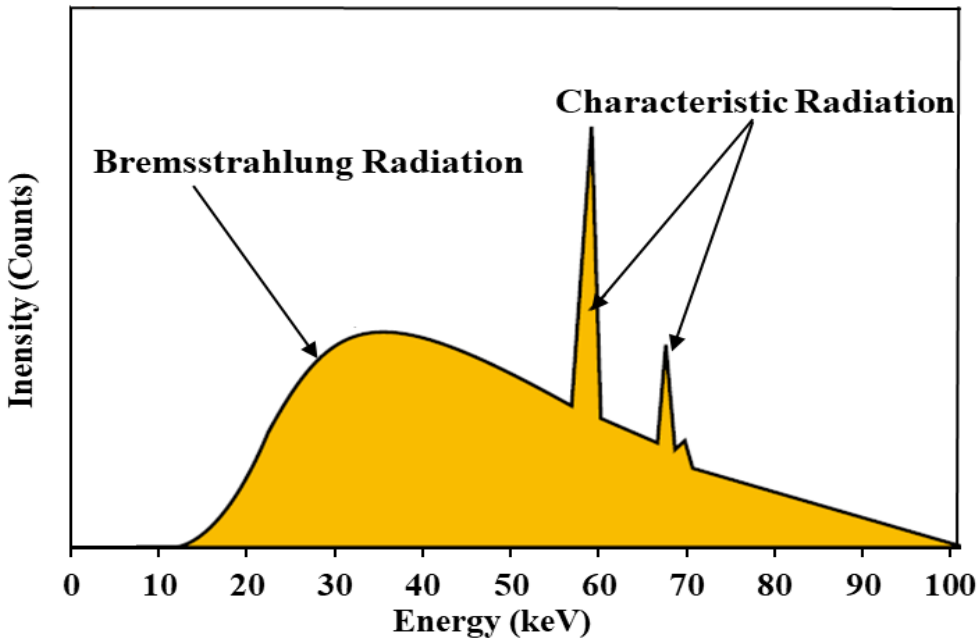

Figure 1.3. Example of Tungsten X-ray energy spectrum showing bremsstrahlung and characteristic radiations (Beyzadeoglu et al., 2010)

1.1.2.1 Principle of X-ray Absorption Spectroscopy (XAS)

Attenuation of X-rays as a result of scattering and absorption can be mathematically calculated by the Beer - Lambert law:

$$I_{(E)} = I_{0\ (E)}\, exp(-\mu_{(E)} d) \qquad (1.9)$$

where:

I_0 = incident intensity

I = measured intensity

d = material thickness [L]

E = X-ray energy [keV]

μ = linear attenuation coefficient of the material [L^{-1}].

As the X-ray beam travels through a material, a portion of the incident beam is absorbed or scattered out of the beam path, and the intensity measured at the detector after transmission through the sample is therefore lower than the incident intensity. Values of μ are a function of bulk density and electron density (closely related to effective atomic number) of the material, and the energy of the radiation (Ketcham, 2005). There are two principal mechanisms of X-ray attenuation that apply to this work, photoelectric absorption and Compton scattering. The photoelectric effect is the dominant attenuation mechanism at low X-ray energies (less than 50-100 keV) and μ increases with the atomic number of the absorbing material (Ketcham and Carlson, 2001) so photoelectric absorption provides compositional information about the material. In contrast, Compton scattering is less sensitive to atomic number and it is effective at energies greater than 50-100 keV and up to 5-10 MeV.

Figure 1.4 displays linear attenuation coefficients for Si, Ca, I and Cs as a function of X-ray photon energy. It is evident that each element has a characteristic K-shell absorption edge, with

the energy of the absorption edges varying systematically with the atomic number. The core- or K-shell electron binding energies increase with atomic number, which is why they display distinct absorption edges versus energy. These distinctive absorption edges, and the variations in the magnitude of μ versus atomic number, are the properties of photoelectric absorption that allow for differentiating elemental compositions by X-ray absorption.

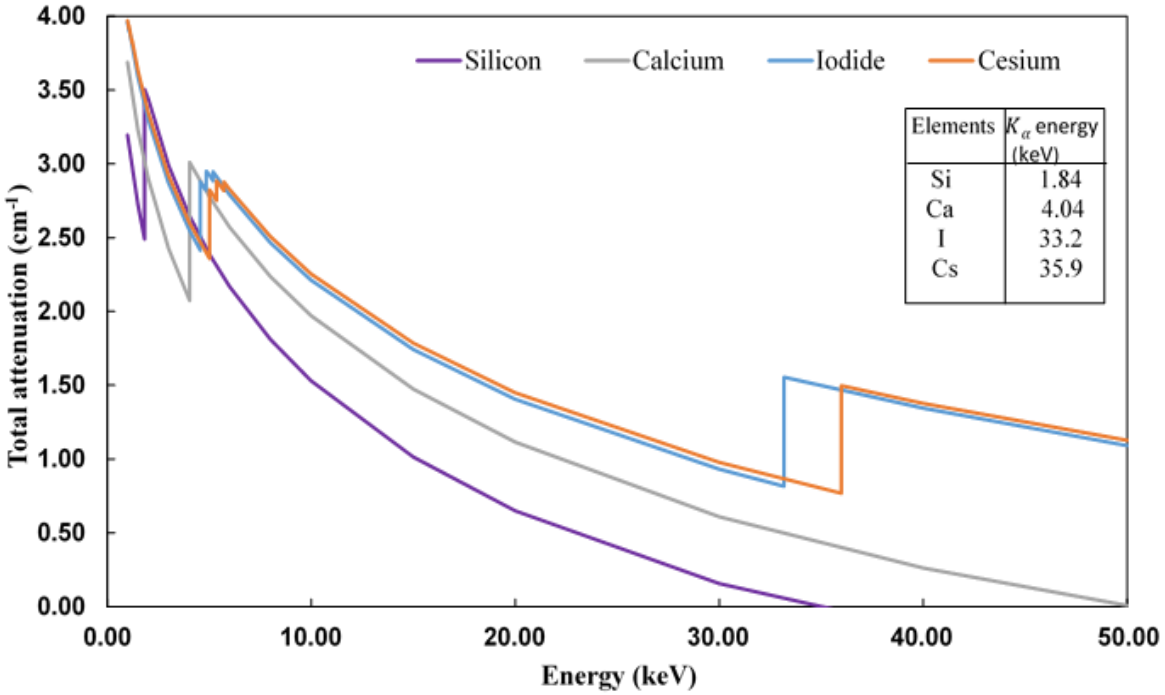

Figure 1.4. Linear attenuation coefficients as a function of X-ray energy for Si, Ca, I and Cs.

1.2. Objectives

The purpose of this study is to develop the novel X-ray absorption spectrometry technique to measure tracer diffusion in the pore fluid within sedimentary rocks from the Michigan Basin in southwest Ontario.

The following are the objectives for this research:

1- Development and application of a non-destructive X-ray spectrometric technique to measure diffusion and porosity in low permeability media (shale) using conservative (I^-) and non-conservative (Cs^+) tracers.

2- Use reactive-transport modeling to estimate diffusion coefficients for I^- and Cs+, and ion-exchange parameters for Cs+.

1.3. Thesis structure

This thesis is organized into three chapters in an article format. The first chapter consists of an introduction to the research including previous work, principles of the X-ray technique, and the research objectives.

Chapter 2 consists of an independent paper for submission to a scientific journal for publication. This section includes the description of samples used and the techniques employed in characterizing rock samples in terms of mineralogy and heterogeneity. Furthermore, Chapter 2 explains data acquisition for X-ray absorption spectrometry (XAS), tracer calibration, and data analysis to determine diffusion-accessible porosity, tracer concentration distributions, diffusion coefficients. Furthermore, multi-site ion exchange modeling was used to determine ion-exchange reaction parameters and diffusion coefficient for the reactive tracer.

Chapter 3 summarizes the scientific contributions and the conclusions of the thesis together with recommendations for future work.

Additional information can be found in the Appendices section.

1.4. References

Agbogun, H., Al, T. A., and Hussein, E. M., 2013a, Three dimensional imaging of porosity and tracer concentration distributions in a dolostone sample during diffusion experiments using X-ray micro-CT: Journal of contaminant hydrology, v. 145, p. 44-53.

Agbogun, H., Hussein, E. M., and Al, T. A., 2013b, Assessment of x-ray micro-CT measurements of porosity and solute concentration distributions during diffusion in porous geologic media: Journal of Porous Media, v. 16, no. 8.

Altman, S. J., Peplinski, W. J., and Rivers, M. L., 2005, Evaluation of synchrotron X-ray computerized microtomography for the visualization of transport processes in low-porosity materials: Journal of Contaminant Hydrology, v. 78, no. 3, p. 167-183.

Altman, S. J., Uchida, M., Tidwell, V. C., Boney, C. M., and Chambers, B. P., 2004, Use of X-ray absorption imaging to examine heterogeneous diffusion in fractured crystalline rocks: Journal of Contaminant Hydrology, v. 69, no. 1-2, p. 1-26.

Beyzadeoglu, M., Ozyigit, G., and Ebruli, C., 2010, Basic radiation oncology, Springer.

Boving, T. B., and Grathwohl, P., 2001, Tracer diffusion coefficients in sedimentary rocks: correlation to porosity and hydraulic conductivity: Journal of Contaminant Hydrology, v. 53, no. 1-2, p. 85-100.

Bradbury, M., and Green, A., 1985, Measurement of important parameters determining aqueous phase diffusion rates through crystalline rock matrices: Journal of Hydrology, v. 82, no. 1-2, p. 39-55.

Cave, L., Al, T., Xiang, Y., and Vilks, P., 2009, A technique for estimating one-dimensional diffusion coefficients in low-permeability sedimentary rock using X-ray radiography: comparison with through-diffusion measurements: J Contam Hydrol, v. 103, no. 1-2, p. 1-12.

Clausnitzer, V., and Hopmans, J. W., 2000, Pore-scale measurements of solute breakthrough using microfocus X-ray computed tomography: Water Resources Research, v. 36, no. 8, p. 2067-2079.

Cnudde, V., and Boone, M. N., 2013, High-resolution X-ray computed tomography in geosciences: A review of the current technology and applications: Earth-Science Reviews, v. 123, p. 1-17.

Cormenzana, J. L., García-Gutiérrez, M., Missana, T., and Junghanns, Á., 2003, Simultaneous estimation of effective and apparent diffusion coefficients in compacted bentonite: Journal of Contaminant Hydrology, v. 61, no. 1-4, p. 63-72.

Croisé, J., Schlickenrieder, L., Marschall, P., Boisson, J., Vogel, P., and Yamamoto, S., 2004, Hydrogeological investigations in a low permeability claystone formation: the Mont Terri Rock Laboratory: Physics and Chemistry of the Earth, Parts A/B/C, v. 29, no. 1, p. 3-15.

Feenstra, S., Cherry, J., Sudicky, E., and Haq, Z., 1984, Matrix diffusion effects on contaminant migration from an injection well in fractured sandstone: Groundwater, v. 22, no. 3, p. 307-316.

Fetter, C. W., Boving, T., and Kreamer, D., 2017, Contaminant hydrogeology, Waveland Press.

Flannery, B. P., Deckman, H. W., Roberge, W. G., and D'AMICO, K. L., 1987, Three-dimensional X-ray microtomography: Science, v. 237, no. 4821, p. 1439-1444.

Foster, S. S., 1975, The Chalk groundwater tritium anomaly—a possible explanation: Journal of Hydrology, v. 25, no. 1-2, p. 159-165.

Fuller, A. J., Shaw, S., Peacock, C. L., Trivedi, D., Small, J. S., Abrahamsen, L. G., and Burke, I. T., 2014, Ionic strength and pH dependent multi-site sorption of Cs onto a micaceous aquifer sediment: Applied geochemistry, v. 40, p. 32-42.

Fuller, A. J., Shaw, S., Ward, M. B., Haigh, S. J., Mosselmans, J. F. W., Peacock, C. L., Stackhouse, S., Dent, A. J., Trivedi, D., and Burke, I. T., 2015, Caesium incorporation and retention in illite interlayers: Applied Clay Science, v. 108, p. 128-134.

Garcıa-Gutiérrez, M., Missana, T., Mingarro, M., Samper, J., Dai, Z., and Molinero, J., 2001, Solute transport properties of compacted Ca-bentonite used in FEBEX project: Journal of Contaminant Hydrology, v. 47, no. 2-4, p. 127-137.

Gurumoorthy, C., and Singh, D. N., 2004, Diffusion of iodide, cesium and strontium in charnockite rock mass: Journal of Radioanalytical and Nuclear Chemistry, v. 262, no. 3, p. 639-644.

Hendry, M. J., Barbour, S. L., Boldt-Leppin, B. E., Reifferscheid, L. J., and Wassenaar, L. I., 2009, A comparision of laboratory and field based determinations of molecular diffusion coefficients in a low permeability geologic medium: Environmental science & technology, v. 43, no. 17, p. 6730-6736.

Hölttä, P., Hakanen, M., Hautojärvi, A., Timonen, J., and Väätäinen, K., 1996, The effects of matrix diffusion on radionuclide migration in rock column experiments: Journal of contaminant hydrology, v. 21, no. 1-4, p. 165-173.

Jakob, A., Pfingsten, W., and Van Loon, L., 2009, Effects of sorption competition on caesium diffusion through compacted argillaceous rock: Geochimica et Cosmochimica Acta, v. 73, no. 9, p. 2441-2456.

Johnson, R. L., Cherry, J. A., and Pankow, J. F., 1989, Diffusive contaminant transport in natural clay: a field example and implications for clay-lined waste disposal sites: Environmental Science & Technology, v. 23, no. 3, p. 340-349.

Ketcham, R. A., 2005, Three-dimensional grain fabric measurements using high-resolution X-ray computed tomography: Journal of Structural Geology, v. 27, no. 7, p. 1217-1228.

Ketcham, R. A., and Carlson, W. D., 2001, Acquisition, optimization and interpretation of X-ray computed tomographic imagery: applications to the geosciences: Computers & Geosciences, v. 27, no. 4, p. 381-400.

Loomer, D. B., Scott, L., Al, T. A., Mayer, K. U., and Bea, S., 2013, Diffusion–reaction studies in low permeability shale using X-ray radiography with cesium: Applied Geochemistry, v. 39, p. 49-58.

Maes, N., Salah, S., Jacques, D., Aertsens, M., Van Gompel, M., De Cannière, P., and Velitchkova, N., 2008, Retention of Cs in Boom Clay: comparison of data from batch sorption tests and diffusion experiments on intact clay cores: Physics and Chemistry of the Earth, Parts A/B/C, v. 33, p. S149-S155.

Mayer, K. U., 1999, A numerical model for multicomponent reactive transport in variably saturated porous media.

Melkior, T., Yahiaoui, S., Motellier, S., Thoby, D., and Tevissen, E., 2005, Cesium sorption and diffusion in Bure mudrock samples: Applied Clay Science, v. 29, no. 3-4, p. 172-186.

Nunn, J. A., Xiang, Y., and Al, T. A., 2018, Investigation of partial water saturation effects on diffusion in shale: Applied Geochemistry, v. 97, p. 93-101.

Oscarson, D., Dixon, D., and Gray, M., 1990, Swelling capacity and permeability of an unprocessed and a processed bentonitic clay: Engineering Geology, v. 28, no. 3-4, p. 281-289.

Oscarson, D., Hume, H., Sawatsky, N., and Cheung, S., 1992, Diffusion of iodide in compacted bentonite: Soil Science Society of America Journal, v. 56, no. 5, p. 1400-1406.

Oscarson, D. W., Hume, H. B., and King, F., 1994, Sorption of cesium on compacted bentonite: Clays and Clay minerals, v. 42, no. 6, p. 731-736.

Palut, J.-M., Montarnal, P., Gautschi, A., Tevissen, E., and Mouche, E., 2003, Characterisation of HTO diffusion properties by an in situ tracer experiment in Opalinus clay at Mont Terri: Journal of Contaminant Hydrology, v. 61, no. 1-4, p. 203-218.

Parkhurst, D. L., and Appelo, C., 2013, Description of input and examples for PHREEQC version 3: a computer program for speciation, batch-reaction, one-dimensional transport, and inverse geochemical calculations: US Geological Survey, 2328-7055.

Patera, E., Hobart, D., Meijer, A., and Rundberg, R., 1990, Chemical and physical processes of radionuclide migration at Yucca Mountain, Nevada: Journal of radioanalytical and nuclear chemistry, v. 142, no. 1, p. 331-347.

Sardini, P., Delay, F., Hellmuth, K.-H., Porel, G., and Oila, E., 2003, Interpretation of out-diffusion experiments on crystalline rocks using random walk modeling: Journal of Contaminant Hydrology, v. 61, no. 1-4, p. 339-350.

Savoye, S. b., Page, J., Puente, C. l., Imbert, C., and Coelho, D., 2010, New experimental approach for studying diffusion through an intact and unsaturated medium: a case study with Callovo-Oxfordian argillite: Environmental science & technology, v. 44, no. 10, p. 3698-3704.

Steefel, C., Appelo, C., Arora, B., Jacques, D., Kalbacher, T., Kolditz, O., Lagneau, V., Lichtner, P., Mayer, K. U., and Meeussen, J., 2015, Reactive transport codes for subsurface environmental simulation: Computational Geosciences, v. 19, no. 3, p. 445-478.

Steefel, C. I., Carroll, S., Zhao, P., and Roberts, S., 2003, Cesium migration in Hanford sediment: a multisite cation exchange model based on laboratory transport experiments: Journal of Contaminant Hydrology, v. 67, no. 1-4, p. 219-246.

Tachi, Y., Yotsuji, K., Seida, Y., and Yui, M., 2011, Diffusion and sorption of Cs+, I− and HTO in samples of the argillaceous Wakkanai Formation from the Horonobe URL, Japan: Clay-based modeling approach: Geochimica et Cosmochimica Acta, v. 75, no. 22, p. 6742-6759.

Tevissen, E., Soler, J., Montarnal, P., Gautschi, A., and Van Loon, L. R., 2004, Comparison between in situ and laboratory diffusion studies of HTO and halides in Opalinus Clay from the Mont Terri: Radiochimica Acta, v. 92, no. 9-11, p. 781-786.

Tidwell, V. C., Meigs, L. C., Christian-Frear, T., and Boney, C. M., 2000, Effects of spatially heterogeneous porosity on matrix diffusion as investigated by X-ray absorption imaging: Contaminant Hydrology, v. 42, p. 285-302.

Van Brakel, J., and Heertjes, P., 1974, Analysis of diffusion in macroporous media in terms of a porosity, a tortuosity and a constrictivity factor: International Journal of Heat and Mass Transfer, v. 17, no. 9, p. 1093-1103.

Van Loon, Soler, J., and Bradbury, M., 2003, Diffusion of HTO, 36Cl− and 125I− in Opalinus Clay samples from Mont Terri: Effect of confining pressure: Journal of Contaminant Hydrology, v. 61, no. 1-4, p. 73-83.

Van Loon, L. R., Baeyens, B., and Bradbury, M. H., 2009, The sorption behaviour of caesium on Opalinus Clay: A comparison between intact and crushed material: Applied Geochemistry, v. 24, no. 5, p. 999-1004.

Van Loon, L. R., Glaus, M. A., and Müller, W., 2007, Anion exclusion effects in compacted bentonites: Towards a better understanding of anion diffusion: Applied Geochemistry, v. 22, no. 11, p. 2536-2552.

Vilks, P., and Miller, N., 2007, Evaluation of experimental protocols for characterizing diffusion in sedimentary rocks: Atomic Energy of Canada Limited. Nuclear Waste Management Division Report TR-2007-11. Toronto, Ontario.

Waber, H., and Smellie, J., 2008, Characterisation of pore water in crystalline rocks: Applied Geochemistry, v. 23, no. 7, p. 1834-1861.

Wersin, P., Soler, J., Van Loon, L., Eikenberg, J., Baeyens, B., Grolimund, D., Gimmi, T., and Dewonck, S., 2008, Diffusion of HTO, Br−, I−, Cs+, 85Sr2+ and 60Co2+ in a clay formation: Results and modelling from an in situ experiment in Opalinus Clay: Applied Geochemistry, v. 23, no. 4, p. 678-691.

Wildenschild, D., Vaz, C., Rivers, M., Rikard, D., and Christensen, B., 2002, Using X-ray computed tomography in hydrology: systems, resolutions, and limitations: Journal of Hydrology, v. 267, no. 3-4, p. 285-297.

Xiang, Y., Al, T., and Mazurek, M., 2016, Effect of confining pressure on diffusion coefficients in clay-rich, low-permeability sedimentary rocks: J Contam Hydrol, v. 195, p. 1-10.

Xiang, Y., Al, T., Scott, L., and Loomer, D., 2013, Diffusive anisotropy in low-permeability Ordovician sedimentary rocks from the Michigan Basin in southwest Ontario: Journal of contaminant hydrology, v. 155, p. 31-45.

Young, D. F., and Ball, W. P., 1998, Estimating diffusion coefficients in low-permeability porous media using a macropore column: Environmental science & technology, v. 32, no. 17, p. 2578-2584.

Zachara, J. M., Smith, S. C., Liu, C., McKinley, J. P., Serne, R. J., and Gassman, P. L., 2002, Sorption of Cs+ to micaceous subsurface sediments from the Hanford site, USA: Geochimica et cosmochimica Acta, v. 66, no. 2, p. 193-211.

Chapter 2 - Measurement of Diffusion Coefficients for Iodide and Cesium in Shale by X-ray Absorption Spectrometry (XAS)

2.0. Abstract

A new, non-destructive method has been developed for measurement of diffusion coefficients for conservative (iodide, I^-) or reactive (cesium, Cs^+) tracers in porous media; in this case samples of the Queenston Formation shale from the Michigan Basin in southwest Ontario, Canada. The method employs X-ray absorption spectrometry (XAS) with a lab-based configuration. A 1-mm diameter collimated X-ray beam is used in transmission mode to collect spatially-resolved one-dimensional profiles of the tracer distribution parallel to the diffusion transport direction. The method avoids the artifacts and errors from beam hardening that are common to radiographic imaging approaches. Additional analyses such as mineralogical studies by scanning electron microscopy with energy dispersive X-ray spectroscopy (SEM-EDS) were conducted to improve the understanding of solute transport. The resultant data obtained by XAS indicates good agreement with an established radiography method. The mean values for the pore diffusion coefficient (D_P) for Cs^+ and I^- and the iodide-accessible porosity (ϕ_I) were estimated at $4.24 \times 10^{-11}\ m^2 \cdot s^-$, $3.35 \times 10^{-11} m^2 \cdot s^-$ and 0.060 respectively. It is concluded that the XAS method is well-suited for non-destructive characterization of diffusive transport in porous media.

Key words: diffusion, shale, X-ray absorption spectrometry, cesium, iodide

2.1. Introduction

Radioactive waste generated by nuclear energy requires safe, long-term containment, and natural geologic environments are being considered for deep geological repositories (DGR) by several countries. Low permeability formations such as the Callovo-Oxfordian claystone in France (Descostes et al., 2008; Savoye et al., 2012; Savoye et al., 2010), the Wakkanai Formation in Japan (Tachi et al., 2011), the Opalinus clay in Switzerland (Appelo and Wersin, 2007; Jakob et al., 2009; Lauber et al., 2000; Tevissen et al., 2004; Wersin et al., 2004), the Boom clay in Belgium (De Cannière et al., 1996), and the Cobourg Formation in the Michigan Basin in southern Ontario (Al et al., 2015; Cavé et al., 2009a; Cavé et al., 2009b; Loomer et al., 2013; Xiang et al., 2016) are under consideration.

Both field and laboratory experiments have been conducted to provide information on the diffusion of reactive cesium (Cs^+) and conservative iodide (I^-) species in low-permeability media (Van Loon et al., 2009; Van Loon et al., 2004; Wersin et al., 2008; Wersin et al., 2004) and the results demonstrated that there is good agreement between in-situ diffusion data and data acquired from laboratory experiments. Consequently, it is common practice to investigate diffusion process in the laboratory with cm-scale samples.

The diffusion of Cs^+ and I^- species has been experimentally investigated in low-permeability media via through-diffusion (Garcıa-Gutiérrez et al., 2001; Van Loon et al., 2007; Van Loon et al., 2003; Vilks et al., 2007) and in-diffusion (Cormenzana et al., 2003; Garcıa-Gutiérrez et al., 2001) techniques. The time required to reach steady-state conditions in through-diffusion experiments could take months to years, especially for reactive diffusive species. In contrast, the in-diffusion method provides the advantage of a shorter time duration because steady state is not required. Out-diffusion, is another experimental approach, and it can be carried out in tandem with the through-diffusion process (Kasar et al., 2016; Sardini et al., 2003). In most cases, out-, in- and

through-diffusion experiments provide bulk diffusion coefficients (e.g. D_e and D_a) for rock samples, meaning the measurements do not account for spatial heterogeneity in the material.

In experiments dealing with reactive tracer species such as the tracer may be retarded by adsorption to minerals surfaces, a process that is primarily Cs^+, controlled by the negatively charged mineral surfaces and associated cation exchange sites (Bradbury and Baeyens, 2000; Savoye et al., 2012;Tachi et al., 2009). Specifically, with respect to Cs^+ adsorption in clay-rich rocks, Bradbury and Baeyens, (2000) and Tamura and Jacobs (1960) describe adsorption to ion-exchange sites at planar surfaces, edges and interlayer structural sites on clay minerals. The experiments, commonly use a distribution coefficient (K_d) to account for solute partitioning to the solid phase and K_d values are generally obtained from batch experiments (Bradbury and Baeyens, 2000; Kasar et al., 2016; Van Loon et al., 2003).

Previous, researchers have evaluated K_d and cation exchange capacity (CEC) values for both crushed and intact rock samples (Appelo et al., 2010; Jakob et al., 2009; Melkior et al., 2005; Soler et al., 2013; Van Loon et al., 2009). They reported a good agreement between K_d and CEC values from Cs^+sorption experiments with crushed and intact samples. A sorption isotherm, i.e. the sorption of Cs^+, as function of the radionuclide equilibrium concentration at constant pH in synthetic pore water (SPW) was measured, irrespective of whether the Cs^+ inventory (concentration) was taken into account or was ignored. In addition, quantification of the transport and reaction processes has been done using reactive transport codes (Loomer et al., 2013; Siroux et al., 2018; Soler et al., 2013; Steefel et al., 2003). In the diffusion–reaction models clay minerals such as shale are defined as exchangers with one or different multi-ion exchange site(s). Cs^+-Na^+exchange reaction is included for the major ions in both SPW and tracer solutions. The model geometry is based on the regular domain for the spatial discretization. In the model no advective transport (i.e., diffusion only) is considered and constant-concentration and zero-mass-flux

boundary conditions are taken into account at the influx boundary and at the end of the domain respectively.

Most experimental techniques for diffusion measurement, some of which are destructive and require cutting the sample into sections and extracting the solute for quantitative analysis, do not provide information about spatial heterogeneity in the physical properties of the porous media or the temporal variations in tracer distributions. These gaps in knowledge can be overcome with the use of non-destructive X-ray imaging/analysis techniques, making it possible to characterize textural features of an object (Cnudde and Boone, 2013; Ketcham, 2005; Ketcham and Carlson, 2001; Wildenschild et al., 2002) and monitor tracer movement in porous media (Agbogun et al., 2013; Altman et al., 2005; Cave et al., 2009a; Clausnitzer and Hopmans, 2000; Frohlich et al., 2012; Loomer et al., 2013; Tidwell and Glass, 1994; Tidwell et al., 2000 Xiang et al., 2013b). Most of these techniques are based on sequential radiographic imaging of the mass distribution of a migrating tracer that is dissolved in the pore fluid of a rock sample. A calibration is used to transform mass to concentration, and the concentration data are fit to a mathematical model for diffusion in order to quantify D_p values. These X-ray-imaging techniques use X-ray attenuating tracers to track solute transport. According to the Beer-Lambert law,

$$I_{(E)} = I_{0\,(E)} \exp(-\mu_{(E)} d) \qquad (2.1)$$

If monochromatic radiation with an initial intensity (I_0) travels through a homogenous sample of thickness d, the measured X-ray beam intensity (I) is attenuated as a function of the linear attenuation coefficient (μ) of the sample and the photon energy (E). For a polychromatic X-ray source, as is common for lab-based X-ray systems, preferential absorption of the lower-energy portion of the beam causes an artifact referred to as beam hardening. This artifact is not constant and changes as a function of beam energy and sample characteristics (effective atomic number),

thereby imposing measurement errors that are difficult to prevent or correct (Ketcham and Carlson, 2001; Wildenschild et al., 2002).

X-ray spectrometry (Jacobsen et al., 2000; McMaster et al., 1970; Thrippleton et al., 2003; Yankovich and Swainson, 2000) offers an alternative to radiographic imaging that can minimize the influence of beam hardening. Herein, we report on a novel spectrometric technique that has been developed to allow estimation of solute-specific diffusion coefficients based on X-ray absorption spectra created by the interaction of X-rays with Cs^+ and I^- tracers during diffusion experiments with low-permeability shale.

2.1.1. X-ray Absorption Approach

The X-ray absorption spectrometry (XAS) technique utilizes tracer-specific energy ranges, or regions of interest (ROI; Fig. 2.1), in the spectrum in order to detect and quantify the concentration of soluble tracers in the porewater contained in porous geologic media. By choosing a specific energy range, the beam hardening effect becomes inconsequential, offering an advantage over radiation-imaging techniques.

The technique employs a collimated X-ray beam (~ 1.1 mm diameter) that is incident on a sample of porous rock while the transmitted beam is detected on the opposite side of the sample, allowing acquisition of a transmitted X-ray energy spectrum. Transmitted spectra are recorded before (reference spectrum) and after (tracer-diffusion spectrum) introducing an aqueous tracer to the porewater via diffusion. In the example shown in Figure 2.1, a reference spectrum is presented along with a spectrum acquired after introduction of a Cs^+ tracer to the sample. The presence of Cs^+ in the porewater is indicated by the decrease, or attenuation of the X-ray intensity in ROI-2, immediately above the K-edge for X–ray absorption by Cs^+. Quantification of the Cs^+ concentration in the porewater is possible because the magnitude of the attenuation in ROI-2 is proportional to the concentration.

X-ray attenuation can be represented mathematically by the Beer - Lambert Law (Ketcham, 2005) such that the difference in X-ray attenuation in ROI-2 between the reference and the tracer-diffusion spectra is referred to here as $\Delta\mu$ which is a function of the tracer mass contained in the pore spaces along the X-ray path.

$$\Delta\mu = ln(I)_{ref} - ln(I)_t \tag{2.2}$$

where:

$(I)_{ref}$ is the integrated X-ray intensity in ROI-2 for the reference spectrum, and

$(I)_t$ is the integrated X-ray intensity in ROI-2 for the tracer diffusion spectrum.

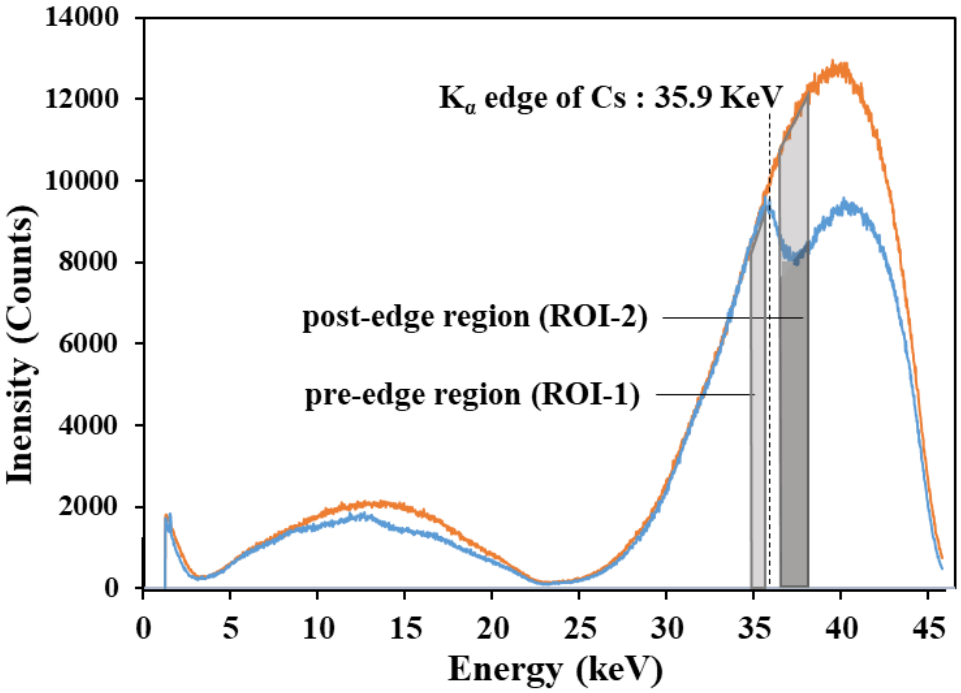

Figure 2.1. Examples of XAS spectra showing a reference spectrum (orange) and a tracer-diffusion spectrum for Cs^+ (blue). The X-ray absorption edge for Cs^+ is indicated by the vertical dashed line and the pre-edge and post-edge energy ranges of interest are designated ROI-1 and ROI-2 respectively. The

presence of Cs^+ in the sample porewater is reflected by the sharp decrease in counts in the post-edge region ROI-2.

2.2. Materials and Methods

2.2.1. Rock Samples and Thin Section Preparation

Rock samples used in this study (Fig 2.2) were obtained from the Ordovician Queenston Formation shale in drill core DGR3 that was drilled by Ontario Power Generation and the Nuclear Waste Management Organization at the Bruce nuclear site in southwest Ontario (Fig. 2.3). At the Bruce nuclear site, the Queenston Formation is approximately 75 m thick (depth of 456 m to 530 m in drill core DGR3), and the samples were collected at a depth of 525.86 m. The clay minerals of the Queenston Formation are mainly illite (58.2-60.9%) and carbonates (calcite (6.1-14.6%)and dolomite, 6.6-11.4%) and quartz (23.5-34.1%). Chlorite (29.1-39.1%) is the other major components in these shales (Jackson, 2009). The stratigraphy and depositional history of the Queenston Formation is summarized by (Armstrong and Carter, 2010; Armstrong and Carter, 2010; Brogly et al., 1998).

Six samples were sub-cored, using a 11 mm diameter diamond drill bit, from a 75.80 mm diameter slice of core; five subcores were extracted from the same slice and one from an adjacent slice. The six sub-cored samples are 20 mm in length and were drilled normal to bedding using compressed air for cooling the drill bit and clearing the cuttings. Three of the five samples from the same slice were used for diffusion experiments with an I^- tracer (Table 2.1). The remaining three were used for diffusion-reaction experiments with a Cs^+ tracer (Table 2.1).

Following the diffusion experiments, the sub cores were cut along the cylindrical axis and polished thin sections were prepared to facilitate mineralogical analysis. The thin sections were polished in kerosene to prevent dissolution of soluble minerals.

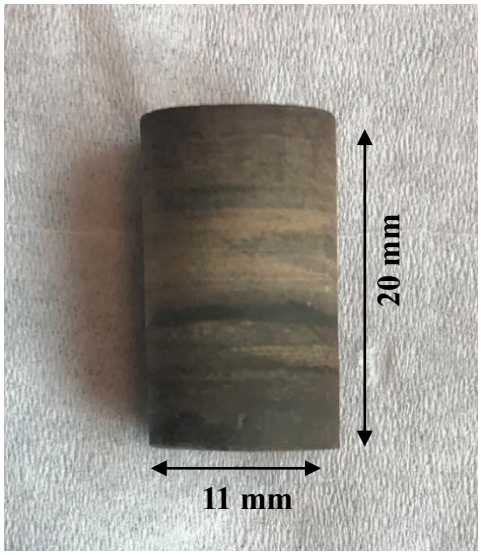

Figure 2.2. Image of one subcored sample from drill core DGR3

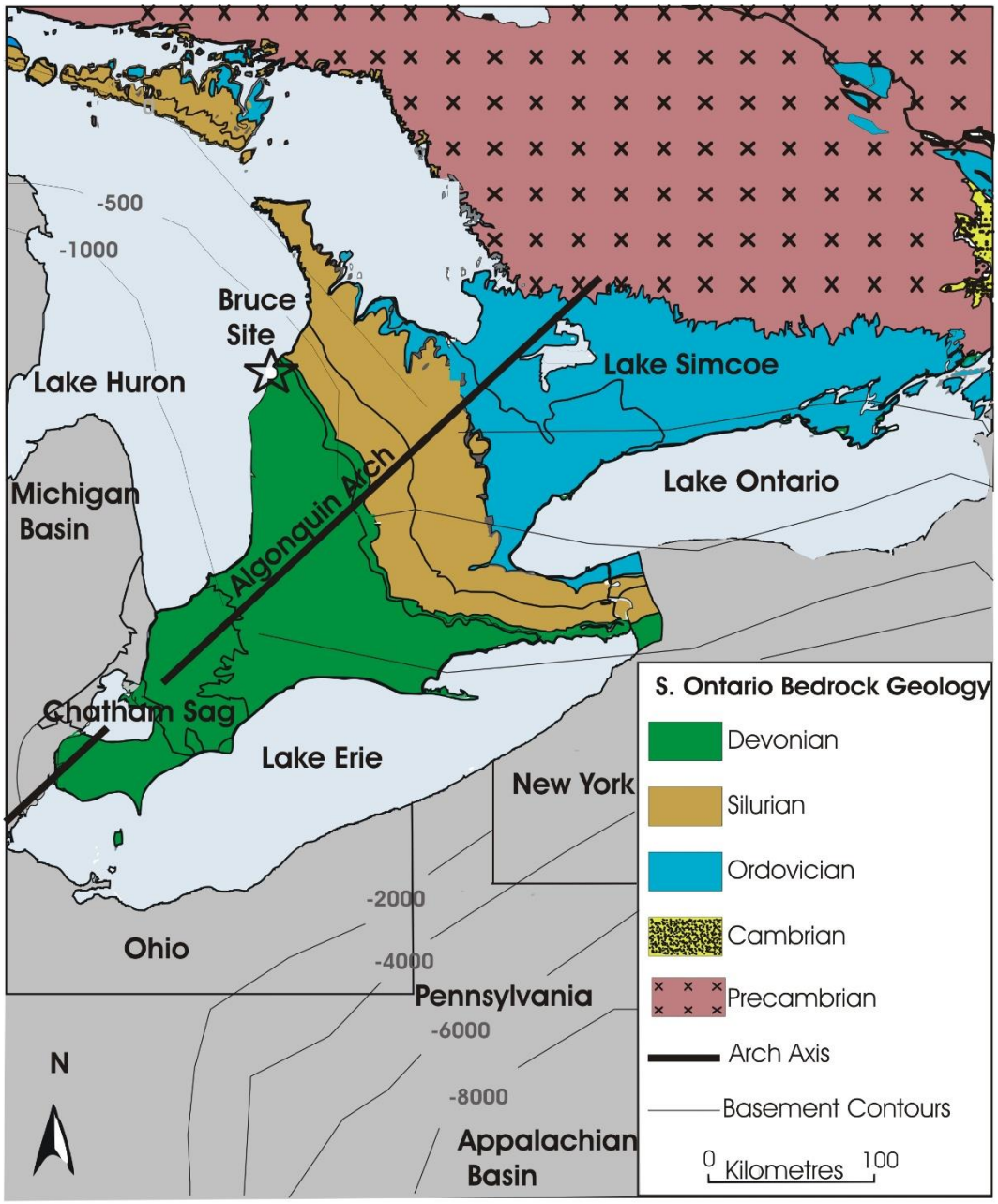

Figure 2.3. The Paleozoic bedrock map of southern Ontario illustrating the location of the Bruce nuclear site (Al et al., 2015)

Table 2.1. Descriptions of samples used in the diffusion experiments

Sample	Slice	Lithology	Depth (m)	Tracer
DGR3a	Slice 1	Red/green shale	525.86	I^-
DGR3b	Slice 1	Red/green shale	525.86	I^-
DGR3e	Slice 1	Red/green shale	525.86	I^-
DGR3g	Slice 1	Red/green shale	525.86	Cs^+
DGR3j	Slice 1	Red/green shale	525.86	Cs^+
DGR3c	Slice 2	Red/green shale	525.84	Cs^+

2.2.2. Mineralogical and Textural Analysis

Mineralogical and textural investigations were conducted by scanning electron microscopy (SEM) in the Earth Sciences Microanalytical Laboratory at the University of Ottawa using polished thin sections (100 μm thick). The investigations were conducted with a JEOL JSM-6610LV instrument, equipped with an Oxford INCA energy-dispersive X-ray spectroscopy (EDS) system. Observations of texture primarily focused on the nature and distribution of porosity.

2.2.3. Porewater and Tracer Solution Compositions

The shale synthetic pore water (SPW) composition described by (Al et al., 2010) was used to initialize the porewater composition for all experiments. The Cs^+ and I^- tracer solutions were both prepared in a SPW matrix using molar substitution of sodium chloride (NaCl) for sodium iodide (NaI) or cesium chloride (CsCl) (Table 2.2). It is known that I^- in solution is mildly reducing, thus

reacts with oxygen to produce iodine (I_2) (Dobson and Grossweiner, 1964). Moreover, photochemical experiments have shown evidence that aqueous I^- exposed to visible-light radiation undergoes photo-oxidation (Ayscough et al., 1967; Dobson and Grossweiner 1964; Truesdale, 2007). To counteract the oxidation of I^-, 0.85 mL (0.025 mol/L) sodium thiosulfate ($Na_2S_2O_3$), a strong reducing agent, was added to 1L of tracer to maintain iodine in the reduced form (Cadle and Huff, 1950):

$$2Na_2S_2O_3 + I_2 \rightarrow 2NaI + Na_2S_4O_6 \quad (2.3)$$

Table 2.2. Ion concentrations in SPW and tracer solutions

Components	**SPW (mol/l)**	**I^- tracer (mol/l)**	**Cs^+ tracer (mol/l)**
Na^+	2.4	2.4	1.4
K^+	0.5	0.5	0.5
Mg^{2+}	0.25	0.25	0.25
Ca^{2+}	1.2	1.2	1.2
Cl^-	5.8	4.8	5.8
SO_4^{2-}	0.001	0.001	0.001
I^-	-	1	-
Cs^+	-	-	1.0

2.2.4. Sample Saturation

The natural pore water in the Queenston Formation shale is near saturation with respect to halite mineral (Al et al., 2015; Al et al., 2010), but following drilling, some evaporation may occur, leading to partial desaturation and possible precipitation of halite which could obstruct pore spaces. Prior to conducting diffusion experiments, samples were resaturated with SPW by placing them in a desiccator with a beaker of deionized water (DI) to create a vapor pressure gradient between pore spaces in the sample and the air in the desiccator. The difference in vapor pressure causes water vapor to diffuse into the air-filled portion of the pores and replenish the lost porewater. Once water

droplets were visible on the sample surface, they were submerged in SPW solution to complete the re-saturation. The shale synthetic pore water (SPW) solution was refreshed weekly for three weeks. Once saturated, samples were kept in a closed container with an open vial of SPW to maintain constant humidity in equilibrium with the samples, thereby minimizing evaporation.

2.2.5. Water-Accessible Porosity and Grain Density

The off-cuttings from sub-coring were used to measure water-accessible porosity (ϕ_w) (Figs. 2.4 and 2. 5). Samples were dried in an oven at 105°C and weighed every 24 hours until there was no measurable change in mass at which point the dry mass (M_d) was recorded. The samples were cooled in a desiccator before each mass measurement. Samples were then saturated with SPW according to the method described in section 2.2.4 and the submerged mass was measured (M_{sub}) in a beaker of SPW (Fig. 2.4b). Finally, samples were removed from the SPW, patted dry with a tissue, and a drying curve was recorded (Fig. 2.5). The drying curves (mass vs time) generally display two linear slopes (drying rates) due to; (1) evaporation from the surface and (2) evaporation from the pores. The critical point, or intersection, between these lines is calculated and represents the saturated mass (M_{sat}). These measurements were also used to calculate grain density (ρ_{gr}). The equations for porosity and grain density calculation are described below (Al et al., 2010) :

$$V_{rock} = \frac{M_{sat} - M_{sub}}{\rho_{brine}} \tag{2.4}$$

$$V_{voids} = \frac{M_{sat} - M_d}{(1 - X)\,\rho_{brine}} \tag{2.5}$$

$$\emptyset_w = \frac{V_{voids}}{V_{rock}} * 100 \tag{2.6}$$

$$\rho_{gr} = \frac{M_{rock}}{V_{rock} - V_{voids}} \quad (2.7)$$

where:

V_{rock}= volume of the sample

V_{voids}= volume of the pore spaces

X = mass fraction obtained from SPW solution

ρ_{brine} = density of brine solution.

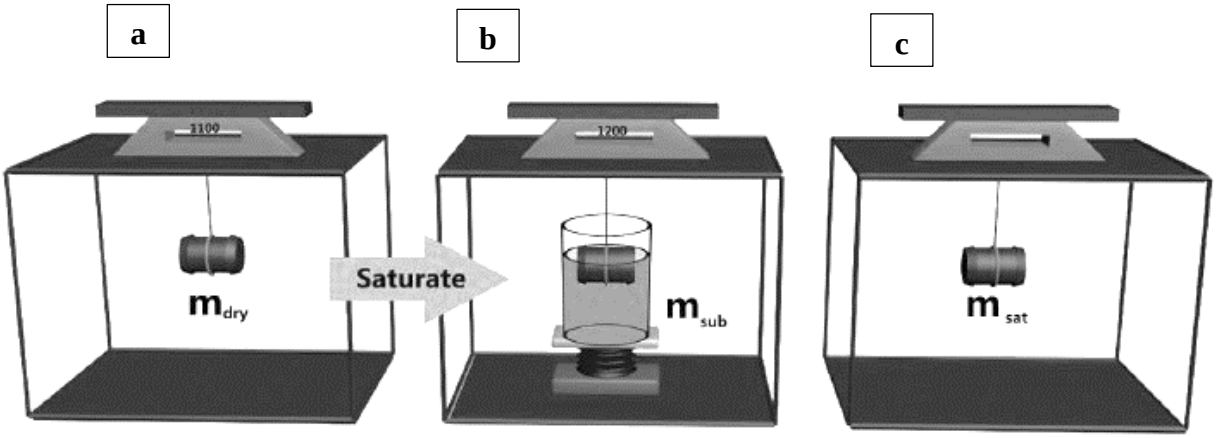

Figure 2.4. Schematic diagram indicating the ϕ_w measurement steps for a) M_d b) M_{sub} and c) Msat.

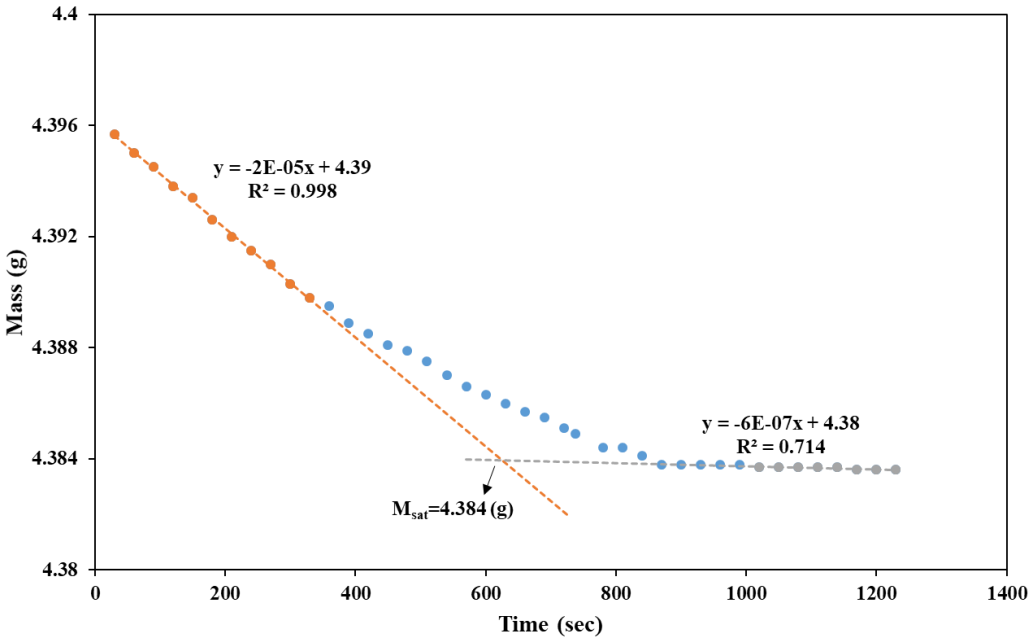

Figure 2.5. Example of a drying curve from slice 2 showing two linear regions (orange and grey symbols) representing drying, or evaporation rates from the surface and from the pores. The intersection of the two lines represents M_{sat}.

2.2.6. Diffusion Cells

The circumference of the SPW-saturated samples was coated with a thin layer of silicone (GE Silicone 1) to prevent solute migration along the side of the sample and then mounted on an acrylic diffusion cell with a solution reservoir (Fig. 2.6). The sample rests on a pedestal, with the bottom surface in contact with a felt pad that is in contact with the solution reservoir. Another felt pad and an aluminum cap, which serves as an internal standard, is placed on the top surface. The aluminum cap contains a threaded hole, sealed with a nylon screw and O-ring, to allow exchange of SPW and tracer fluids at the top boundary of the sample. The felt pads maintain capillary saturation and prevent air bubble formation at the top and bottom boundaries. The pedestal, sample and cap are enclosed and held in place by a layer of heat-shrink tubing around the circumference. The reservoir is equipped with tubes and valves allowing exchange of SPW and tracer solutions in the reservoir.

Prior to addition of SPW to the reservoir, the reservoir is flushed with CO_2, to replace air with the more soluble gas using the method described by Xiang et al. (2016). This aids in preventing air bubble formation in the reservoir which can limit or prevent diffusion at the influx boundary.

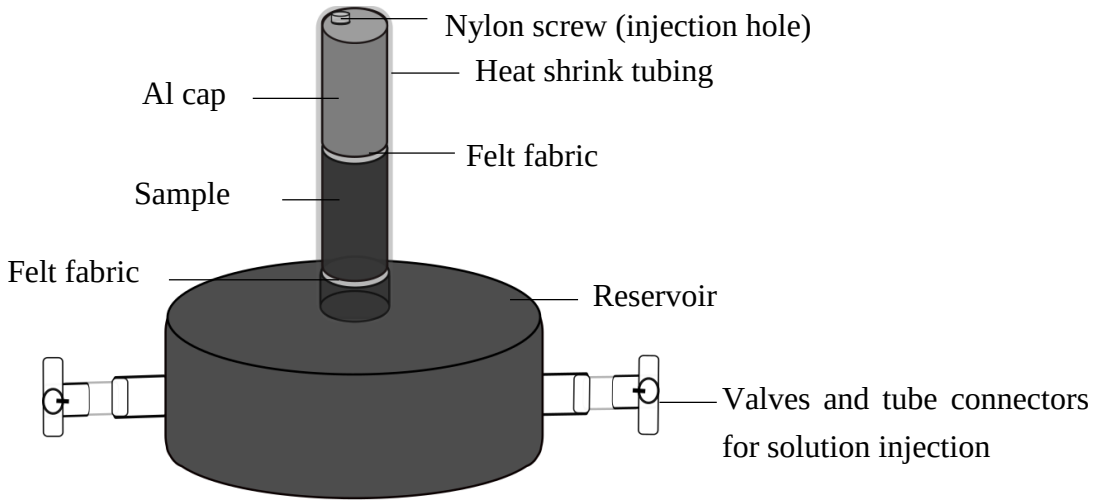

Figure 2.6. Schematic diagram of the diffusion cell used for XAS.

2.2.7. Diffusion Experiments

The X-ray absorption spectrometry (XAS) measurements were conducted using a custom-built X-ray instrument from Pinnacle X-ray Systems (Atlanta, Georgia) equipped with a 3 kW X-ray source (Varian NDI-160-22). Spectrometry measurements were conducted with an Amptek CdTe XR100CR detector and PX5 Digital Pulse Processor – Multi-channel Analyzer (DPP-MCA). The detector energy scale was calibrated on the Pb Lβ (12.61 keV) and Sn Kα (25.27 keV) lines from a PbSn alloy (Appendix C). The samples were mounted on a Velmex rotational stage (B5990TS) and a Velmex BiSlide (PK245-01AA) which, respectively, allow rotation, as well as vertical and horizontal motion (Fig. 2.7) in a plane orthogonal to the X-ray beam. The X-ray beam was collimated (Fig. 2.7; Appendix B) in order to control the spatial resolution for the XAS measurements. The field of view (FOV) for the collimated beam was imaged and measured in

digital radiographs, and the diameter, 1.1 mm, is equivalent to the spatial resolution for the measurements.

Measurements were conducted by positioning the sample on the stage between the X-ray source and the detector, with the beam aligned at the bottom of the sample. The data acquisition parameters are indicated in Table 2.3. During data collection for a single step, the sample was rotated continuously for 6 min at 2 rpm such that each step represents the X-ray absorption properties for a disc-shaped volume with a height of 1.1 mm (spatial resolution). After completion of each step, the stage was moved down 1.1 mm and the acquisition process was repeated for the number of steps required to collected data across the full height of the sample (Table 2.3); a dataset referred to hereafter as a profile.

Preparation for an experiment requires acquisition of triplicate profiles in the absence of tracer; the average of these is hereafter referred to as the reference profile. The experiment is then initiated by replacing the SPW solution in the reservoir of the diffusion cell with tracer solution (Table 2.2), flushing three times with tracer solution to prevent dilution of the tracer. This introduction of tracer represents the start time for the experiment (t_0). Tracer diffusion was monitored by the collection of XAS profiles at 24 hour intervals for the first five days, after which the interval was increased to a maximum of 48 hours. The experiments were terminated after seven to ten days when measurements indicated that tracer breakthrough occurred at the top boundary. Mass-balance calculations between the sample pore volume and the reservoir volume indicate that the maximum decrease in tracer concentration in the reservoir by diffusion into the sample is only 1.8%. Therefore, the concentration at the influx boundary is considered constant for the duration of the experiments.

Two types of measurement error, repositioning and instrumental error, were determined while there was no tracer in the samples. To calculate repositioning error, the samples were repositioned

for each measurement (e.g., the sample was taken out and replaced in the same position again), and for determination of instrumental error the sample position was held constant while three sequential measurements were acquired. The relative standard deviation (RSD%) for repositioning and instrumental error are 0.032%. and 0.029% respectively.

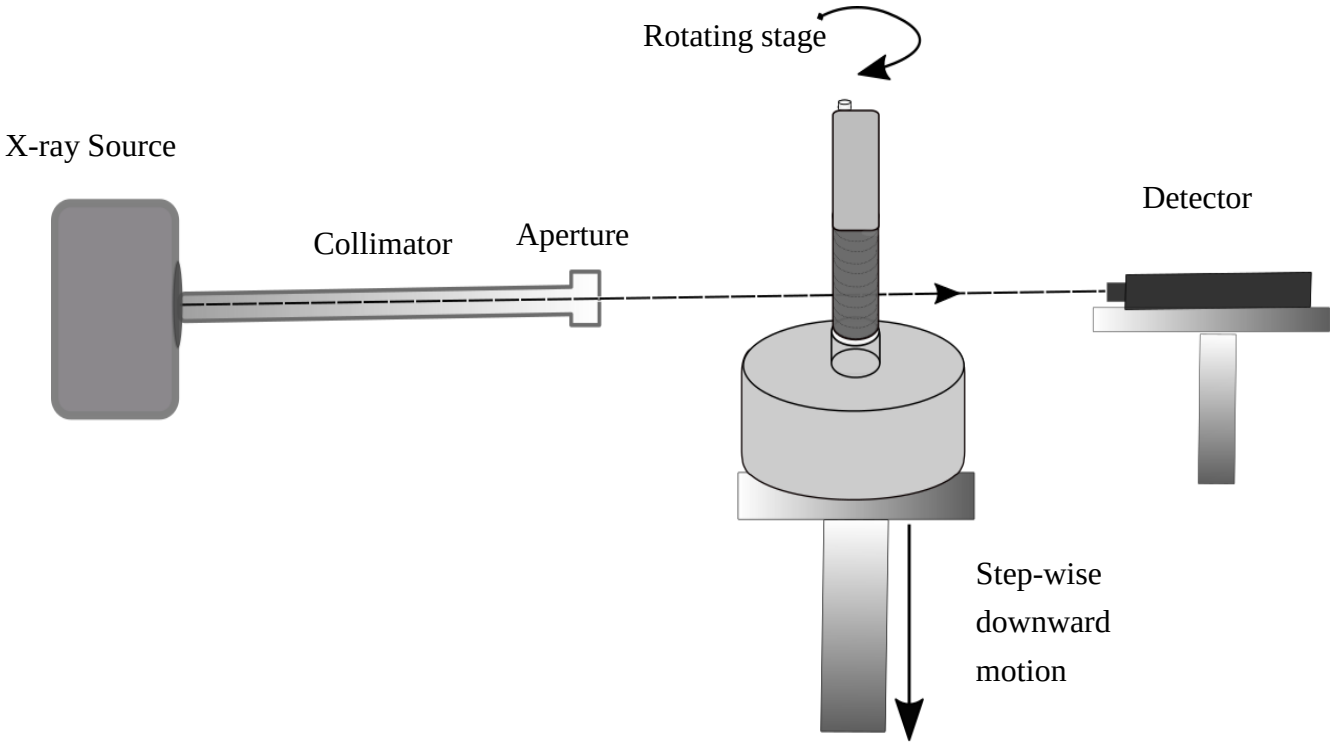

Figure 2.7. The geometry of XAS experiment set up

Table 2.3. X-ray spectrometry data acquisition parameters

Parameter	**Diffusion /Calibration**		**Beam hardening**	
	Cs^+	**I^-**	**Cs^+**	**I^-**
Source potential (kV)	45	40	45	45
Source current (mA)	1.0	1.5	0.5	0.5
Aluminum filter (mm)	4.1	-	5.8	5.8
Collimator aperture (mm)	1	1	1	1
Rotation rate (deg/min)	720	720	720	720
Time per step (min)	6	6	6	6
Vertical motion increment (mm)	1.1	1.1	1.1	1.1

2.2.8. Beam Hardening

The relationship between the $\Delta\mu$ and I^- or Cs^+concentration was measured in several different sample containers to evaluate the susceptibility of the spectrometry approach to X-ray beam hardening artifacts. Following the approach described by Loomer et al. (2013), $\Delta\mu$ was determined for plastic (Cole-Parmer) and ceramic (Macor; McMaster-Carr) vials containing variable concentrations of I^- or Cs^+ tracer solutions. The internal diameters of the ceramic vials range from 1.5 to 4.5 mm and the outer diameters are constant (11 mm). These dimensions were used to define the ratio of void volume to total volume along the beam path – here referred to as porosity (Table 2.4). The porosity values were used to calculate effective tracer concentration values as the product of the solution tracer concentration and the porosity. The measurements were conducted using the instrumental conditions noted in Table 2.3.

2.2.9. Calibration

Measurements were conducted to define calibration curves relating $\Delta\mu$ to tracer concentration in order to transform $\Delta\mu$ values from I^- and Cs^+ diffusion experiments to relative concentrations. The measurements were conducted using Macor ceramic vials (McMaster-Carr) with SPW and a 1 M tracer solution to determine $\Delta\mu$. The porosity values for the ceramic vials were used to calculate effective tracer concentrations as the product of the concentration of the tracer solutions and the porosity. The measurements were conducted using the instrumental conditions noted in Table 2.3.

Table 2.4. Material dimensions and porosity values used in the beam-hardening and calibration experiments

Materials	Inner diameter (mm)	Outer diameter (mm)	Porosity
Plastic vial	11.24	13.1	1.02
Ceramic A	2.5	11	0.223
Ceramic B	4.5	11	0.410
Ceramic C	1.5	11	0.127
Ceramic D	3.5	11	0.316

2.2.10. Data Processing

2.2.10.1. Normalization

The spectra resulting from the multiple steps in each profile were processed as described in section 2.1.1 to derive Δμ profiles (Eq. 2.2) for each time step. The energy ranges for ROI-1 and ROI-2 (Fig. 2.1) are specific for each tracer and they are presented in Table 2.5 Prior to calculation of Δμ, the spectra must be corrected to account for variations in signal intensity resulting from possible fluctuations in the power source to the X-ray tube. This correction is accomplished by normalizing all spectra to a fixed normalization value (NV) for the integrated counts in ROI-1 (Table 2.6).

$$NI_{ROI-2} = \left(\frac{NV}{I_{ROI-1}}\right) * I_{ROI-2} \tag{2.8}$$

where:

NI_{ROI-2} = normalized intensity for ROI-2

I_{ROI-1} and I_{ROI-2} = measured intensities in ROI-1and ROI-2 respectively.

Table 2.5. Energy ranges (keV) for pre- and post-edge regions of interest

	Cs^+	I^-
ROI-1	34.8 - 35.8	32.0 - 32.8
ROI-2	36.5 - 38.5	33.5 - 36.2

Table 2.6. Normalization values (counts)

Cs^+	I^-
400000	400000

2.2.10.2. Propagation of Uncertainties

The uncertainties reported in $\Delta\mu_{x\_t}$ have been calculated (Taylor, 1997) from the propagation of uncertainty obtained from triplicate measurements of the reference profiles (no tracer):

$$\Delta\mu_{x\_t} \pm \boldsymbol{w_x} = ln(\mathrm{I})_{x\_ref} \pm \boldsymbol{a_x} - ln(\mathrm{I})_{x\_t} \pm \boldsymbol{a_x} \quad (2.9)$$

where:

$\boldsymbol{a_x}$ is the standard deviation for $ln(\mathrm{I})_{x\_ref}$ at each point in *x* along the reference profile

$\boldsymbol{w_x}$ is the uncertainty for $\Delta\mu_{x\_t}$ at each point in *x* calculated by quadratic sum:

$$\boldsymbol{w_x} = \sqrt{(\boldsymbol{a_x})^2 + (\boldsymbol{a_x})^2} \quad (2.10)$$

Similarly, triplicate measurements of the tracer-saturated profiles were used to calculate the uncertainty for $\Delta\mu_{x\_sat}$:

$$\Delta\mu_{x\_sat} \pm \boldsymbol{y_x} = ln(\mathrm{I})_{x\_ref} \pm \boldsymbol{a_x} - ln(\mathrm{I})_{x\_sat} \pm \boldsymbol{z_x} \quad (2.11)$$

where:

$\boldsymbol{z_x}$ is the standard deviation for $ln(\mathrm{I})_{x\_sat}$ at each point in *x* along the tracer saturated profiles

$\boldsymbol{y_x}$is the uncertainty in $\Delta\mu_{x\_sat}$ at each point in *x* calculated by quadratic sum:

$$\boldsymbol{y_x} = \sqrt{(\boldsymbol{a_x})^2 + (\boldsymbol{z_x})^2} \tag{2.12}$$

Using the uncertainties for $\Delta\mu_{x\_t}$ and $\Delta\mu_{\mathrm{x\_sat}}$, the uncertainty for $\frac{C}{C_0}$ from equation (Eq.2.16) is:

$$\boldsymbol{n} = \sqrt{\left(\frac{\boldsymbol{w}}{\Delta\boldsymbol{\mu}_{\boldsymbol{x\_t}}}\right)^{\mathbf{2}} + \left(\frac{\boldsymbol{y}}{\Delta\boldsymbol{\mu}_{\mathbf{x\_sat}}}\right)^{\mathbf{2}}} \times \left|\frac{\boldsymbol{C}}{\boldsymbol{C_0}}\right| \tag{2.13}$$

2.2.10.3. Iodide-Accessible Porosity Measurements

In order to calculate the iodide-accessible porosity (ϕ_{I}), and to transform the Δμ profiles to relative concentration $\left(\frac{C}{C_0}\right)$,the concentration of I^- in the pore fluid must be uniform through the sample, and equal to the initial concentration at the influx boundary (Cavé et al., 2009a; Cavé et al., 2010; Loomer et al., 2013). This was achieved following the collection of I^- diffusion profiles by adding tracer solution to the top boundary via the threaded hole in the Al cap, allowing tracer ingress via diffusion from both ends. Calculations using the reactive transport code, PHREEQC (Parkhurst and Appelo, 1999), indicated 45 days are required to attain complete tracer saturation (Appendix A). Iodide tracer was allowed to diffuse into the samples for a period of 45 days and, to avoid oxidation of I^-, the samples were stored in the dark in a chamber containing N_2 gas. After 45 days, three additional Δμ profiles were acquired for each sample over a period of 3 days. As no measureable differences were observed among the triplicate datasets, the samples were considered to have achieved complete tracer saturation. At this stage, a Δμ profile, representing the spatially-resolved X-ray attenuation values for a tracer-saturated sample, $\Delta\mu_{x\_sat}$, was calculated:

$$\Delta\mu_{x\_sat} = ln(\mathrm{I})_{x\_ref} - ln(\mathrm{I})_{x\_sat} \quad (2.14)$$

where:

$\Delta\mu_{x\_sat}$ = change in X-ray attenuation due to the presence of tracer at distance, *x*

$ln(\mathrm{I})_{x\_ref}$ = X-ray intensity in the reference profile at distance, *x*

$ln(\mathrm{I})_{x\_sat}$ = X-ray intensity in the tracer-saturated profile at distance, *x*.

Using values for $\Delta\mu_{\mathrm{x\_sat}}$ the spatially resolved values for ϕ_{I} can be determined using the calibration function.

$$\phi_{x\_I} = \frac{\Delta\mu_{\mathrm{x\_sat}}}{m\ C_0} \quad (2.15)$$

where:

m = the slope of the linear calibration function.

2.2.10.4. Iodide Tracer Concentrations and Diffusion Coefficients

The relative concentration profile for I^- is calculated according to the method described by (Cavé et al., 2009; Tidwell et al., 2000):

$$\left(\frac{C}{C_0}\right)_{x\_t} = \frac{\Delta\mu_{x\_t}}{\Delta\mu_{x\_sat}} \quad (2.16)$$

where:

t is the acquisition time for any given Δμ profile.

Using a least-squares method, the $(\frac{C}{C_0})$ profiles for each acquisition time were fit to an analytical solution of Fick's second law to determine D_p values:

$$\left(\frac{C}{C_0}\right)_{x\_t} = \text{erfc}\ \left[\frac{x}{2\sqrt{D_{p-I}t}}\right] \quad (2.17)$$

where:

C = the tracer concentration at distance x (m) from the influx boundary and time t (s) since the start of diffusion,

C_0 = the constant initial concentration of the tracer at the influx boundary,

D_{P-I} = the pore-water diffusion coefficient for the conservative tracer I^- ($m^2\,s^{-1}$),

erfc = the complementary Gaussian error function.

The effective diffusion coefficient (D_e) was calculated from ϕ_I and D_P:

$$D_e = \phi_I \cdot D_{p-I} \quad (2.18)$$

where:

ϕ_I is the average of the spatially-resolved ϕ_{x_I} values.

2.2.10.5. Cesium Tracer Concentrations

Consistent with Loomer et al, (2013), the relative concentration profiles for Cs^+ at specific acquisition times were calculated as a function of $\Delta\mu_{x\_t}$ using the slope of the calibration function (m), the initial Cs^+ concentration at the influx boundary (C_0) and the bulk ϕ_w value for the shale:

$$\left(\frac{C}{C_0}\right)_{x\_t} = \frac{\Delta\mu_{x\_t}}{\phi_w\, m\, C_0} \quad (2\text{-}19)$$

The $\Delta\mu_{x,t}$ values reflect the total mass of Cs^+ in the sample, which includes aqueous and adsorbed mass, so the $\left(\frac{C}{C_0}\right)_{x\_t}$ values in the rock sample are expected to exceed the constant boundary value of 1.0 mol/L.

2.2.10.6. Diffusion-Reaction Simulations

For clay-bearing rocks (e.g. shale), reactive species such as Cs^+ are affected by sorption reactions (Bradbury and Baeyens, 2000; Fuller et al., 2015; Takahashi et al., 2017). Consequently, reactive-transport modeling was used to simulate Cs^+ transport and estimate the diffusion/reaction parameters D_{p-Cs} and cation exchange capacity (CEC). The MIN3P code (Mayer, 1999) was used (version Min3p-HPC-X64v.2.1.26.786; (Mayer et al., 2015) which includes multi-site ion exchange (MIE). This work uses a one-dimensional MIE approach whereby ion exchange occurs at frayed-edge sites (FES), planar sites (PS) and type II sites according to the description provided by previous researchers (Bradbury and Baeyens, 2011; Bradbury and Baeyens, 2000; Maes et al., 2008; Steefel et al., 2003; Van Loon et al., 2009; Xie et al., 2015; Zachara et al., 2002). This model assumes that Cs^+ adsorption is dominated by illite and that the fractions of the total CEC are 0.25%, 20%, and 79.75% for FES, type II and PS sites respectively (Bradbury and Baeyens, 2000). Values of $logk_{Cs^+/Na^+}$ equal to 7.0, 3.6, and 1.6 for the Cs^+–Na^+ exchange reactions at FES, type II, and PS sites, respectively, were used in the simulations.

Following the methods described by Loomer et al. (2013), the parameter estimation code, PEST version 7.05, (Doherty, 2018) was used with the MIN3P code to estimate values for D_{P-Cs} and CEC. Briefly, initial values were assigned for D_{P-Cs} and CEC, then MIN3P was used to simulate the Cs^+ relative concentration profile. PEST was used to compare the fit between the simulated and experimental profiles and iteratively adjust the D_{P-Cs} and CEC values until a satisfactory fit was achieved. The model parameters, including initial conditions, boundary conditions and the fit

criteria are provided in Table 2.7. MIN3P was operated with transport by diffusion only, combined with MIE equilibria. In the simulation, ion-exchange reactions were limited to Cs^+ exchange with Na^+, as Na is the dominant cation in the SPW. MIN3P uses the Gaines-Thomas convention whereby mass action for ion exchange is based on equivalent fractions (Appelo and Postma, 2004; Mayer, 1999). Ion activity coefficients for aqueous species were calculated based on the HW model (Harvie et al., 1984) using interaction parameters presented in Table 2.8.

Table 2.7. Selected parameters used in reactive transport code, MIN3P

Model Parameters	**Samples**		
	DGR3c	**DGR3j**	**DGR3g**
Number of control volumes	13	13	15
Domain Length (m)	1.63×10^{-2}	1.625×10^{-2}	1.688×10^{-2}
Transport boundary conditions on both ends of the domain	First type	First type	First type
Tracer concentration at influx boundary (M)	1.0	1.0	1.0
Minimum time step (hrs)	2.4×10^{-7}	2.4×10^{-7}	2.4×10^{-7}
Water accessible porosity	0.0743	0.0989	0.0989
Dry bulk density (gcm^{-3})	2.54	2.54	2.54

*Ion exchange sites in each cell were initially equilibrated with the SPW composition

Table 2.8. Ion-interaction parameters used in the model

Ion pair	$\boldsymbol{\theta^{-}}$	$\boldsymbol{C_0^{-}}$	$\boldsymbol{\beta_0^{-}}$	$\boldsymbol{\beta_1}$	**Reference**
Binary coefficients					
$Cs^+ Cl^-$		0.00038	0.03	0.0558	(Pitzer and Mayorga, 1973)
$Cs^+ SO_4^{-2}$		0.00004	0.0888	1.11075	
Cs^+OH^-		-0.0599803	0.15	0.3	
$Cs^+ Na^+$	-0.033				(Pitzer and Kim, 1993)
$Cs^+ K^+$	0.00				
$Cs^+ H^+$	-0.044				
Ion group	$\psi(\times 10^{-3})$				
Ternary coefficients					
$Cs^+Na^+Cl^-$	-0.003				(Pitzer and Kim, 1993)
$Cs^+K^+Cl^-$	-0.0013				
$Cs^+H^+Cl^-$	-0.019				

2.3. Results

2.3.1. Mineralogical and Textural Analysis

An image of the thin section prepared from slice 1 (Fig. 2.8a), corresponding to samples DGR3a, b, e, g and j (Table 2.1) indicates that alternating oxidized (maroon) and reduced (green) layers occur parallel to bedding.

Scanned images of DGR3c from slice 2 (Table 2.1; Fig. 2.8b) displaying mostly reduced layers (green) occurs parallel to bedding. The layers in thin section prepared from slice 2 are less observable relative to the thin section prepared from slice 1. The crack separating the upper and lower arrows in DGR3c, was created during the thin section preparation, not a property of the sample.

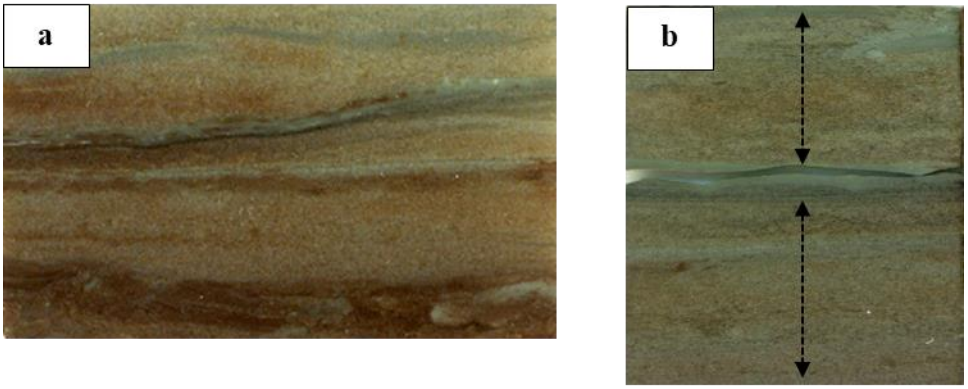

Figure 2.8. Scanned images of Queenston Formation shale, a) slice 1, b) slice 2

The SEM analysis indicates that the samples are composed mainly of primary detrital quartz and feldspar with clay minerals in the inter-granular space (Fig. 2.9). Lesser amounts of amphibole, apatite, rutile, pyrite, chlorite, organic matter and biotite are also observed. Calcite and dolomite

are abundant as primary detrital grains and as secondary cements. Gypsum is observed in some samples as a secondary cement.

The subcores drilled for diffusion experiments are from two contiguous slices of the larger drill core and all except one of the diffusion samples (DGR3c) are from slice 1 (Table 2.1). Gypsum is much more common in DGR3c where it fills voids leaving very little open void space (Fig. 2.10). Pore spaces are manifest as dark-grey to black regions in the SEM images, and they occur as small (< 1 μm) features that are disseminated throughout the material, most commonly interstitial among the primary grains and the cementing carbonate and gypsum. At high magnification, clay minerals are observed in these interstitial regions (Fig.2.11), demonstrating that the pores are much less than 1 μm, consistent with pore-size distribution data presented by Celejewski et al. (2018).

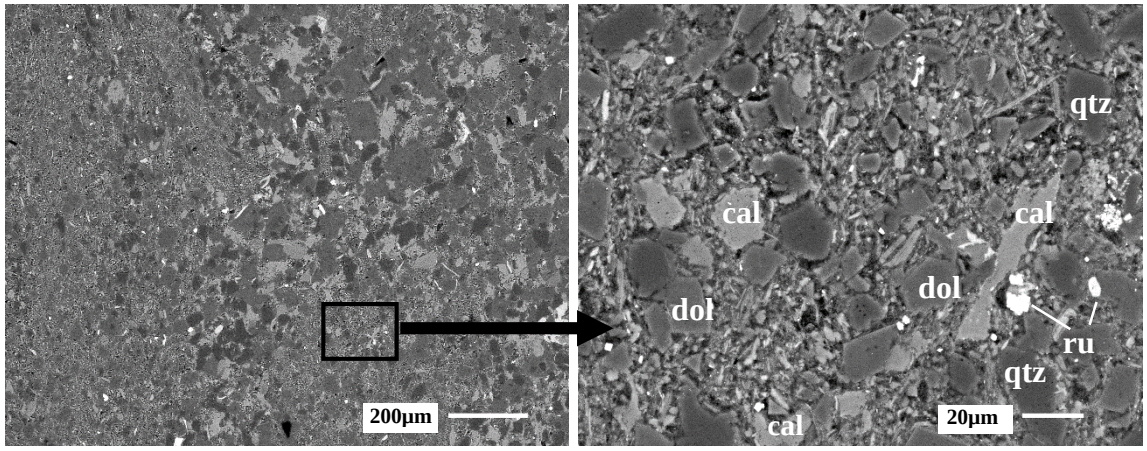

Figure 2.9. Representative SEM images from Queenston shale sample illustrating the grain-size and mineralogy characteristics of the material, cal: calcite, dol: dolomite, ru: rutile, qtz: quartz

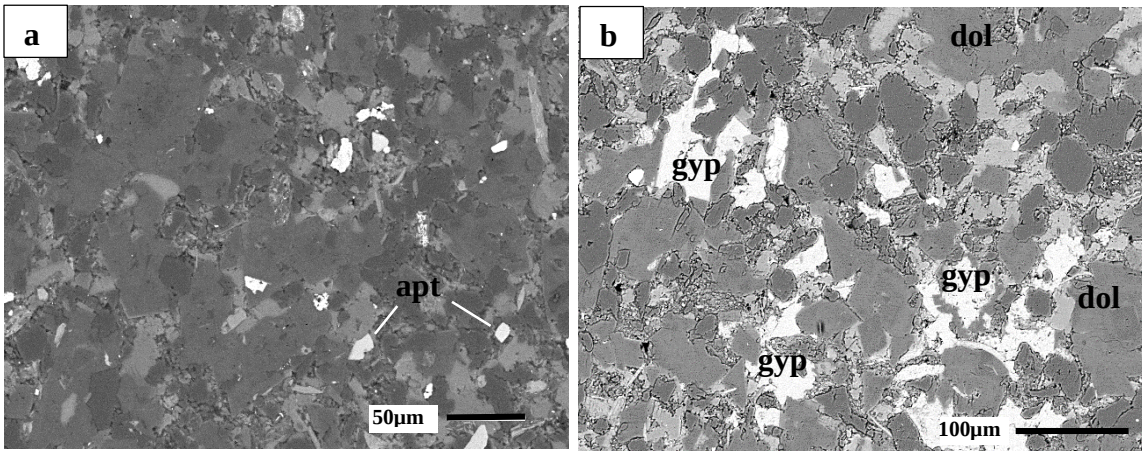

Figure 2.10. SEM images from a) slice 1 and b) slice 2; gypsum commonly fills voids in material from slice 2 but is generally absent from slice 1.

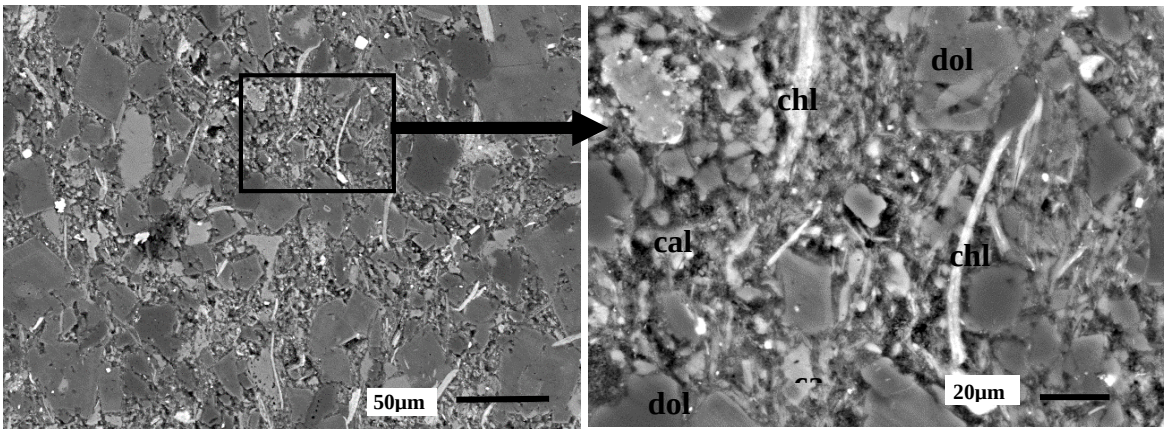

Figure 2.11. Representative SEM images of Queenston shale with voids dominated by clay infill.

2.3.2. Water-Accessible Porosity and Grain Density

The measurements of ϕ_w range from 0.0743 to 0.0989 (Table 2.9) which is within the range of measurements reported by Xiang et al. (2013) for the Queenston Formation shale. The ρ_{gr} values range from 2.81 to 2.86 which is consistent with expectations based on the primary mineralogy (quartz ρ = 2.62, K-feldspar ρ = 2.56, calcite ρ = 2.71, dolomite ρ = 2.84) combined with some relatively dense accessory minerals (hematite, pyrite, rutile, apatite).

Table 2. 9. Water-accessible porosity and grain density for Queenston shale

Sample	$\boldsymbol{\phi_w}$	$\boldsymbol{\rho_{gr}}$ $(\boldsymbol{gcm^{-3}})$	**Diffusion experiment**
Slice 1	0.0989±0.0006	2.86±0.005	DGR3a, DGR3b, DGR3e, DGR3g, DGR3j
Slice 2	0.0743±0.0017	2.81±0.003	Dgr3c

2.3.3. Diffusion Experiments

2.3.3.1. Calibration

2.3.3.1.1. Beam Hardening Effect

The spectrometry data for I^- solutions contained in plastic and ceramic vials define linear relationships with slopes that differ by only 0.9% (Fig. 2.12a) while the data for Cs^+ tracer solutions display a 12% difference in slope (Fig.2.12b). In comparison, Loomer et al. (2013) conducted a similar experiment with the radiography method and they report a difference in slope of 43% for I^- and 49% for Cs^+. The 12% difference in slope obtained with spectrometry may be at least partially attributable to beam hardening, but Cs^+ is a reactive solute and adsorption of Cs^+ on the inner surface of the ceramic vials could also explain the difference in slopes. However, I^- is a non-reactive tracer and the similarity in slope for the plastic and the ceramic vials indicates that beam hardening effects are minimal.

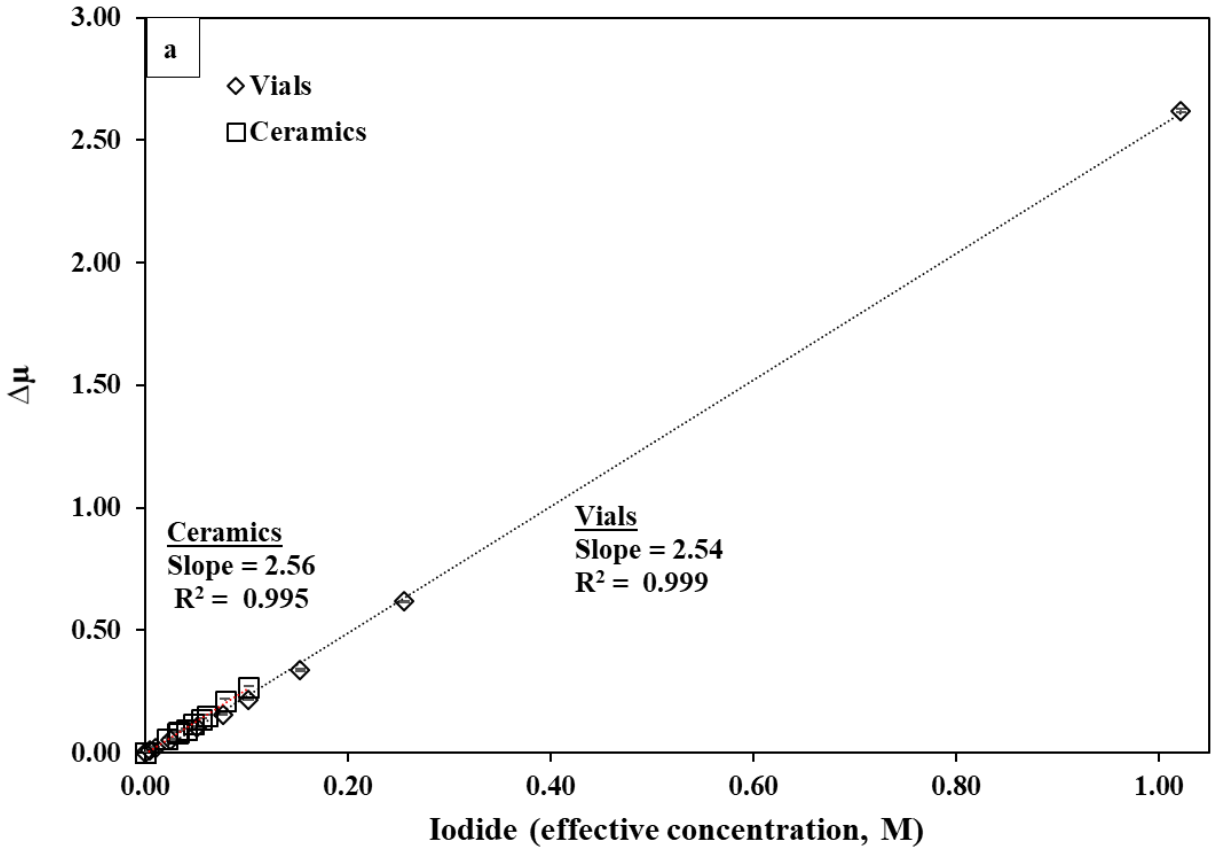

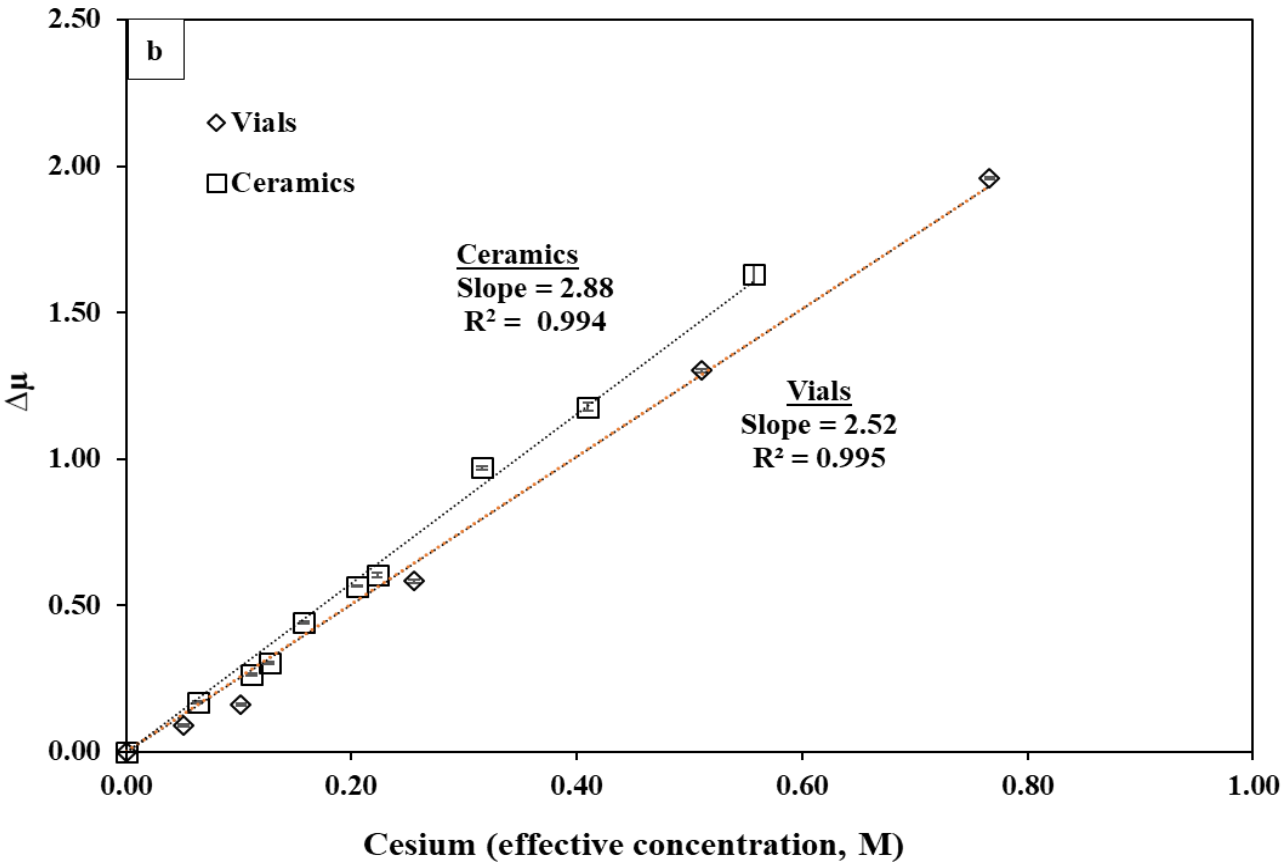

Figure 2.12. Δμ profile versus different tracer concentration developed for a) I^- and b) Cs^+ to test for beam hardening effects. The slopes of linear regressions for datasets collected in plastic and ceramic vials are very similar indicating minimal effects from beam hardening. The vertical error bars reflect propagation of error as described in section 2.2.10.2.

2.3.3.1.2. Iodide and Cesium Calibration

The calibration curves for I^- and Cs^+ are presented in Figure 2.13. Based on the known tracer mass, the absorption is identified and then the linear slop value is used for calculating the ϕ_I and Cs^+ relative concentration (sections 2.2.10.3 and 2.2.10.5).

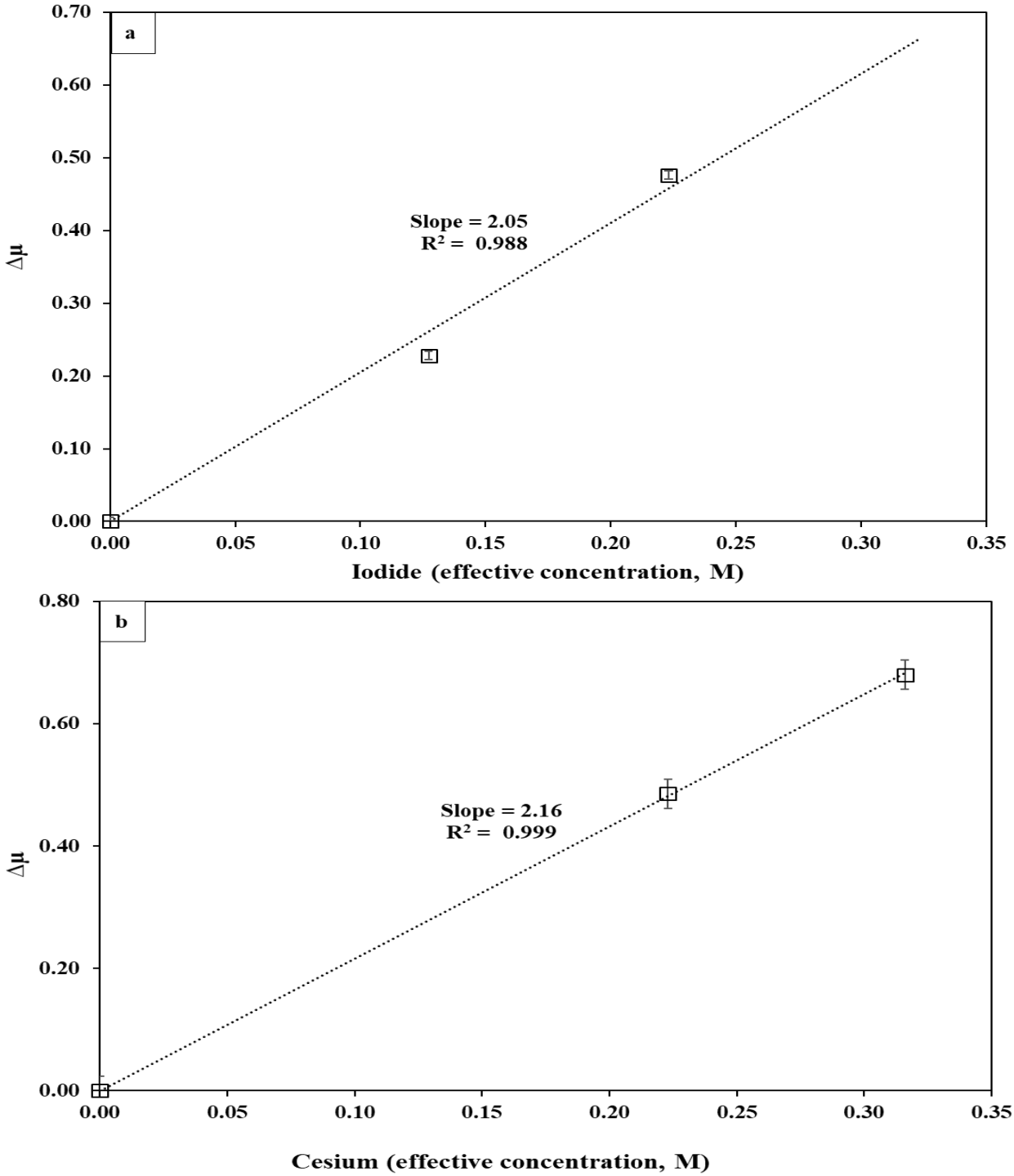

Figure 2.13. Calibration curves relating Δμ to effective concentration for a) I^- and b) Cs^+. The vertical error bars reflect propagation of error as described in section 2.2.10.2.

2.3.3.2. Iodide Tracer Diffusion

The multiple experimental measurement times (circles) reflect the movement of the tracer along the diffusion direction (Figure 2.14). The experimental and modelled profiles for I^- diffusion measurements provided in Figure 2.14 were fit to calculate D_{P-I}. A good fit is generally observed between model and experimental C/C_0 profiles, although the fit is best for profiles measured at times > 24 hrs. The estimated diffusion coefficients are similar for all three samples: for DGR3a, the estimated D_{P-I} values range from 8.8×10^{-12} to 4.2×10^{-11} m^2/s, with an average of 2.8×10^{-11} m^2/s, for DGR3b, values range from 1.2×10^{-12} to 2.8×10^{-11} m^2/s, with an average of 2.1×10^{-11} m^2/s, and for sample DGR3e, estimated values range from 2.0×10^{-12} to 5.5×10^{-11} m^2/s, with an average of 3.5×10^{-11} m^2/s. The breakthrough of I^- tracer at the end of the samples occurs between 140 and 168 hours. All data are provided in Appendix D.

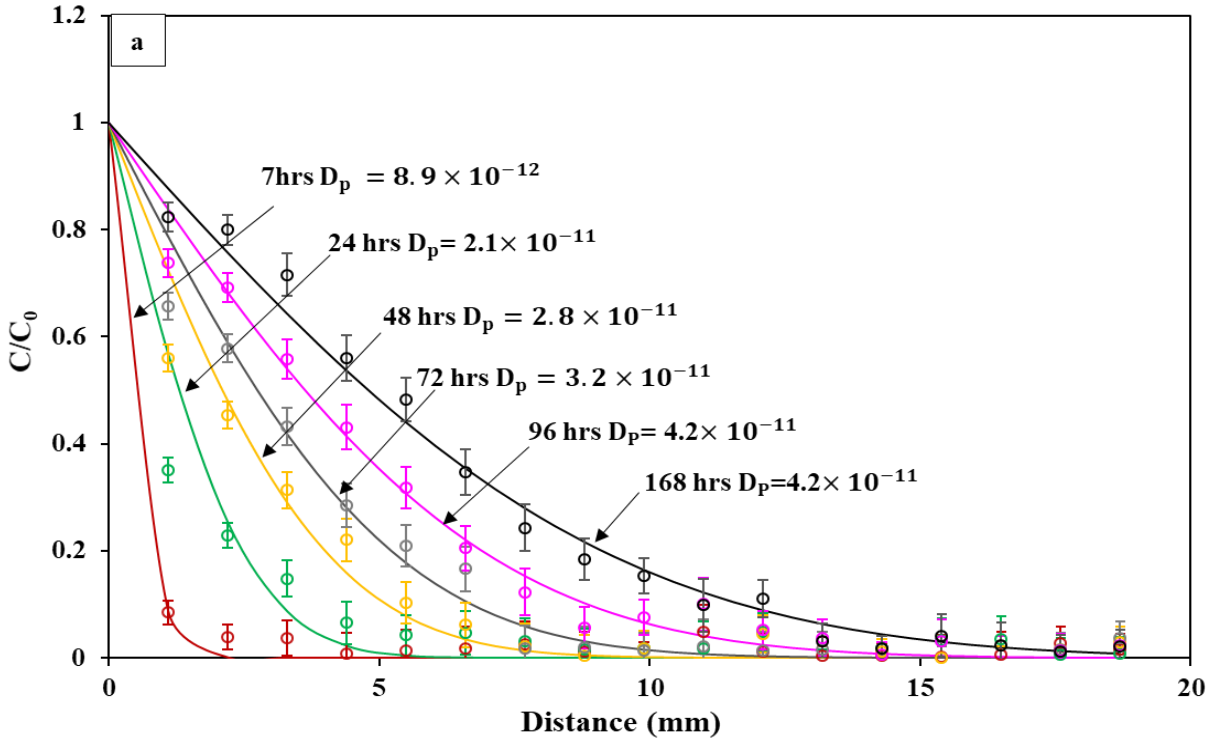

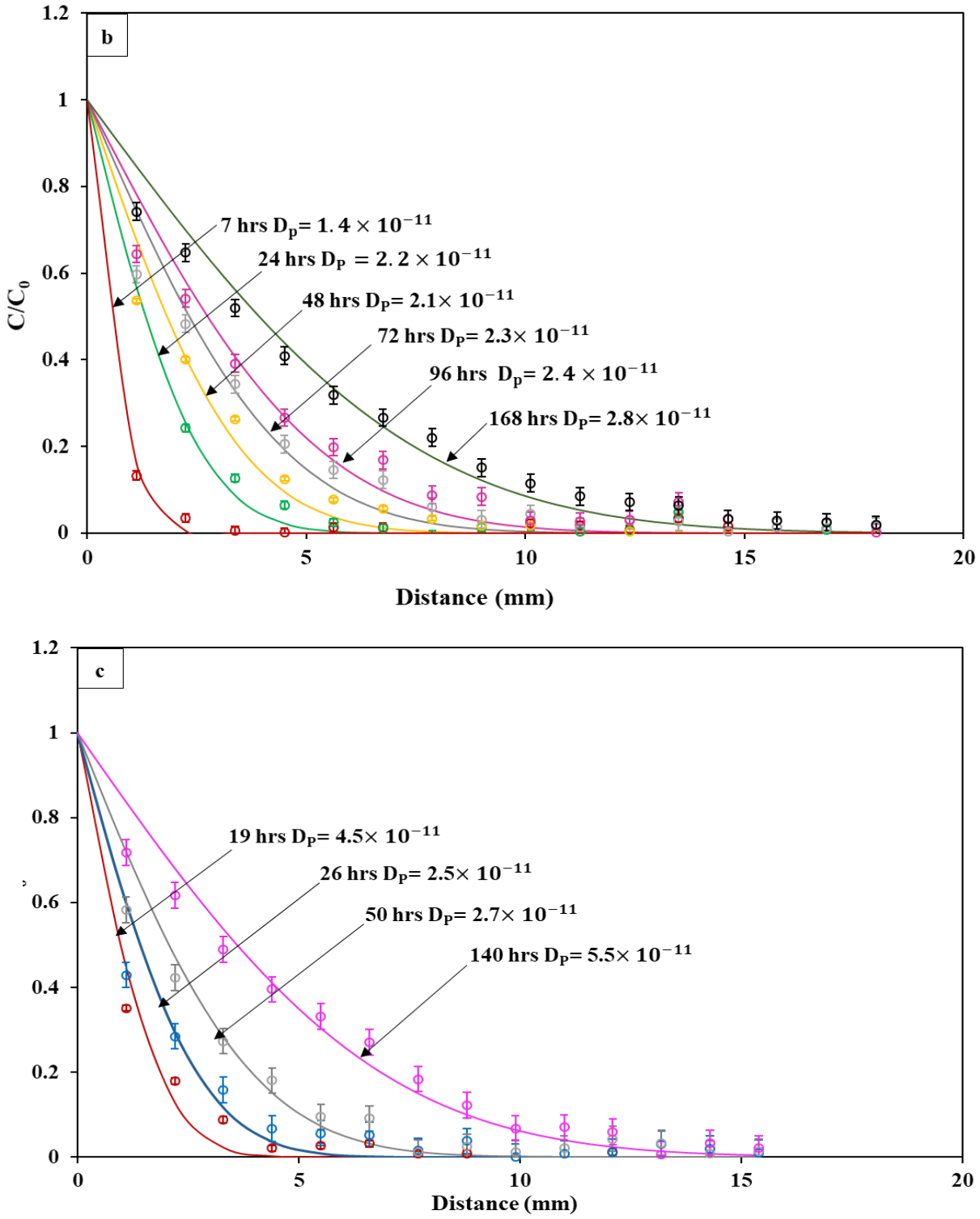

Figure 2.14. Profiles for C/C_0 for I^- in samples a) DGR3a, b) DGR3b and c) DGR3e. Solid lines and circles represent the analytical model and experimental measurements, respectively. The vertical error bars reflect propagation of error as described in section 2.2.10.2.

2.3.3.3. Iodide-Accessible Porosity Measurements

Measurements of the spatially-resolved ϕ_{x_I} values are presented in Figure 2.15 and the corresponding average ϕ_I values range from 0.059 to 0.064 (Table 2.10). All three samples were cored from the same slice (Table 2.1) and the ϕ_{x_I} profiles display similar trends with relatively high values at the top and bottom boundaries, and two internal peaks.

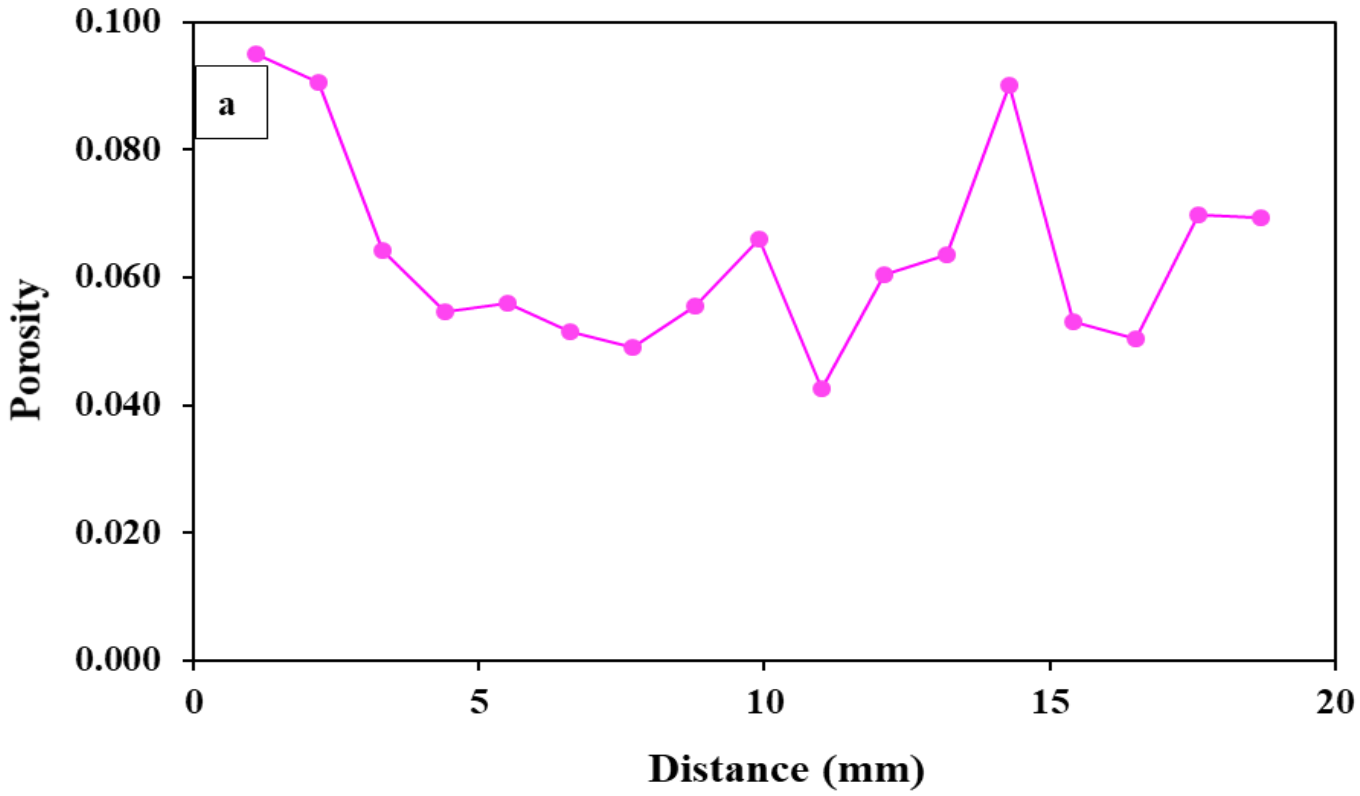

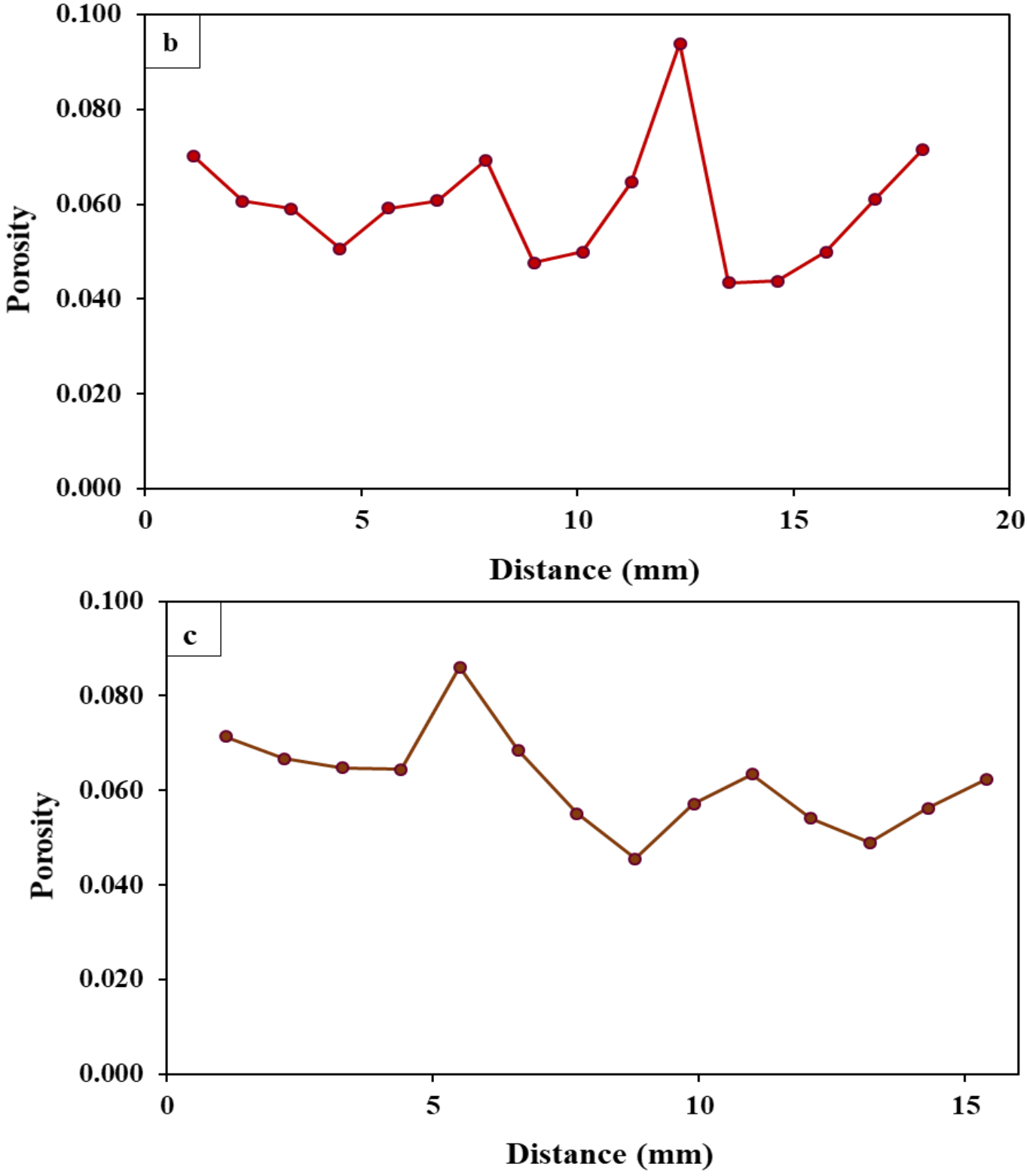

Figure 2.15. One dimensional profiles of ϕ_{x_I} along the length of sample a) DGR3a, b) DGR3b, and c) DGR3e.

2.3.3.4. Cesium Tracer Diffusion

The relative concentration experimental profiles for Cs^+ diffusion measurements are provided in Figure 2.16. The breakthrough of Cs^+ tracer at a distance near the outflux boundary, 16.5 mm, occurred at essentially the same time, 215 hours, for samples DGR3g and DGR3j, but breakthrough was faster for sample DGR3c, 191 hours. Similarly, the C/C_0 values near the influx boundary are significantly higher for samples DGR3g and DGR3j compared to sample DGR3c (Fig. 2.16).

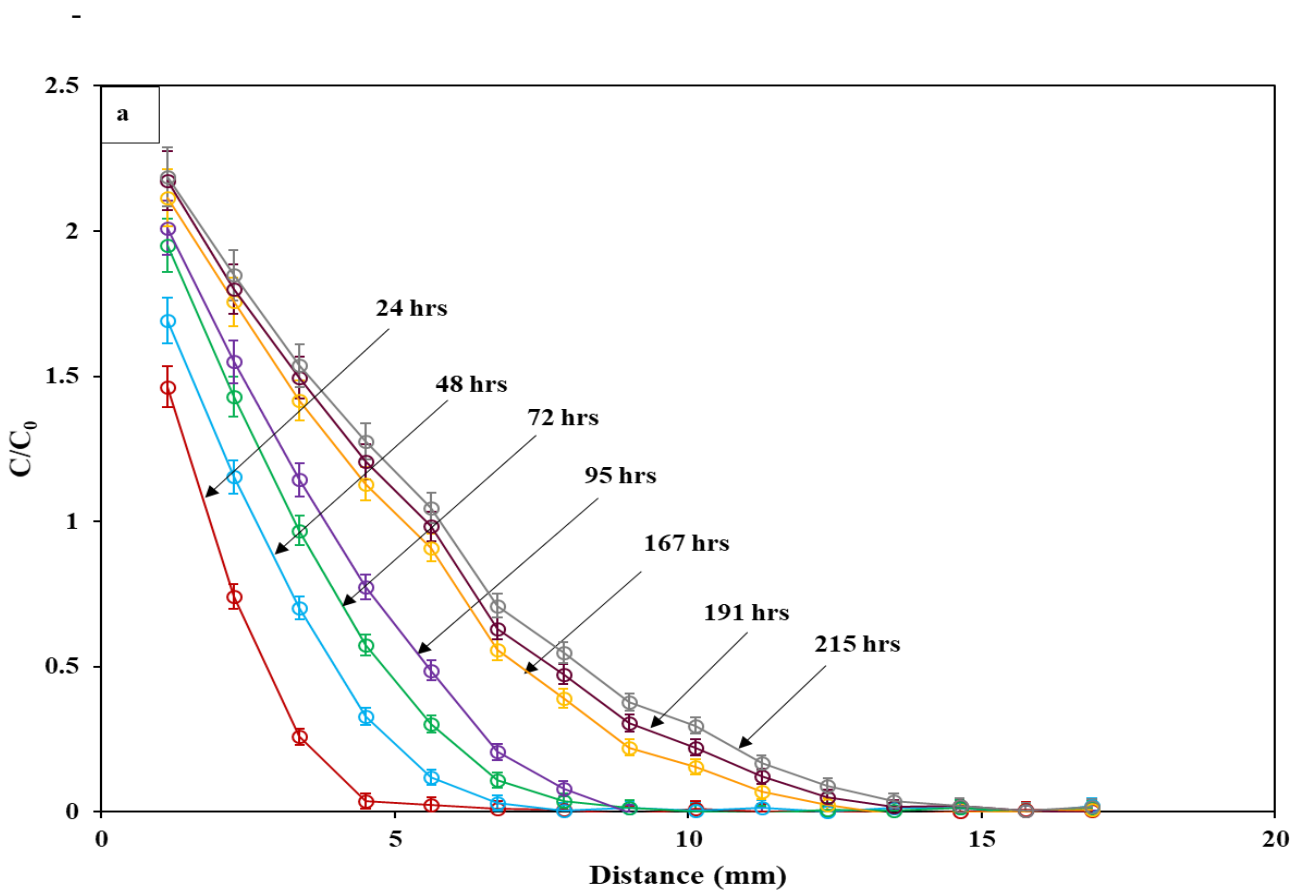

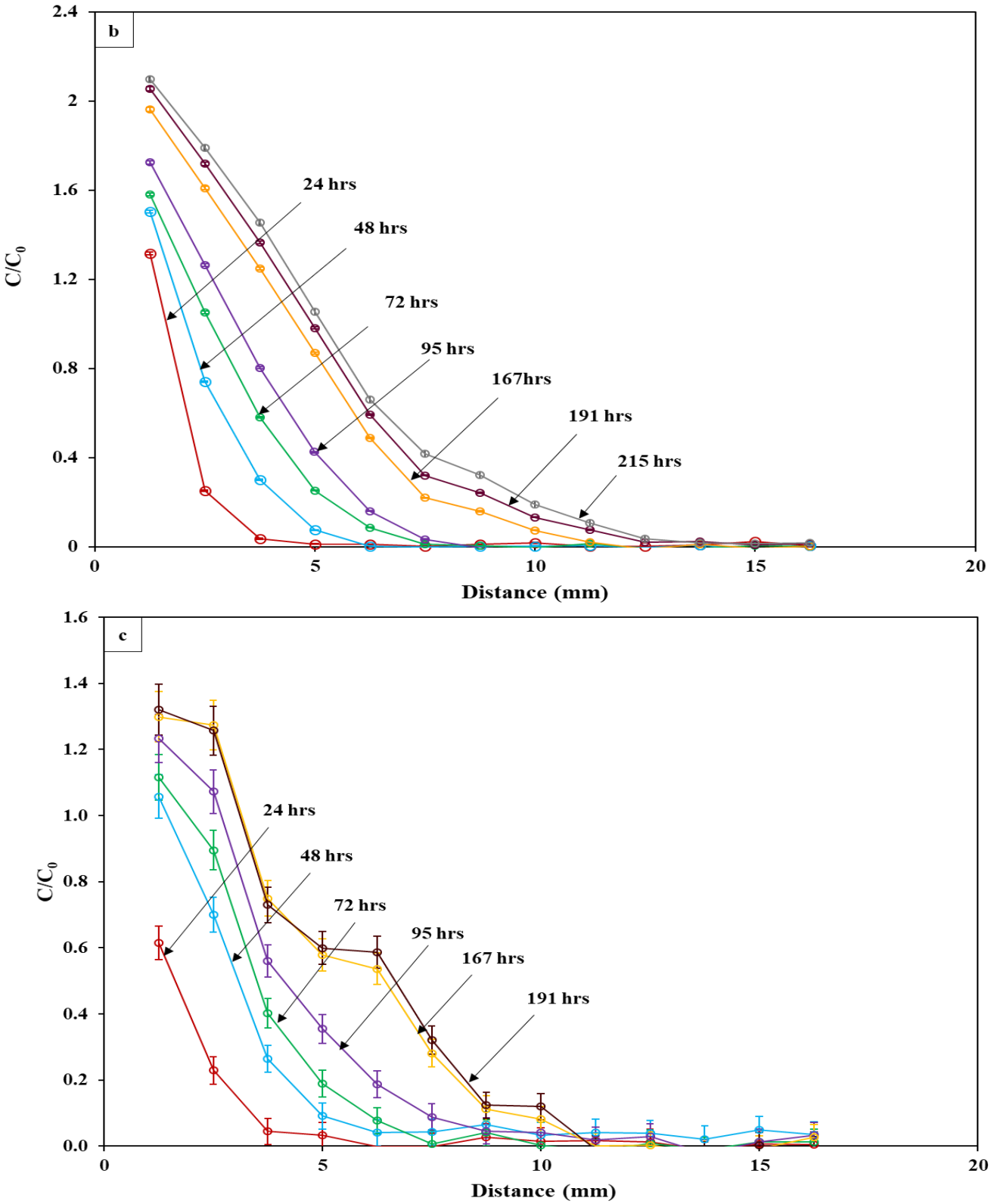

Figure 2.16. The experimental profiles for C/C_0 for Cs+ in sample a) DGR3g-. b) DGR3j, c) DGR3c, the open circles represent experimental measurements obtained by methods outlined in section 2.2.10.5. The vertical error bars reflect propagation of error as described in section 2.2.10.2.

2.3.3.5. Diffusion-Reaction Simulations

The modelled fits to the experimental profiles for Cs^+ diffusion are provided in Figure 2.17. A good fit is generally observed. The D_{P-Cs}values range from 2.65×10^{-11} m^2s^{-1} (sample DGR3c) to 4.37 $\times10^{-11}$ m^2s^{-1} (DGR3j) to 5.69 $\times10^{-11}$ m^2s^{-1} (DGR3g). Sample DGR3c which has the lowest D_{P-Cs}value also has the lowest CEC value, 1.00 meq/100g, while CEC values are 6.97 meq/100g and 7.11 meq/100g for samples DGR3j and DGR3g respectively.

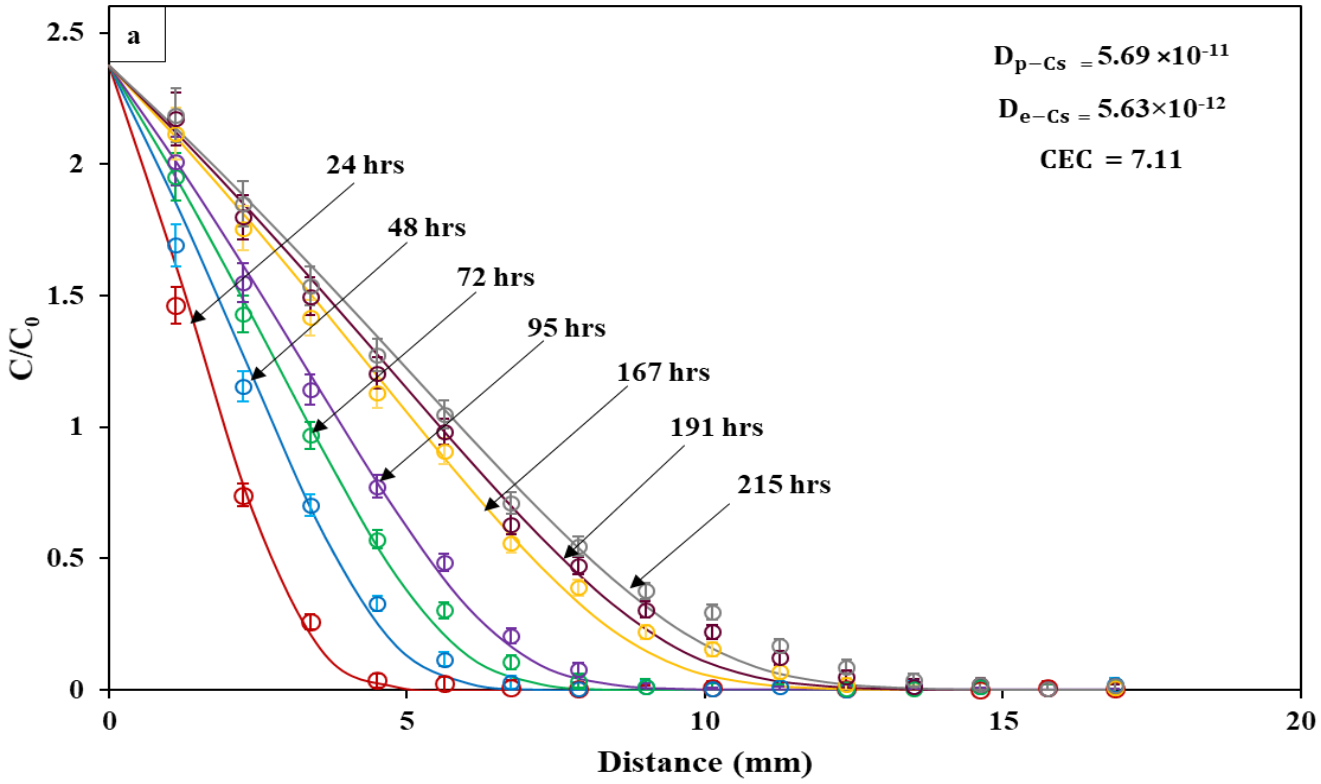

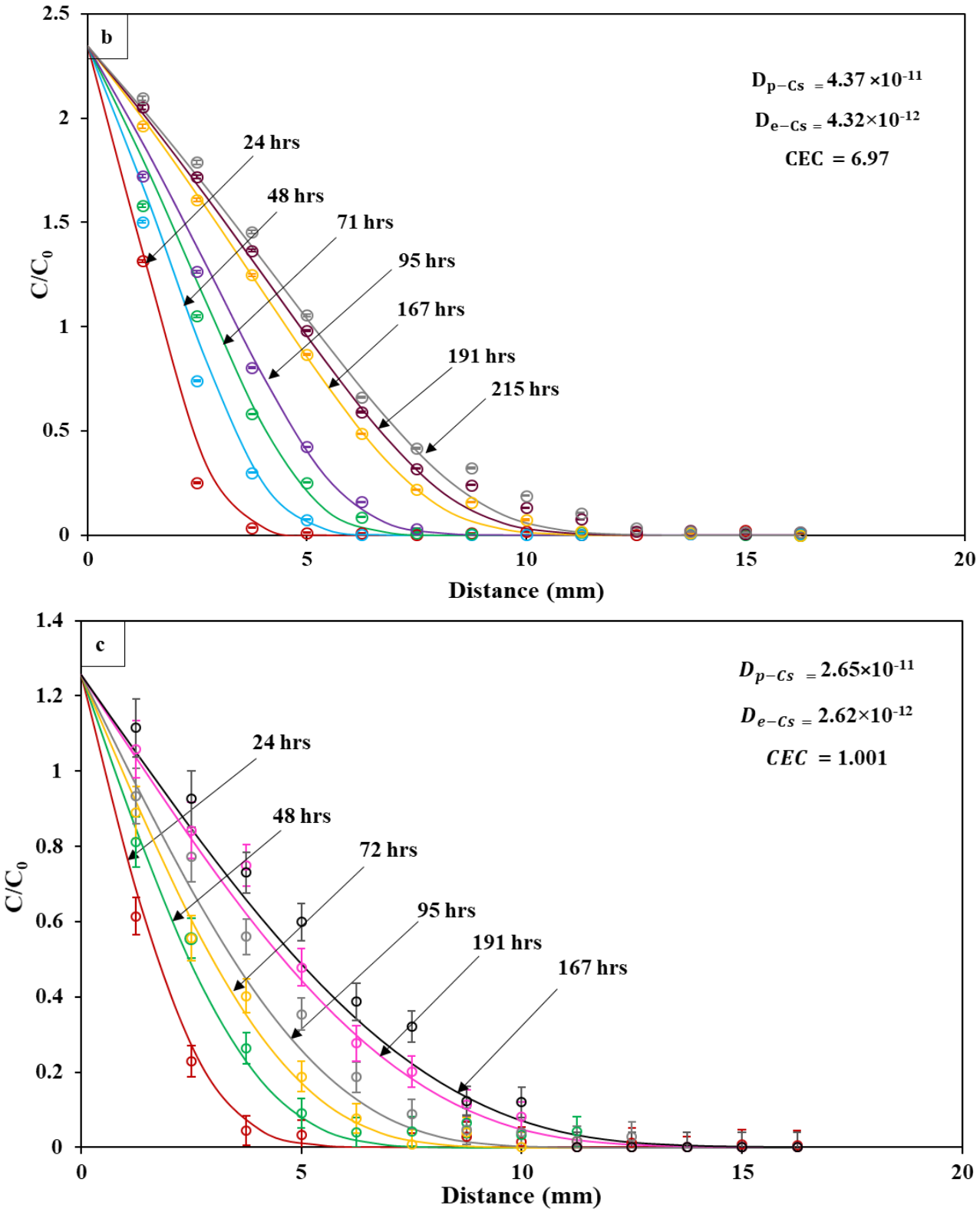

Figure 2.17. Comparison of the experimental C/C_0 profiles for Cs+ (circles) against the best-fit simulated profiles (solid lines), a) DGR3g-. b) DGR3j, c) DGR3c. The vertical error bars reflect propagation of error as described in section 2.2.10.2.

2.4. Discussion

2.4.1 Iodide Diffusion

The D_{p-I} values obtained by spectrometry display variation at different time steps during the experiment. This variability likely reflects spatial heterogeneity in the material properties of the samples and as time progresses, the tracer advances to contact the changing material properties. A comparison of the data from the spectrometry method with results from previous diffusion measurements on Queenston Formation shale is presented in Table 2.10 and Figure 2.18. The previously reported measurements were conducted using radiography (Al et al. 2010; Cavé et al. 2010, Cavé et al. 2009a; Loomer et al. 2013; Xiang et al. 2013) and through-diffusion methods (Cavé et al. 2010; Vilks and Miller, 2007; Xiang et al. 2013). The comparison demonstrates that the XAS method provides data that are consistent with radiography and through diffusion.

The average ϕ_I values determined for each sample are approximately 40% lower than the bulk ϕ_w value measured for the same material (Table 2.10). This discrepancy is commonly observed in clay-rich rocks and is attributed to anion exclusion (Altmann et al., 2012; Cavé et al., 2010; Smith et al., 2004; Tachi et al., 2011; Wigger et al., 2018). The ϕ_I values were used to transform D_p to D_e and the values are presented in Table 2.10.

Table 2.10. Comparison of porosity and diffusion coefficients for I^- measured by spectrometry (this study) with values measured by radiography and through diffusion from previous studies

Sample	ϕ_w	D_P ($\times\ 10^{-11} m^2 s^{-1}$)	ϕ_I	D_e ($\times\ 10^{-12} m^2 s^{-1}$)	Method
Queenston (DGR3a-525.86)		3.70±0.62	0.064	2.35	
Queenston (DGR3e-525.86)	0.0989	3.96±0.14	0.062	2.45	Spectrometry
Queenston (DGR3b-525.86)		2.40±0.22	0.059	1.43	
Queenston (DGR3-525)[a]	0.084	4.37±0.04	0.048	2.1	
Queenston (DGR3-468)[a]	0.109	5.6±0.06	0.060	3.4	
Queenston (DGR3-506)[a]	0.058	2.7±0.04	0.048	1.3	
Queenston (DGR3-517)[a]	0.09	5.0±0.04	0.044	2.6	Radiography
Queenston (DGR3-556)[a]	0.078	4.09±0.04	0.048	1.8	
Queenston (DGR3a-468)[b]	0.109	4.3±0.6	0.078	3.4	
Queenston (DGR3b-468)[b]	0.109	4.5±0.2	0.078	3.5	
Queenston (DGR3c-468)[b]	0.109	2.6±0.1	0.072	1.9	

Queenston (DGR3-468.02)[c]	0.109	5.71	0.042	2.4	
Queenston (DGR3-525.86)[c]	0.084	2.94	0.033	0.97	
Queenston (DGR3-506.64)[c]	0.058	2.70	0.033	0.89	
Queenston (DGR-78)[d]	0.062	6.0	0.05	4.4	
Queenston (DGR-78)[d]	0.062	5.0	0. 05	3.1	
Queenston (DGR-583.18)[e]	0.087	3.0	0.061	1.8	
Queenston (DGR-593.53)[e]	0.083	2.70	0.041	1.1	
Queenston (DGR-620.95)[e]	0.089	2.0	0.046	0.91	
Queenston (DGR-456)[f]	0.090	2.9	0.094	2.6	
Queenston (078)[g]	0.063	3.1	0.041	0.13	
Queenston (084)[g]	0.063	2.1	0.049	1.0	Through diffusion
Queenston (105)[g]	0.063	3.0	0.029	0.87	
Queenston (DGR-597.25)[h]	0.082	3.0	0.073	2.2	
Queenston (DGR-620.93)[h]	0.089	1.30	0.065	0.85	

a Xiang et al. (2013); b Loomer et al. (2013); c Al et al. (2010); d Cavé et al. (2009); e Cavé et al. (2010); f Xiang et al. (2013); g Vilks and Miller (2007); h Cavé et al. (2010)

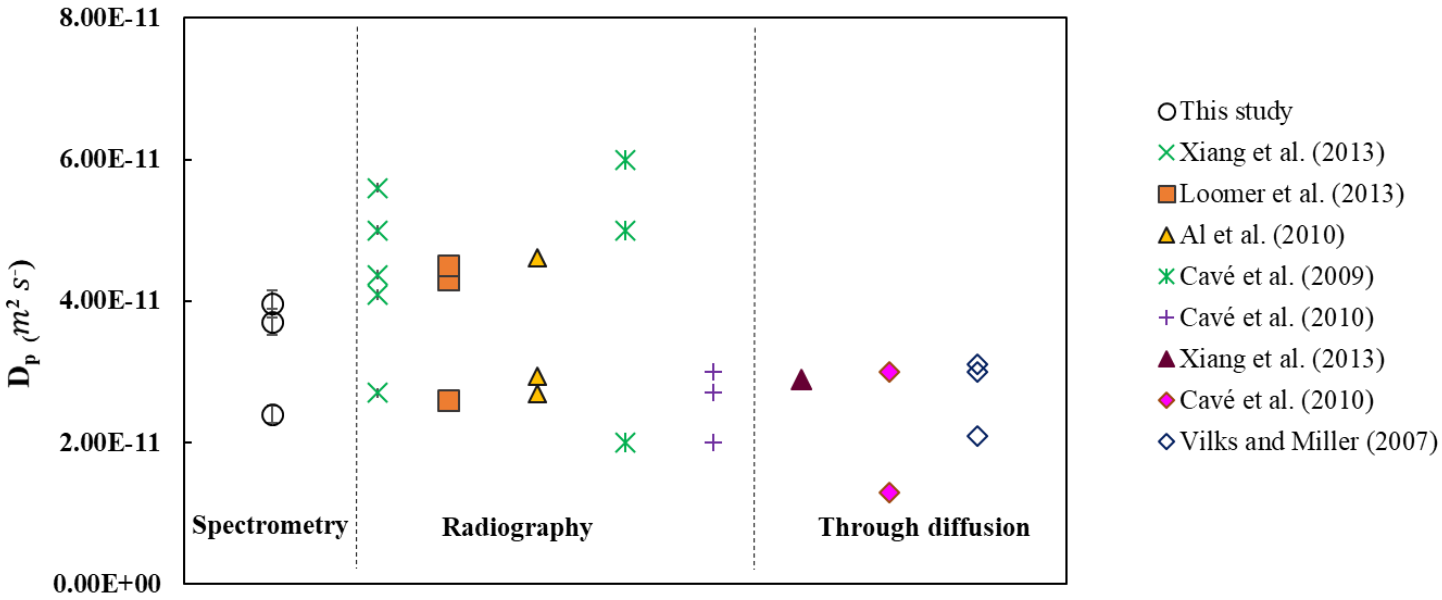

Figure 2.18. Plot of D_p measured with iodide tracer to compare the results from this study with the other literature worked on the similar Queenston shale.

2.4.2 Cesium Diffusion/reaction

There are clear differences among samples in the magnitude of the C/C_0 values near the influx boundaries, as well as the breakthrough times, $D_{p\text{-}Cs}$ and CEC values (Figs. 2.16 and 2.17), with sample DGR3c standing out as distinct from the others. These differences are primarily due to spatial heterogeneity in mineralogy. Sample DGR3c and samples DGR3g/DGR3j are from different slices of the original drill core, and gypsum infills much of the pore space for sample DGR3c, while the pore spaces in samples DGR3g and DGR3j are lined with clay minerals (Figs 2. 9 - 2.11). The presence of gypsum in the pores of sample DGR3c decreases the surface area of clay minerals available for adsorption of Cs^+, thereby providing an explanation for the relatively low CEC and the relatively low C/C_0 values near the influx boundary. Similarly, the occurrence of gypsum cement in the pore space is likely to decrease the tortuosity factor, thereby contributing

to the relative decrease in $D_{p\text{-}Cs}$ observed for sample DGR3c. The breakthrough time for sample DGR3c is relatively fast compared to DGR3g and DGR3j, which appears to be inconsistent with the lower value for $D_{p\text{-}Cs}$, however, the rate of solute transport is a function of both D_p and CEC, and it is apparent that the decrease in Cs^+ attenuation by adsorption that results from the lower CEC allows for the faster breakthrough time, despite the lower $D_{p\text{-}Cs}$.

The results obtained in this study using the spectrometry method compare very well with the results obtained by Loomer et al. (2013) that were obtained by X-ray radiography (Table 2.11). Loomer et al., (2013) reported breakthrough of Cs^+ after approximately 215 hours at a distance of 16.4 mm from the influx boundary, essentially identical to the results obtained in this study for samples DGR3g and DGR3j. Similarly, the $D_{p\text{-}Cs}$ (7.0×10^{-11} to 7.4×10^{-11} m^2/s) and CEC values (8 to 8.7 meq/100g) obtained by Loomer et al. (2013) compare well with the measurements from the present study for the two samples that do not contain gypsum cements. Loomer et al. (2013) did not report gypsum cementing of the pore space as was noted here for sample DGR3c, so the present work provides valuable information about the range of values that might be expected due to material heterogeneity**.**

Table 2.11. Diffusion – sorption values on clay –bearing rocks for Cs^+ from the literature, compared with other studies

Material	D_{p-Cs} ($\times 10^{-11} m^2 s^-$)	Log $ks_{Cs/Na}$	ϕ_w	Total CEC (meq/100g)	Site capacity (of the CEC) (meq/100g)	D_{e-Cs} ($\times 10^{-12} m^2 s^-$)	Ionic strength	Illite content (wt%)	C_0 (M)	Ion exchange site
Reference illite[a]	—	7,3.6,1.6	—	20	0.0025(0.25%),0.2(19.95%), 0.7975(79.80%)	—	0.1	—	10^{-10}-10^{-3}	FES, Type II, Ps
Queenston Fm. (DGR3c)[b]	2.65		0.0743	1.001		2.62				
Queenston Fm. (DGR3j)[b]	4.37	7,[a]3.6[a],1.6[a]	0.0989	6.97	0.0025(0.25%)[a],0.2(19.95%)[a], 0.7975(79.80%)[a]	4.32	8.3	40-50	10^0	FES, Type II, Ps
Queenston Fm. (DGR3g)[b]	5.69		0.0989	7.11		5.63				
Queenston Fm. (Canada)[c]	7.70	1.5	0.109	8.5	—	8.40	8.3	40-50	10^0	X
	7.70	1.5		8.7		8.40				
	7.40	1.6		8		8.10				

a Bradbury and Baeyens (2000)

b This study

c loomer et al. (2013)

As mentioned in the Methods, the MIE model (or three-site cation exchange model), based on "reference illite" as reported by Bradbury and Baeyens (2000) was applied in this work to simulate Cs^+ adsorption. The MIE model recognizes a concentration dependent preference for Cs^+ selectivity against competitively adsorbing ions (e.g. Na^+, K^+ , Rb^+, Ca^+ and Mg^{2+}) (Bradbury and Baeyens, 2000; Jakob et al., 2009; Tachi et al., 2011; Tachi et al., 2009). In general, it is reported that the FES sites dominate Cs^+ exchange at Cs^+ concentrations up to 10^{-8} M, while type II site dominate from 10^{-8} M to 10^{-5} M and planar sites dominate at higher Cs^+ concentrations. The Cs^+ tracer concentration used in this study was 1 M and therefore far exceeded the concentration ranges where FES and type-II sites control Cs^+ exchange. In future work it would be worthwhile to conduct similar experiments at lower Cs concentrations in order to properly test the MIE model.

2.5. Conclusion

A non-destructive novel XAS technique has been developed to quantify diffusion and diffusion-reaction parameters in low permeability clay-bearing rocks, like the Queenston shale formation. This technique resolves the spatial distribution of reactive and conservative species in the porewater of rock samples based on measured X-ray attenuation at the K-edges for I^- and Cs^+ absorption in the energy spectra. I^- and Cs^+ diffusive transport along a concentration gradient in the porewater was monitored as a function of X-ray attenuation ($\Delta\mu$), producing a spatial profile of the tracer concentration versus transport distance. The generation of concentration profiles at multiple time steps allowed the calculation of diffusion coefficients by fitting an analytical solution of Fick's Second Law to the concentration profiles for I^- (D_{p-I}) or numerical simulations for combined diffusion/reaction processes to the concentration profiles of Cs^+ (D_{p-Cs} and CEC). The results are in good agreement with previously published data measured using radiography and through-diffusion techniques.

Measurements of the spatially-resolved ϕ_{x_I} value ranging from 0.059-0.064 are consistent with the other data measured using radiography and through-diffusion techniques.

Relatively high values were obtained for D_{e-Cs}, (2.62×10^{-12} to $5.63\times 10^{-12} m^2 s^-$) in comparison with D_{e-I}, (1.43×10^{-12} to $2.45\times 10^{-12}\ m^2 s^-$), reflecting the lower accessibility for anionic species to porewater in the electric double layer and in the interlayer porosity of clay minerals (anion exclusion).

Another notable outcome of this study is that the beam hardening effect present in the $\Delta\mu$ calibration for radiography is not seen in spectroscopy, since the difference in slopes of standard materials is minimized due to the specific energy range used in this method.

2.6. References

Agbogun, H., Hussein, E. M., and Al, T. A., 2013, Assessment of x-ray micro-CT measurements of porosity and solute concentration distributions during diffusion in porous geologic media: Journal of Porous Media, v. 16, no. 8, p. 683-694.

Al, T., Clark, I., Kennell, L., Jensen, M., and Raven, K., 2015, Geochemical evolution and residence time of porewater in low-permeability rocks of the Michigan Basin, Southwest Ontario: Chemical Geology, v. 404, p. 1-17.

Al, T., Xiang, Y., Cavé, L., and Loomer, D., 2010, Measurement of diffusion properties by X-ray radiography and by through-diffusion techniques using iodide and tritium tracers: core samples from OS-1 and DGR-2, Technical Report TR-07-17 Revision 3, May 2010. Prepared by University of New Brunswick for Intera Engineering Ltd.

Altman, S. J., Peplinski, W. J., and Rivers, M. L., 2005, Evaluation of synchrotron X-ray computerized microtomography for the visualization of transport processes in low-porosity materials: Journal of Contaminant Hydrology, v. 78, no. 3, p. 167-183.

Altmann, S., Tournassat, C., Goutelard, F., Parneix, J.-C., Gimmi, T., and Maes, N., 2012, Diffusion-driven transport in clayrock formations: Applied Geochemistry, v. 27, no. 2, p. 463-478.

Appelo, C., Van Loon, L., and Wersin, P., 2010, Multicomponent diffusion of a suite of tracers (HTO, Cl, Br, I, Na, Sr, Cs) in a single sample of Opalinus Clay: Geochimica et Cosmochimica Acta, v. 74, no. 4, p. 1201-1219.

Appelo, C. A. J., and Postma, D., 2004, Geochemistry, groundwater and pollution, CRC press.

Appelo, C. A. J., and Wersin, P., 2007, Multicomponent diffusion modeling in clay systems with application to the diffusion of tritium, iodide, and sodium in opalinus clay: Environmental science & technology, v. 41, no. 14, p. 5002-5007.

Armstrong, D. K., and Carter, T., 2006, An updated guide to the subsurface Paleozoic stratigraphy of southern Ontario, Ontario Geological Survey.

Armstrong, D. K., and Carter, T.,, 2010, The subsurface Paleozoic stratigraphy of southern Ontario, Ontario Geological Survey.

Ayscough , Burchill C. E., J., I. K., and Logan S. R., 1967, The Photochemical Oxidation of Aqueous Iodide Solutions, v. 44, p. 5.

Bostick, B. C., Vairavamurthy, M. A., Karthikeyan, K., and Chorover, J., 2002, Cesium adsorption on clay minerals: An EXAFS spectroscopic investigation: Environmental Science & Technology, v. 36, no. 12, p. 2670-2676.

Bradbury, M. H., and Baeyens, B., 2000, A generalised sorption model for the concentration dependent uptake of caesium by argillaceous rocks: Journal of Contaminant Hydrology, v. 42, no. 2-4, p. 141-163.

Bradbury, M. H., and Baeyens, B., 2011, Predictive sorption modelling of Ni (II), Co (II), Eu (IIII), Th (IV) and U (VI) on MX-80 bentonite and Opalinus Clay: A “bottom-up” approach: Applied Clay Science, v. 52, no. 1-2, p. 27-33.

Brogly, P., Martini, I., and Middleton, G., 1998, The Queenston Formation: shale-dominated, mixed terrigenous-carbonate deposits of Upper Ordovician, semiarid, muddy shores in Ontario, Canada: Canadian Journal of Earth Sciences, v. 35, no. 6, p. 702-719.

Cadle, R. D., and Huff, H., 1950, The oxidation of iodide to iodine by dilute solutions of organic peroxides: J Phys Colloid Chem, v. 54, no. 8, p. 1191-1195.

Cavé, L., Al, T., and Xiang, Y., 2009b, X-ray radiography techniques for measuring diffusive properties of sedimentary rocks. Nuclear Waste Management Organization: NWMO-TR-2009-03.

Cavé, L., Al, T., Xiang, Y., and Loomer, D., 2010, Investigations of diffusive transport processes in sedimentary rock: Nuclear Waste Management Organization Technical Report NWMO TR-2010-04.

Cave, L., Al, T., Xiang, Y., and Vilks, P., 2009a, A technique for estimating one-dimensional diffusion coefficients in low-permeability sedimentary rock using X-ray radiography: comparison with through-diffusion measurements: J Contam Hydrol, v. 103, no. 1-2, p. 1-12.

Clausnitzer, V., and Hopmans, J. W., 2000, Pore-scale measurements of solute breakthrough using microfocus X-ray computed tomography: Water Resources Research, v. 36, no. 8, p. 2067-2079.

Cnudde, V., and Boone, M. N., 2013, High-resolution X-ray computed tomography in geosciences: A review of the current technology and applications: Earth-Science Reviews, v. 123, p. 1-17.

Cormenzana, J. L., García-Gutiérrez, M., Missana, T., and Junghanns, Á., 2003, Simultaneous estimation of effective and apparent diffusion coefficients in compacted bentonite: Journal of Contaminant Hydrology, v. 61, no. 1-4, p. 63-72.

De Cannière, P., Moors, H., Lolivier, P., De Preter, P., and Put, M., 1996, Laboratory and in situ migration experiments in the Boom clay: EUR(Luxembourg).

Descostes, M., Blin, V., Bazer-Bachi, F., Meier, P., Grenut, B., Radwan, J., Schlegel, M., Buschaert, S., Coelho, D., and Tevissen, E., 2008, Diffusion of anionic species in Callovo-Oxfordian argillites and Oxfordian limestones (Meuse/Haute–Marne, France): Applied Geochemistry, v. 23, no. 4, p. 655-677.

Dobson , and Grossweiner 1964, Primary Processes in the Photo-Oxidation of Iodide Ion in Ethanol: Radiation Research Society, v. 23, p. 290-299.

Doherty, J., 2018, Model-Independent Parameter Estimation User Manual Part I: PEST, SENSAN and Global Optimisers: Watermark Numerical Computing. Haettu, v. 17, no. 03, p. 2019.

Durrant, C. B., Begg, J. D., Kersting, A. B., and Zavarin, M., 2018, Cesium sorption reversibility and kinetics on illite, montmorillonite, and kaolinite: Science of the Total Environment, v. 610, p. 511-520.

Dzene, L., Tertre, E., Hubert, F., and Ferrage, E., 2015, Nature of the sites involved in the process of cesium desorption from vermiculite: Journal of colloid and interface science, v. 455, p. 254-260.

Frohlich, D. R., Amayri, S., Drebert, J., Grolimund, D., Huth, J., Kaplan, U., Krause, J., and Reich, T., 2012, Speciation of Np(V) uptake by Opalinus Clay using synchrotron microbeam techniques: Anal Bioanal Chem, v. 404, no. 8, p. 2151-2162.

Fuller, A. J., Shaw, S., Peacock, C. L., Trivedi, D., Small, J. S., Abrahamsen, L. G., and Burke, I. T., 2014, Ionic strength and pH dependent multi-site sorption of Cs onto a micaceous aquifer sediment: Applied geochemistry, v. 40, p. 32-42.

Fuller, A. J., Shaw, S., Ward, M. B., Haigh, S. J., Mosselmans, J. F. W., Peacock, C. L., Stackhouse, S., Dent, A. J., Trivedi, D., and Burke, I. T., 2015, Caesium incorporation and retention in illite interlayers: Applied Clay Science, v. 108, p. 128-134.

Garcıa-Gutiérrez, M., Missana, T., Mingarro, M., Samper, J., Dai, Z., and Molinero, J., 2001, Solute transport properties of compacted Ca-bentonite used in FEBEX project: Journal of Contaminant Hydrology, v. 47, no. 2-4, p. 127-137.

Harvie, C. E., Møller, N., and Weare, J. H., 1984, The prediction of mineral solubilities in natural waters: The Na-K-Mg-Ca-H-Cl-SO4-OH-HCO3-CO3-CO2-H2O system to high ionic strengths at 25 C: Geochimica et Cosmochimica Acta, v. 48, no. 4, p. 723-751.

Jackson, R., 2009, Organic geochemistry and clay mineralogy of DGR-3 and DGR-4 core. DGR site characterization document Intera Engineering project 08-200: Intera TR-08-29. Ottawa: Intera.

Jacobsen, C., Wirick, S., Flynn, G., and Zimba, C., 2000, Soft X-ray spectroscopy from image sequences with sub-100 nm spatial resolution: Journal of Microscopy, v. 197, no. 2, p. 173-184.

Jakob, A., Pfingsten, W., and Van Loon, L., 2009, Effects of sorption competition on caesium diffusion through compacted argillaceous rock: Geochimica et Cosmochimica Acta, v. 73, no. 9, p. 2441-2456.

Kasar, S., Kumar, S., Bajpai, R., and Tomar, B., 2016, Diffusion of Na (I), Cs (I), Sr (II) and Eu (III) in smectite rich natural clay: Journal of environmental radioactivity, v. 151, p. 218-223.

Kasar, S., Kumar, S., Saha, A., Tomar, B., and Bajpai, R., 2017, Mechanistic and thermodynamic aspects of Cs (I) and Sr (II) interactions with smectite-rich natural clay: Environmental Earth Sciences, v. 76, no. 7, p. 274.

Ketcham, R. A., 2005, Three-dimensional grain fabric measurements using high-resolution X-ray computed tomography: Journal of Structural Geology, v. 27, no. 7, p. 1217-1228.

Ketcham, R. A., and Carlson, W. D., 2001, Acquisition, optimization and interpretation of X-ray computed tomographic imagery: applications to the geosciences: Computers & Geosciences, v. 27, no. 4, p. 381-400.

Lauber, M., Baeyens, B., and Bradbury, M. H., 2000, Physico-Chemical Characterisation and Sorption Measurements of Cs, Sr, Ni, Eu, Th, Sn and Se on Opalinus Clay from Mont Terri: Paul Scherrer Inst.

Long, H., Wu, P., Yang, L., Huang, Z., Zhu, N., and Hu, Z., 2014, Efficient removal of cesium from aqueous solution with vermiculite of enhanced adsorption property through surface modification by ethylamine: Journal of colloid and interface science, v. 428, p. 295-301.

Loomer, D. B., Scott, L., Al, T. A., Mayer, K. U., and Bea, S., 2013, Diffusion–reaction studies in low permeability shale using X-ray radiography with cesium: Applied Geochemistry, v. 39, p. 49-58.

Maes, N., Salah, S., Jacques, D., Aertsens, M., Van Gompel, M., De Cannière, P., and Velitchkova, N., 2008, Retention of Cs in Boom Clay: comparison of data from batch sorption tests and diffusion experiments on intact clay cores: Physics and Chemistry of the Earth, Parts A/B/C, v. 33, p. S149-S155.

Mahoney, J. J., and Langmuir, D., 1991, Adsorption of Sr on kaolinite, illite and montmorillonite at high ionic strengths: Radiochimica Acta, v. 54, no. 3, p. 139-144.

Mayer, K. U., 1999, A numerical model for multicomponent reactive transport in variably saturated porous media.

Mayer, U., Xie, M., Su, D., and MacQuarrie, K., 2015, MIN3P-THCm, A Three-dimensional Numerical Model for Multicomponent Reactive Transport in Variably Saturated Porous Media: User Manual.

McMaster, W., Kerr Del Grande, N., Mallett, J., and Hubbell, J., 1970, Compilation of x-ray cross sections UCRL-50174, sections I, II revision 1, III, IV: Atomic Data and Nuclear Data Tables, v. 8, no. 4, p. 443-444.

Melkior, T., Yahiaoui, S., Motellier, S., Thoby, D., and Tevissen, E., 2005, Cesium sorption and diffusion in Bure mudrock samples: Applied Clay Science, v. 29, no. 3-4, p. 172-186.

Missana, T., Benedicto, A., García-Gutiérrez, M., and Alonso, U., 2014, Modeling cesium retention onto Na-, K-and Ca-smectite: Effects of ionic strength, exchange and competing cations on the determination of selectivity coefficients: Geochimica et Cosmochimica Acta, v. 128, p. 266-277.

Missana, T., Garcıa-Gutiérrez, M., and Alonso, U., 2004, Kinetics and irreversibility of cesium and uranium sorption onto bentonite colloids in a deep granitic environment: Applied Clay Science, v. 26, no. 1-4, p. 137-150.

Montavon, G., Alhajji, E., and Grambow, B., 2006, Study of the interaction of Ni2+ and Cs+ on MX-80 bentonite; Effect of compaction using the "capillary method": Environmental science & technology, v. 40, no. 15, p. 4672-4679.

Parkhurst, D. L., and Appelo, C., 1999, User's guide to PHREEQC (Version 2): A computer program for speciation, batch-reaction, one-dimensional transport, and inverse geochemical calculations: Water-resources investigations report, v. 99, no. 4259, p. 312.

Pitzer, K. S., and Kim, J. J., 1993, Thermodynamics of electrolytes.: IV. Activity and osmotic coefficients for mixed electrolytes, Molecular Structure And Statistical Thermodynamics: Selected Papers of Kenneth S Pitzer, World Scientific, p. 413-419.

Pitzer, K. S., and Mayorga, G., 1973, Thermodynamics of electrolytes. II. Activity and osmotic coefficients for strong electrolytes with one or both ions univalent: The Journal of Physical Chemistry, v. 77, no. 19, p. 2300-2308.

Reinoso-Maset, E., and Ly, J., 2014, Study of major ions sorption equilibria to characterize the ion exchange properties of kaolinite: Journal of Chemical & Engineering Data, v. 59, no. 12, p. 4000-4009.

Sardini, P., Delay, F., Hellmuth, K.-H., Porel, G., and Oila, E., 2003, Interpretation of out-diffusion experiments on crystalline rocks using random walk modeling: Journal of Contaminant Hydrology, v. 61, no. 1-4, p. 339-350.

Savoye, S., Beaucaire, C., Fayette, A., Herbette, M., and Coelho, D., 2012, Mobility of cesium through the Callovo-Oxfordian claystones under partially saturated conditions: Environ Sci Technol, v. 46, no. 5, p. 2633-2641.

Savoye, S. b., Page, J., Puente, C. l., Imbert, C., and Coelho, D., 2010, New experimental approach for studying diffusion through an intact and unsaturated medium: a case study with Callovo-Oxfordian argillite: Environmental science & technology, v. 44, no. 10, p. 3698-3704.

Siroux, B., Wissocq, A., Beaucaire, C., Latrille, C., Petcut, C., Calvaire, J., Tabarant, M., Benedetti, M. F., and Reiller, P. E., 2018, Adsorption of strontium and caesium onto an Na-illite and Na-illite/Na-smectite mixtures: Implementation and application of a multi-site ion-exchange model: Applied Geochemistry, v. 99, p. 65-74.

Smith, D., Pivonka, P., Jungnickel, C., and Fityus, S., 2004, Theoretical analysis of anion exclusion and diffusive transport through platy-clay soils: Transport in porous media, v. 57, no. 3, p. 251-277.

Soler, J. M., Wersin, P., and Leupin, O. X., 2013, Modeling of Cs+ diffusion and retention in the DI-A2 experiment (Mont Terri). Uncertainties in sorption and diffusion parameters: Applied Geochemistry, v. 33, p. 191-198.

Steefel, C. I., Carroll, S., Zhao, P., and Roberts, S., 2003, Cesium migration in Hanford sediment: a multisite cation exchange model based on laboratory transport experiments: Journal of Contaminant Hydrology, v. 67, no. 1-4, p. 219-246.

Tachi, Y., Yotsuji, K., Seida, Y., and Yui, M., 2011, Diffusion and sorption of Cs+, I− and HTO in samples of the argillaceous Wakkanai Formation from the Horonobe URL, Japan: Clay-based modeling approach: Geochimica et Cosmochimica Acta, v. 75, no. 22, p. 6742-6759.

Tachi, Y., Yotsuji, K., Seida, Y., and Yui, M., 2009, Diffusion of cesium and iodine in compacted sodium montmorillonite under different saline conditions: MRS Online Proceedings Library (OPL), v. 1193.

Takahashi, Y., Fan, Q., Suga, H., Tanaka, K., Sakaguchi, A., Takeichi, Y., Ono, K., Mase, K., Kato, K., and Kanivets, V. V., 2017, Comparison of Solid-Water Partitions of Radiocesium in River Waters in Fukushima and Chernobyl Areas: Sci Rep, v. 7, no. 1, p. 12407.

Tamura, T., and Jacobs, D., 1960, Structural implications in cesium sorption: Health physics, v. 2, no. 4, p. 391-398.

Taylor, J., 1997, Introduction to error analysis, the study of uncertainties in physical measurements.

Tevissen, E., Soler, J., Montarnal, P., Gautschi, A., and Van Loon, L. R., 2004, Comparison between in situ and laboratory diffusion studies of HTO and halides in Opalinus Clay from the Mont Terri: Radiochimica Acta, v. 92, no. 9-11, p. 781-786.

Thrippleton, M. J., Loening, N. M., and Keeler, J., 2003, A fast method for the measurement of diffusion coefficients: one-dimensional DOSY: Magnetic Resonance in Chemistry, v. 41, no. 6, p. 441-447.

Tidwell, V. C., and Glass, R. J., 1994, X ray and visible light transmission for laboratory measurement of two-dimensional saturation fields in thin-slab systems: Water Resources Research, v. 30, no. 11, p. 2873-2882.

Tidwell, V. C., Meigs, L. C., Christian-Frear, T., and Boney, C. M., 2000, Effects of spatially heterogeneous porosity on matrix diffusion as investigated by X-ray absorption imaging: Contaminant Hydrology, v. 42, p. 285-302.

Truesdale, V. W., 2007, On the feasibility of some photochemical reactions of iodide in seawater: Marine Chemistry, v. 104, no. 3-4, p. 266-281.

Van Loon, Baeyens, B., and Bradbury, M., 2009, The sorption behaviour of caesium on Opalinus Clay: a comparison between intact and crushed material: Applied Geochemistry, v. 24, no. 5, p. 999-1004.

Van Loon, Glaus, M. A., and Müller, W., 2007, Anion exclusion effects in compacted bentonites: towards a better understanding of anion diffusion: Applied Geochemistry, v. 22, no. 11, p. 2536-2552.

Van Loon, Soler, J., and Bradbury, M., 2003, Diffusion of HTO, 36Cl− and 125I− in Opalinus Clay samples from Mont Terri: Effect of confining pressure: Journal of Contaminant Hydrology, v. 61, no. 1-4, p. 73-83.

Van Loon, L. R., Wersin, P., Soler, J., Eikenberg, J., Gimmi, T., Hernan, P., Dewonck, S., and Savoye, S., 2004, In-situ diffusion of HTO, 22Na+, Cs+ and I- in Opalinus Clay at the Mont Terri underground rock laboratory: Radiochimica Acta, v. 92, no. 9-11, p. 757-763.

Vilks, Cramer, J. J., Jensen, M., Miller, N. H., Miller, H. G., and Stanchell, F. W., 2007, In situ diffusion experiment in granite: Phase I: Journal of Contaminant Hydrology, v. 61, no. 1-4, p. 191-202.

Wersin, P., Soler, J., Van Loon, L., Eikenberg, J., Baeyens, B., Grolimund, D., Gimmi, T., and Dewonck, S., 2008, Diffusion of HTO, Br−, I−, Cs+, 85Sr2+ and 60Co2+ in a clay formation: Results and modelling from an in situ experiment in Opalinus Clay: Applied Geochemistry, v. 23, no. 4, p. 678-691.

Wersin, P., Van Loon, L., Soler, J., Yllera, A., Eikenberg, J., Gimmi, T., Hernán, P., and Boisson, J.-Y., 2004, Long-term diffusion experiment at Mont Terri: first results from field and laboratory data: Applied Clay Science, v. 26, no. 1-4, p. 123-135.

Wigger, C., Kennell-Morrison, L., Jensen, M., Glaus, M., and Van Loon, L., 2018, A comparative anion diffusion study on different argillaceous, low permeability sedimentary rocks with various pore waters: Applied Geochemistry, v. 92, p. 157-165.

Wildenschild, D., Vaz, C., Rivers, M., Rikard, D., and Christensen, B., 2002, Using X-ray computed tomography in hydrology: systems, resolutions, and limitations: Journal of Hydrology, v. 267, no. 3-4, p. 285-297.

Xiang , Diana Loomer, and Al, T., 2016, Improvements in Methodologies for Radiographic Measurement of Diffusion Properties in Low-permeability Rocks, and Development of Methods for pH Measurement in Brines Nuclear Waste Management Organization.

Xiang, Y., Al, T., and Mazurek, M., 2016, Effect of confining pressure on diffusion coefficients in clay-rich, low-permeability sedimentary rocks: J Contam Hydrol, v. 195, p. 1-10.

Xiang, Y., Al, T., Scott, L., and Loomer, D., 2013, Diffusive anisotropy in low-permeability Ordovician sedimentary rocks from the Michigan Basin in southwest Ontario: J Contam Hydrol, v. 155, p. 31-45.

Xie , Rasouli P, Mayer K U, and B, M. T., 2015, MIN3P-THCm Code Enhancements for Reactive Transport Modelling in Low Permeability Media, NWMO-TR-2015-12.

Yankovich, T. L., and Swainson, I., 2000, Methodology for analyzing weak spectra: Atomic Energy of Canada Limited.

Zachara, J. M., Smith, S. C., Liu, C., McKinley, J. P., Serne, R. J., and Gassman, P. L., 2002, Sorption of Cs+ to micaceous subsurface sediments from the Hanford site, USA: Geochimica et cosmochimica Acta, v. 66, no. 2, p. 193-211.

Chapter 3 – Conclusion

This study demonstrated that the novel X-ray absorption technique, XAS, is effectively able to investigate the conservative (I^-) and reactive (Cs^+) solute transport properties such as D_{e-I} , D_{e-Cs} , and CEC. The method is based on measuring time-series solute transport diffusion within the different section of the sample. The solute transport concentration in each section of the sample was quantified by absorption k-edge energy of the $I^-$and Cs^+. XAS method provides a means of measuring changes in X-ray intensity ($\Delta\mu$) to generate relative concentration profile of the solute transport as a function of transport distance at each time step to calculate D_{p-I} , D_{p-Cs} , and CEC. The analytical solution of Fick's Second Law was applied to fit the experimental and analytical relative iodide concentration profiles to calculate D_{p-I} and then D_{e-I}. However, A multi-site ion exchange model was run to provide analytical time-series profiles to quantify D_{p-Cs} ,CEC , and D_{e-Cs}. Comparison of the iodide results obtained from this study are in good agreement with the other results made by radiography and through diffusion experiments through different argillaceous rocks.

A comparison of the D_{p-Cs} and D_{e-Cs}values obtained in this study with other diffusion coefficients reported in the literature indicated that the diffusion values of Queenston shale are relatively lower than other argillaceous rocks. The low cesium values of CEC within Queenstone shale relative to the other argillaceous rocks indicate less accessible clay minerals for sorption of the reactive solute transport. Furthermore, the effective diffusion pathways and the less accessible clay content affect CEC values are consistent with the SEM-SE images demonstrate the intergranular void spaces in the shale containing clay minerals. In general, the values determined by this method can be representative of host rocks for radioactive waste repositories.

Another worthwhile outcome of this study is the elimination of the beam hardening effect, which is seen in radiography method that contributes to calibration method.

3.1. Further recommendation

The results of this study successfully demonstrate that the XAS technique can be taken into consideration as an alternative non-destructive X-ray method and it can be used for the quantitative measurement of diffusion properties of low-permeability rocks.

The following suggestions for future research directions:

1- The XAS method has been tested on low- permeability rock samples, including

of Queenston Formation shale; The method can be used to spatially resolve tracer concentrations through other types of rock like crystalline rock samples (e.g., granite) for measurement of the diffusion properties.

2- This work uses a one-dimensional MIE approach to quantify diffusion and sorption properties. Upgrading the reactive-transport model from 1-D to 2D and 3-D and assessing the diffusion/reaction parameters ,D_p and cation exchange capacity (CEC), is recommended in future work. It may provide more information for diffusion/sorption of the reactive tracer through the rock samples which is likely to give a clear view of the solute transport through the geological system.

3- This work investigated the diffusion of Cs^+ and I^- species via the XAS method. Study of Diffusion and sorption behaviors of other anionic tracers such as Cl^-, Br^-, and reactive tracers (e.g., Rb^+, Sr^{+2}, Tl^+) can provide more information on whether they have favorable X-ray absorption characteristics with this method.

4- It is true that the XAS method minimize the Beam hardening effect, the difference in slopes between two materials –plastic and ceramics vials- for Cs^+ needs to be more investigated with more experiments and different materials with less absorbency.

5- The XAS measurements were conducted with a 1 M tracer solution to determine diffusion properties. Using a wide range of tracer solution concentrations is recommended to verify the limit of detection of the XAS method for diffusion measurements.

Appendix A

A.1.1. Phreeqc Simulation

A.1.1.1. Phreeqc Input File for the Sample Being Saturated with Iodide from Either Side

Modelling simulation using PHREEQC whateq database indicated the required time to reach a fully saturated sample form both side is approximately 45 days. For the simulation the diffusion domain was divided into 40 cells along the sample with 20mm in length. The cells ranging from 1 to 39 were initially filled with SPW and the diffusion-only transport was initiated by introducing 1M iodide tracer into influx boundaries. Two influx boundaries on either side of the domain was imposed constant.

The following is an example of a PHREEQC input file used for calculation the time is required the sample to be fully saturated from either side.

```
SOLUTION 1-39 spw
    temp      25
    pH        7
    pe        4
    redox     pe
    units     mol/l
    density   1.22
    Cl        5.8
    K         0.5
    Mg        0.25
    Na        2.4
    Ca        1.2
    S(6)      0.001
    -water    1 # kg

SOLUTION 0 IODIDE TRACER
    temp      25
    pH        7
    pe        4
    redox     pe
    units     mol/l
    density   1
    Ca        1.2
```

```
    Cl        4.8
    K         0.5
    Mg        0.25
    Na        2.4
    S(6)      0.001
    I         1.0
    -water    1 # kg

SOLUTION 40 IODIDE TRACER
    temp      25
    pH        7
    pe        4
    redox     pe
    units     mol/l
    density   1
    Ca        1.2
    Cl        4.8
    K         0.5
    Mg        0.25
    Na        2.4
    S(6)      0.001
    I         1.0
    -water    1 # kg

TRANSPORT
    -cells                 40
    -shifts                110
    -time_step             36000 # seconds
    -flow_direction        diffusion_only
    -boundary_conditions   constant constant
    -lengths               0.0005
    -dispersivities        0
    -diffusion_coefficient 4.2e-11
    -thermal_diffusion     2   4.2e-11
    -print_cells           2-40
    -punch_cells           2-40
    -punch_frequency       2




SELECTED_OUTPUT 1
    -file                 D:\ottawa university\Tom
Al\homework\5\saturation.sel
    -totals                        I

end
```

Appendix B

B.2.1. Spectroscopy Measurements

The field of view (FOV) of the X-ray beam was collimated in order to optimize the spatial resolution and the change of diffusing species in each cross section of the sample; diffusion pathway. Recorded tests proved that the optimal FOV size, the more spatial resolution there is for resolving the concentration of diffusing species within the sample. Before diffusion experiments, some effective parameters on spatial resolution such as focal spot size, inner diameter, length of collimator, aperture diameter, sample to collimator distance and finally focal spot to collimator distance have been examined.

B.2.1.1. Calculation of Field of View

In spectroscopy measurements, resolving the tracer presence within the sample is usually highly important and depends on the high spatial resolution which is a function of field of view (Fig. B.1). It is known that as the number of measurement gets more precise, which is affected by smaller field of view, the spatial resolution for the mass of tracer will go higher. An array of measurements mentioned above such as the length of the collimator, collimator inner diameter, sample to end of the collimator distance, focal spot to collimator distance, focal spot size, and aperture size should be taken into account for evaluation of X-ray field of view (FOV) (tablebB.1). Moreover, the FOV was calculated based on the mentioned geometric characteristics.

$$tan\alpha = \frac{\left(\frac{d_2}{2}\right) + \left(\frac{d_4}{2}\right)}{d_3} =$$

$$tan\alpha = \frac{\frac{d_2}{2}}{x} =$$

$$\frac{\left(\frac{d_2}{2}\right)}{fov/2} = \frac{x}{x + d_1}$$

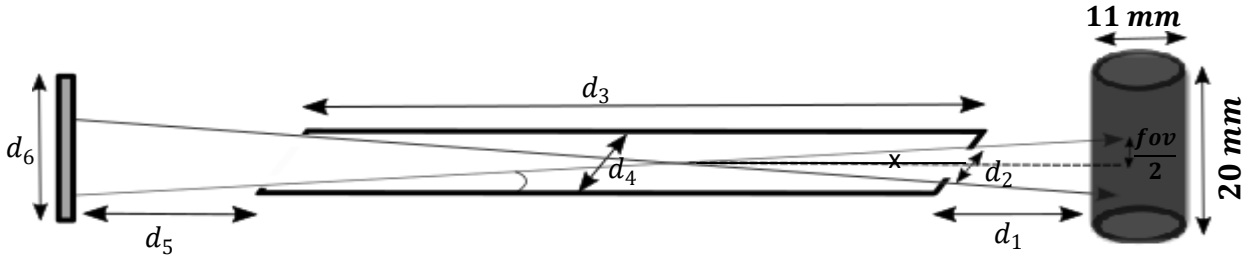

Figure B.1. Schematic diagram indicating the field of view

Table B.1. Acquisition parameters for collimated X-ray beam to optimize FOV

Parameters	**Setting (mm)**
$Sample\ to\ collimator\ distance(d_1)$	30
Aperture diameter(d_2)	1
$Calimator\ lemgth\ (d_3)$	318
$Calimator\ ID(d_4)$	2.1336
$Focal\ spot\ to\ collimator\ tip\ distance(d_{5)}$	48
$Focal\ spot\ (d_6)$	5.5
Spatial resolution (FOV)	1.1

The effectiveness X-ray source measurements is associated with the focal spot, X-ray intensity, and generated X-ray energies spectrum (Fitzgerald, 1947; Ketcham and Carlson, 2001). Focal spot size influences the number of possible X-ray source to detector paths that can intersect a given point- between the object and focal spot. The size of the X-ray tube focal-spot and the magnification factors (M, source-to-detector distances to the source-to-specimen distance), are used to determine the geometric sharpness or blur of the setup (Fig. B.2). Geometric sharpness or the size of the penumbra (UG) is provided by the following equation (Gebureck et al., 1989):

$$UG = f * \frac{b}{a}$$

where:

f = X-ray generator focal-spot size.
a = distance from x-ray source to front surface of object
b = distance from the object to the detector.

When the object is placed as close to the detector as possible, magnification is not needed, and therefore the source is placed some distance from the object minimizing the penumbra. A greater distance between the source and the object will increase the resolution/ clarity. However, the intensity of the source decreases with distance. Therefore, the source should only be placed as far away as necessary to control the penumbra. If the object is placed in direct contact with the detector (as is often done in radiograph) the following formula can be used, which takes into account, the material thickness instead of the object-to-detector distance:

$$UG = f * \frac{t}{d}$$

where:

f = X-ray generator focal spot size
t = the thickness of the material
d = distance from x-ray source to front surface of object.

The X-ray attenuation rate and penetrative ability is defined by the energy spectrum. Higher-energy spectra are less sensitive to changes in density and material composition, while penetrating more than lower-energy spectra.

However, X-ray current controls the photon count effecting the signal to noise ratio. A better signal results in better counting statistics since photon count is inversely proportional to noise; Noise= $\frac{1}{\sqrt{counts}}$.

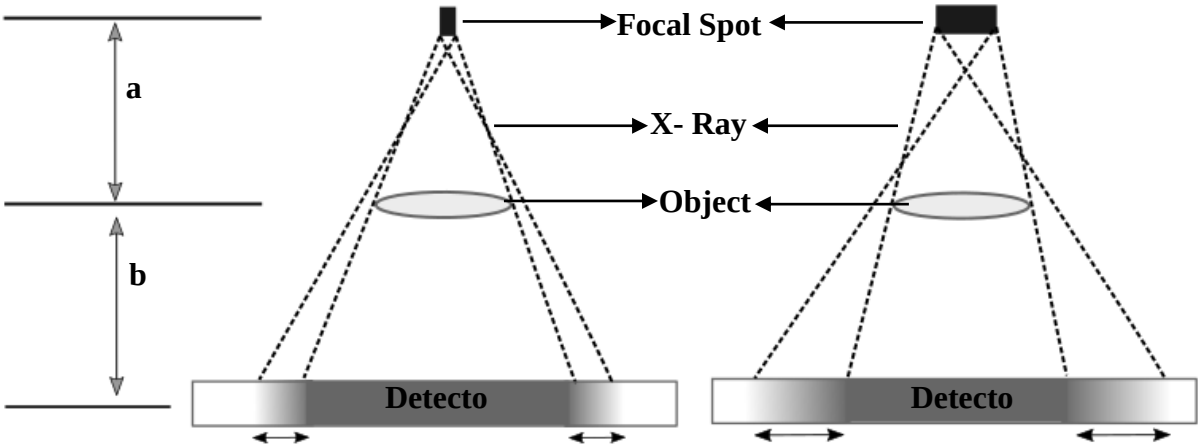

Figure B.2. Geometric blur (black arrows); increasing focal spot size (shown) and increasing magnification (not shown) increases the sharpness at the edge of the object's projected image

B.2.1.2. Determination of Sample Position Spatial Resolution Measurement

The smallest feature that can be distinctively resolved within the spectra is defined as the spatial resolution (SR) of the spectra. The technique that is used to measure the SR as well as sample position was the application of two distinct materials with a discrete count rate, using lead tape on either side of the sample in the experiment. The SR and base sample position were measured by moving the sample to different position on the diffusion axis. This includes taking a profile across the boundary of two markedly contrasting materials on either sides. The intensity value of the sample to lead tape as function of the stage position was measured and plotted (Fig. B.3a). The given line profile illustrates the information on sample top, sample base, and the transitional area between sample and lead tape to assess the SR. SR is determined by analyzing the line profile, which is calculated by subtracting the sample top value from sample base value in terms of stage position:

$$SR(mm) = \frac{upper\ infelction\ value(units) - lower\ infelction(units)}{200(units)}$$

It is worth mentioning that, the moving stage position combined with the program (X-spec) (relies on) is in units, and each 200 units equal with 1mm. In addition, there should be a lateral motion of the stage to find the horizontal midpoint in sample to adjust the transmitted beam from the collimator (Fig. B.3b). In accordance with Beer's law associated with sample thickness, the lowest intensity indicates the middle point of sample laterally. In addition, the total number of steps which is necessary for scanning the whole sample through the experiment is obtained from the following equation:

$$Number\ of\ steps = \frac{length\ of\ sample(mm)}{SR(mm)}$$

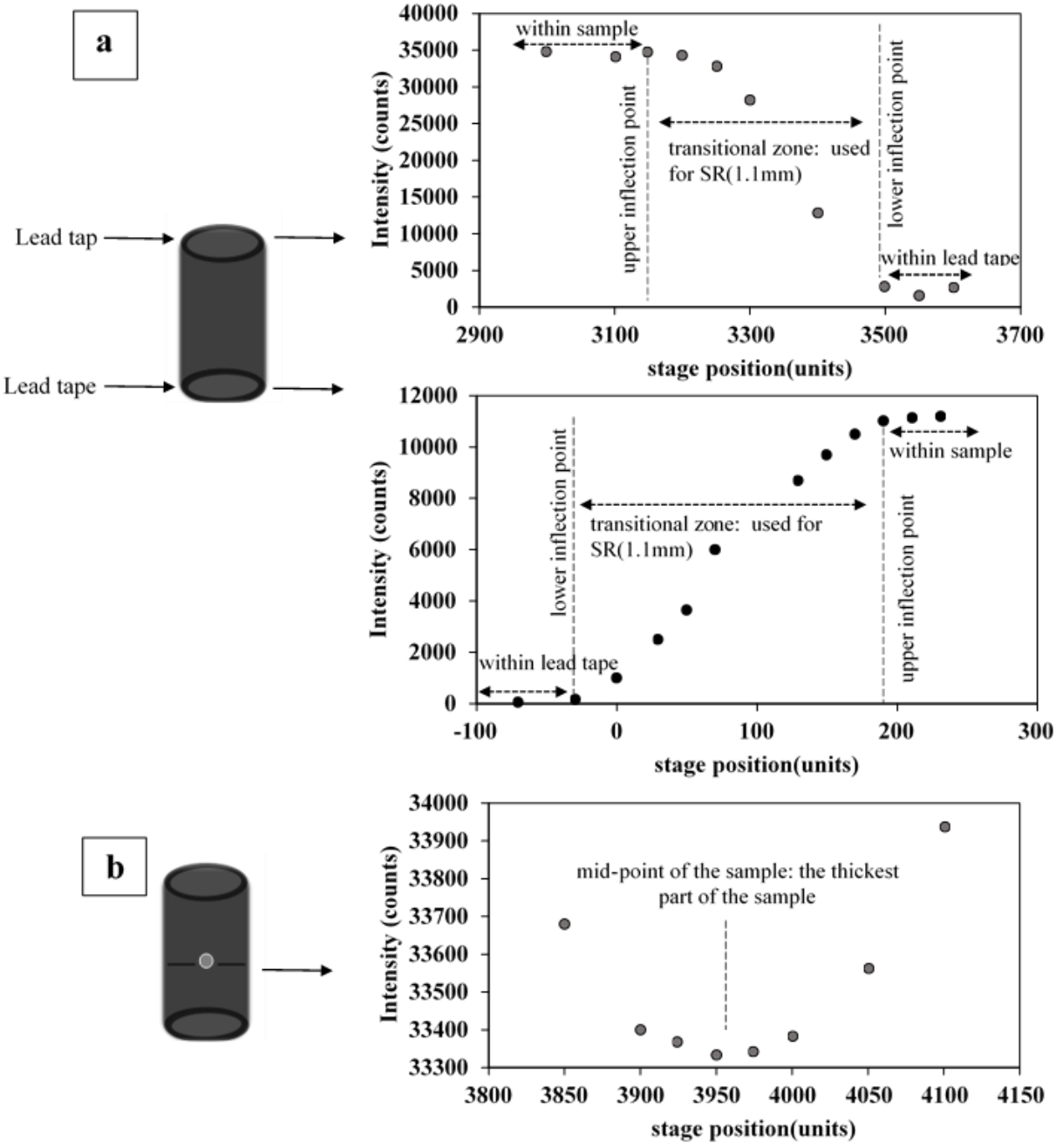

Figure B.3. a) A line profile across the sample and lead tape on either side of the sample to determine the spatial resolution and sample position for diffusion experiment, b) A line profile for determining the lateral mid-point of the sample for diffusion experiment

B.2.2. References

Fitzgerald, G., 1947, An Investigation in Adumbration, or the Factors that Control Geometric Unsharpness: J. Am. Dent. Assoc, v. 34, p. 1-20.

Gebureck, P., Petermann, D., and Stegemann, D., 1989, Determination of the focal spot size of microfocus X-ray sources, Non-Destructive Testing, Elsevier, p. 42-47.

Ketcham, R. A., and Carlson, W. D., 2001, Acquisition, optimization and interpretation of X-ray computed tomographic imagery: applications to the geosciences: Computers & Geosciences, v. 27, no. 4, p. 381-400.

Appendix C

C.3.1. Energy Calibration

Energy calibration, converting the channel of numbers into the energy range of a system, is critical for the quantitative X-ray analysis. Before beginning to calibrate the energy scale, adjusting the DPP gain of the amplifier, which indicates the spectroscopy range or energy scale range. For amplifier's gain adjusting, system conversion gain expressed in unit of eV/channel is a key parameter, because it denotes the DppMCA channel number in which a particular energy peak will occur. Typical values for the conversion of gain given by dividing the number of channel in the output spectrum over the voltage corresponding to the peak channel is approximately 20 eV/channel considering 2048 channels containing a range of 45keV. Another key parameter is the "offset", the channel corresponding to zero energy. Ideally, the offset would be zero and the gain exactly equal to a convenient value (There is, in general, a non-zero offset to the spectrum). Subsequently, the fast and slow thresholds relating to the incoming count rate should be tuned on. The purpose of this step is to ensure that the DppMCA can acquire spectra properly before starting the calibration procedure. Based on the X-ray energies for the Cs and I experiment, the digital pulse processor was optimized using the parameters in table C. 1. Once the appropriate gain (full scale energy) and threshold was found the software was calibrated to change the channel scale into an energy scale. To accurately calibrate a spectrum, we used the strong and widely-easily separated photo peaks in the spectrum acquired by a PbSn known alloy. Herein, The Pb Lβ and Sn kα were used for energy calibration. Once the calibration was conducted, the XAS experiment was started.

Table C. 1. Acquisition parameters for DppMCA Configuration

Configuration parameters	Setting	
	Cs^+	I^-
Gain	26.77	29.79
Channel number	2048	2048
Full energy range (KeV)	0-45	0-41
Fast threshold	30	30
Slow threshold	1.79	1.79
Conversion gain (eV/channel)	21	20
Peak time (µs)	6.4	6.4
Offset	-0.11	-0.15

C.3.2. Converting Channel to Energy Scale

When performing X-ray analysis, since the measured spectra are based on channels, it is important to calibrate the spectra in terms of energy conducted by DDPMCA. The following steps should be followed (Fig. C.1):

- Choose two peaks with a known voltage energy. A pure sample and/or specified alloy with two known, strong, widely separated photopeaks should be selected to calibrate the scale in DPPMCA.
- Identify a region of interest (ROI) for each peak based on the spectrum pattern from the known samples.

- Select the calibration button in the software. In the calibration window, the channel number of each known strong spectrum is shown for converting into energy value.
- Select the first peak and enter the channel number and voltage energy based on the spectrum pattern. Then repeat the same step for the other peak.
- Click Ok. The scale should be displayed as energy scale.

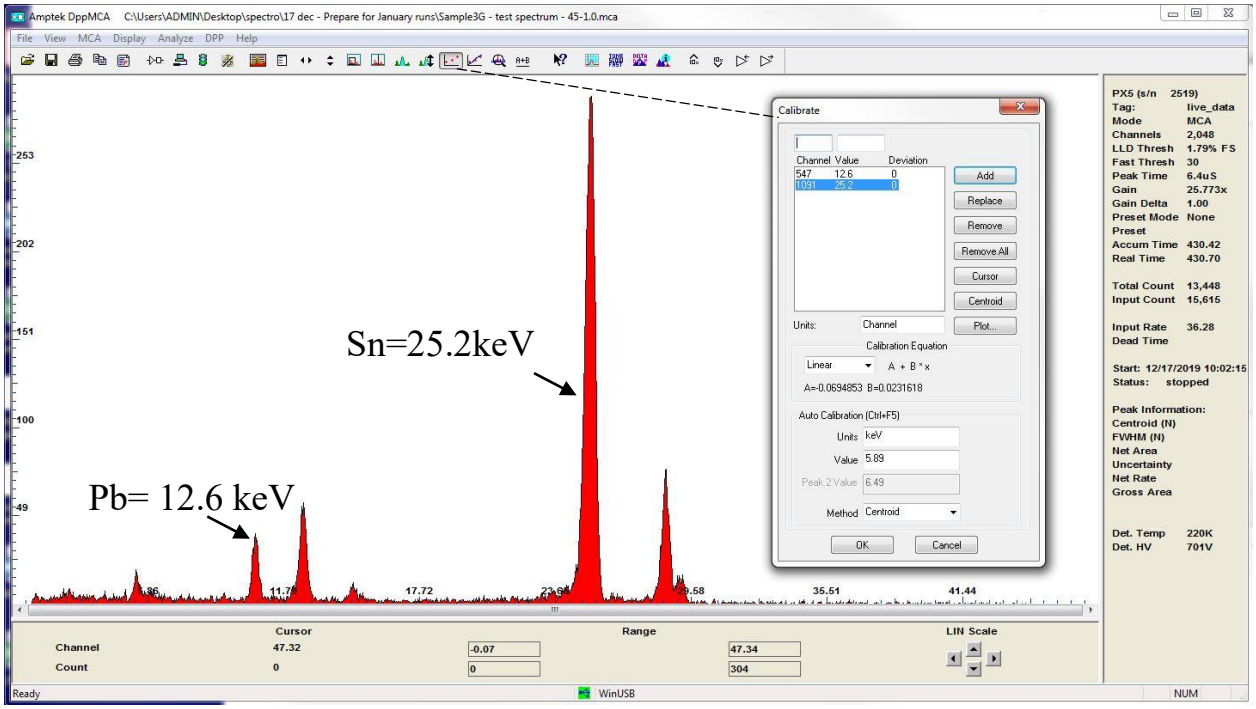

Figure C.1. Energy calibration procedure in DPPMCA software with Sn:Pb alloy

Appendix D

D.4.1. Diffusion Measurements Results

For diffusion experiment, small cylindrical samples oriented normal to bedding plane were drilled via diamond core bit to drill. Three of the five samples from the same slice were used for diffusion experiments with an I^- tracer .The remaining three were used for diffusion-reaction measurements made by monitoring behavior of Cs^+. The off-cuts from main sliced rocks were used for water accessible porosity (ϕ_w) measurement. A value of the bulk porosity of the sample determined with Gravimetric measurements (Emerson, 1990) of water-accessible porosity (ϕ_w) were used for comparison with iodide-accessible porosity (ϕ_I) obtained from spectroscopy method. The diffusive reactive modelling were applied for reactive tracer, Cs^+, using water-accessible porosity.

D.4.1.1. Diffusion Experiment Using Iodide Tracer

The diffusion coefficients obtained by spectroscopy method at multiple- time steps indicated in table D. 1-.3. The values D_e derived from fitting the experimental data to the analytical model for each sample are indicated in tables below. The decrease in D_e is partially accounted for by the loss of iodide-accessible porosity and/or might be related to heterogeneity (Al et al., 2010; Nunn et al., 2018). Comparison of the water-accessible porosity with the iodide-accessible porosity indicated iodide-accessible porosity (table D.1-.3) from spectroscopy measurement in shale samples was typically 63.3% of the water-loss value, consistent with relatively high clay content and anion exclusion theory (Smith et al., 2004).The time-series profiles for relative iodide concentrations (C/C_0) calculated from $\Delta\mu$ in the porewater-saturated Queenston shale sample are displayed in Fig. D1- D 3.

Table D.1. Iodide diffusion coefficients for Queenston shale sample DGR3a

Sample ID DGR3a	$\boldsymbol{\phi_w}$ **0.0989**	$\boldsymbol{\phi_I}$ **0.0636**
Time step(hrs)	$\mathbf{D_p\ (m^2s^-)}$	$\mathbf{D_e(m^2s^-)}$
7	8.9×10^{-12}	5.66×10^{-13}
24	2.1×10^{-11}	8.27×10^{-13}
48	2.8×10^{-11}	1.78×10^{-12}
72	3.2×10^{-11}	2.04×10^{-12}
96	4.2×10^{-11}	2.67×10^{-12}
168	4.2×10^{-11}	2.67×10^{-12}
Average(48-168 hrs)	$3.70\times 10^{-11} \pm 0.62$	2.35×10^{-12}

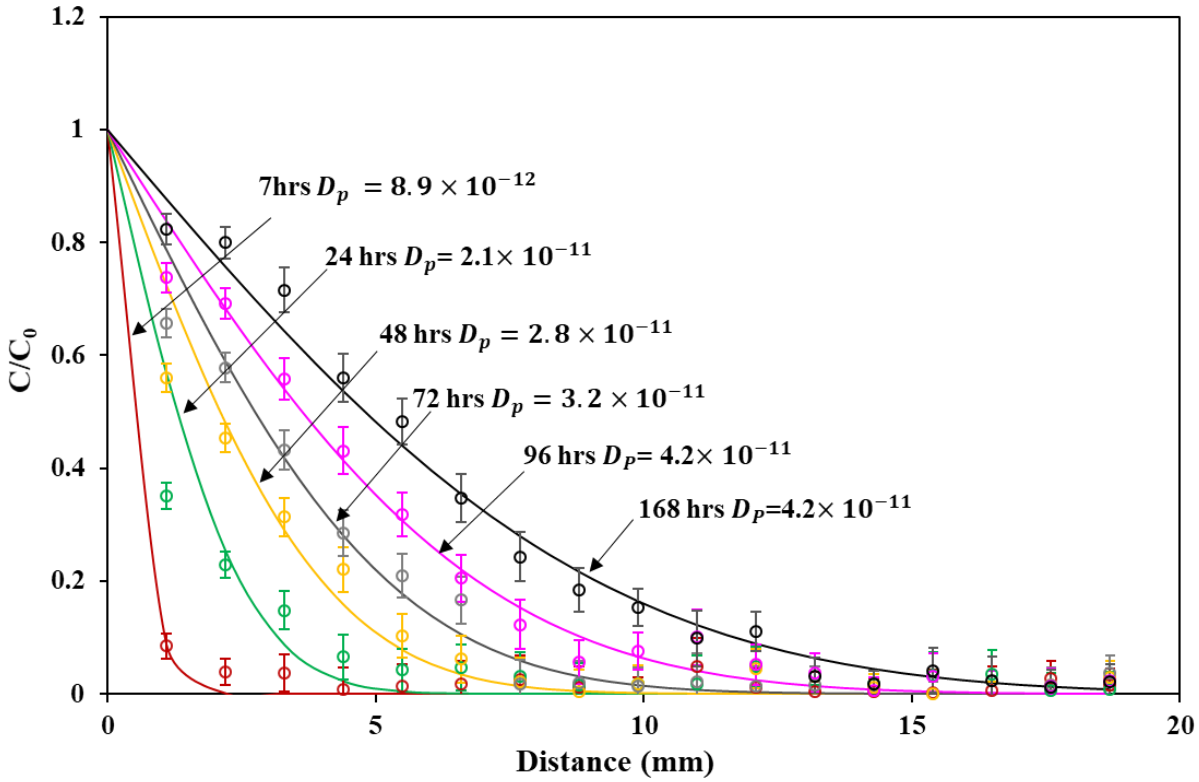

Figure D.1. Iodide concentration profiles and analytical diffusion profiles of sample dgr3a, the vertical error bars reflect propagation of error as described in section 2.2.10.2

Table D.2. Iodide diffusion coefficients for Queenston shale sample DGR3b

Sample ID DGR3b	ϕ_w **0.0989**	ϕ_I **0.0597**
Time step(hrs)	$D_p(m^2s^-)$	$D_e(m^2s^-)$
7	1.4×10^{-11}	8.36×10^{-13}
24	2.2×10^{-11}	1.31×10^{-12}
48	2.1×10^{-11}	1.25×10^{-12}
72	2.3×10^{-11}	1.37×10^{-12}
96	2.4×10^{-11}	1.43×10^{-12}
168	2.8×10^{-11}	1.67×10^{-12}
Average(24-168 hrs)	$2.36\times 10^{-11} \pm 0.22$	1.43×10^{-12}

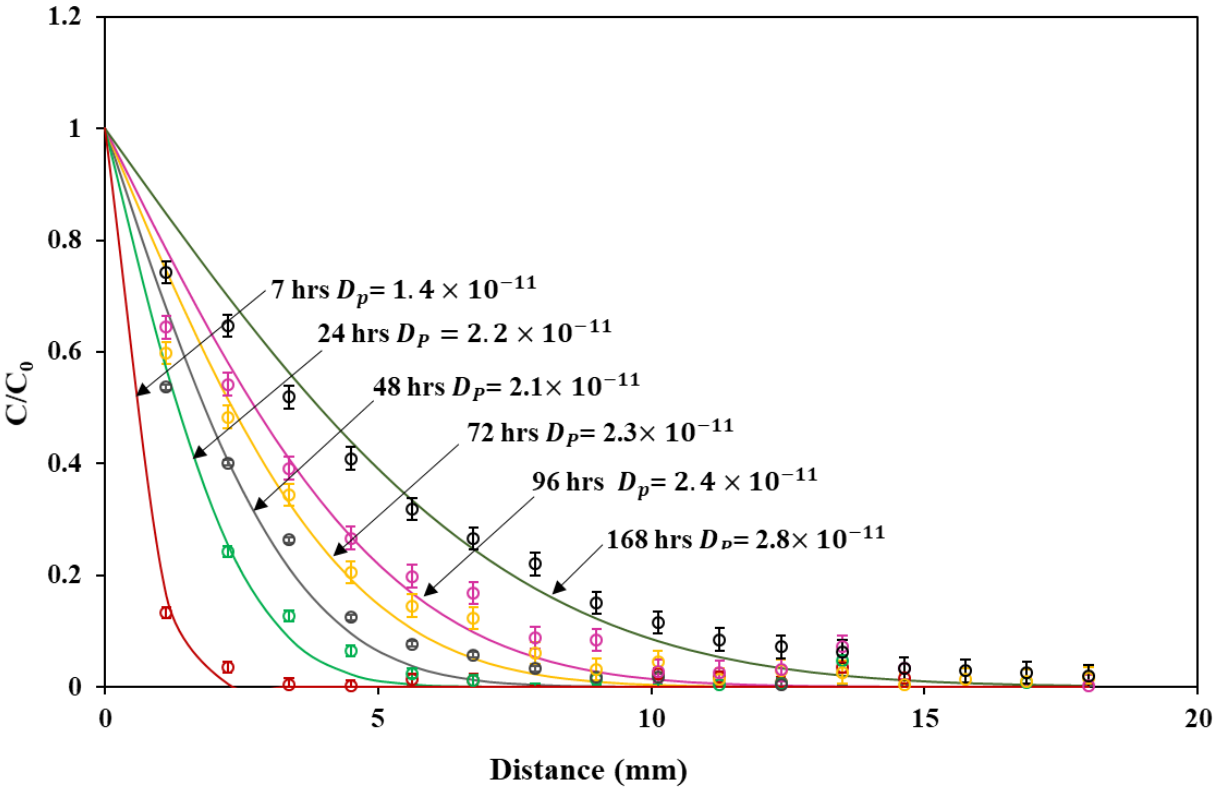

Figure D.2. Iodide concentration profiles and analytical diffusion profiles of sample dgr3b, the vertical error bars reflect propagation of error as described in section 2.2.10.2

Table D.3. Iodide diffusion coefficients for Queenston shale sample DGR3e

Sample ID DGR3e	ϕ_w **0.0989**	ϕ_I **0.0618**
Time step(hrs)	$D_p(m^2s^-)$	$D_e(m^2s^-)$
19	4.5×10^{-11}	2.78×10^{-12}
26	2.5×10^{-11}	1.54×10^{-12}
50	2.7×10^{-11}	1.67×10^{-12}
140	5.5×10^{-11}	3.40×10^{-12}
142	4.6×10^{-11}	2.84×10^{-12}
Average(19-142 hrs)	$3.96\times 10^{-11} \pm 1.32$	2.45×10^{-12}

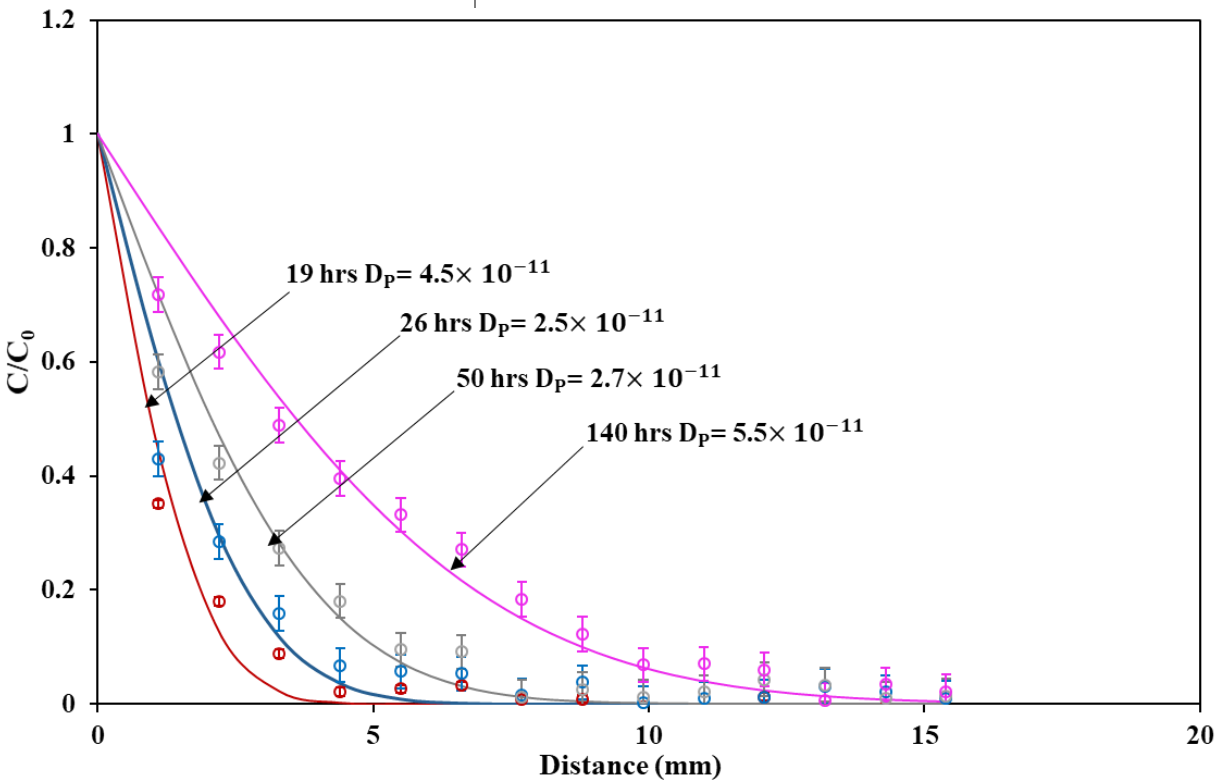

Figure D.3. Iodide concentration profiles and analytical diffusion profiles of sample dgr3e, the vertical error bars reflect propagation of error as described in section 2.2.10.2.

D.4.1.2. Diffusion Experiment Using Cesium Tracer

The reactive –transport modelling was used to estimate diffusion and sorption parameters affecting Cs^+ transport with the shale samples. The D_{p-Cs} , D_{e-Cs} and CEC derived from fitting the experimental data to the analytical model for each sample are indicated in figures below. The increase in D_{e-Cs} is accounted for by the larger diffusivities for the cation which is consistent with cation excess and anion exclusion effects. Comparison of the D_{e-Cs} with the D_{e-I} indicated anion exclusion mechanism for ionic species. The time-series profiles for relative cesium concentrations (C/C_0) calculated from Δμ in the porewater-saturated Queenston shale sample are displayed in Fig. D4- D 6.

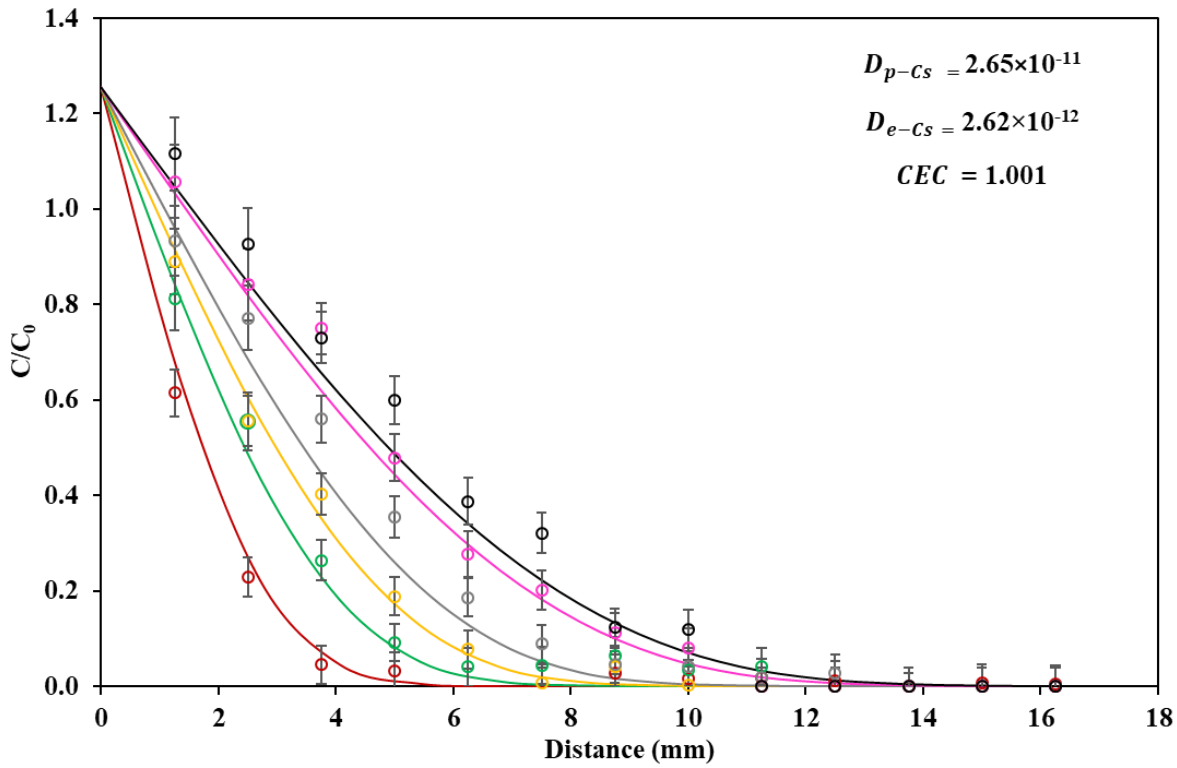

Figure D.4. Relative Cs^+concentration profiles and simulated diffusion-reaction model profiles (thin lines) for Dgr3c, the vertical error bars reflect propagation of error as described in section 2.2.10.2.

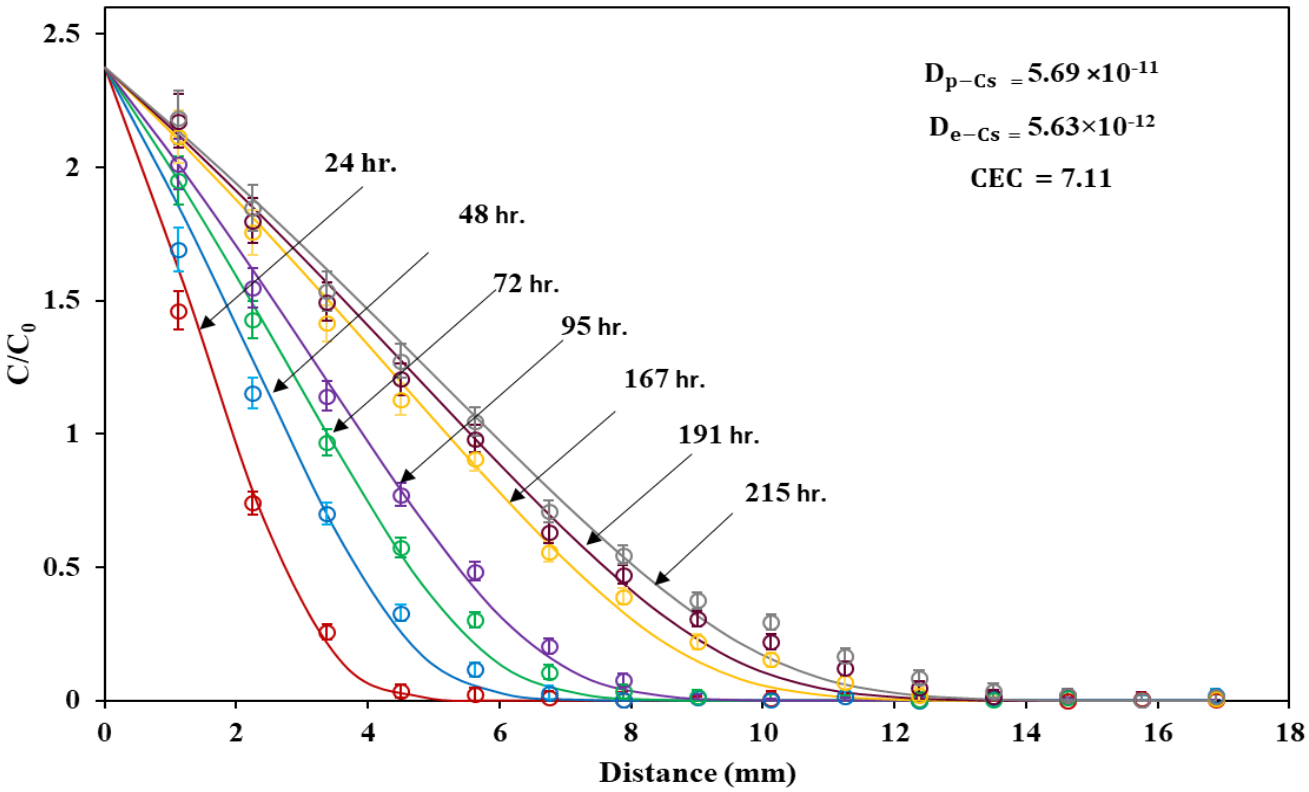

Figure D.5. Relative Cs^{+}concentration profiles and simulated diffusion-reaction model profiles (thin lines) for Dgr3g, the vertical error bars reflect propagation of error as described in section 2.2.10.2.

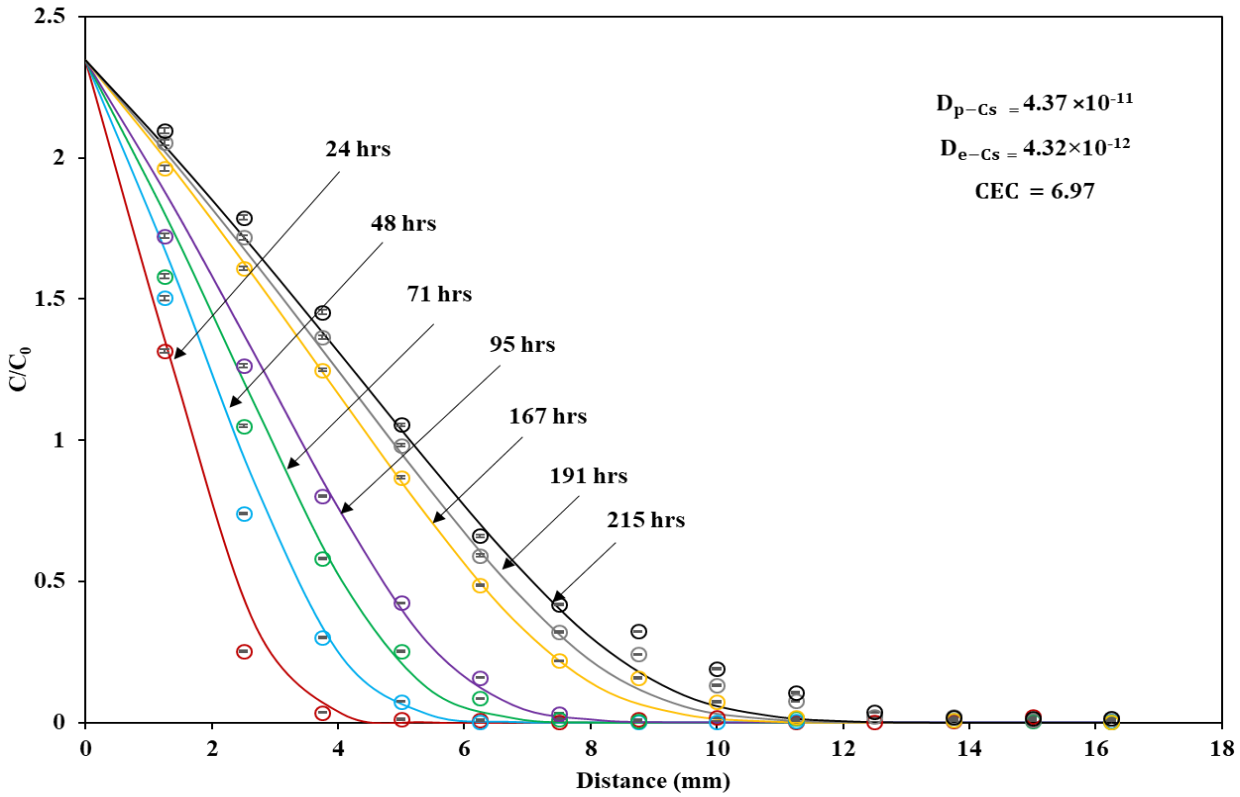

Figure D.6. Relative Cs^{+}concentration profiles and simulated diffusion-reaction model profiles (thin lines) for Dgr3j, the vertical error bars reflect propagation of error as described in section 2.2.10.2.

D.4.2. References

Al, T., Xiang, Y., Cavé, L., and Loomer, D., 2010, Measurement of diffusion properties by X-ray radiography and by through-diffusion techniques using iodide and tritium tracers: core samples from OS-1 and DGR-2, Technical Report TR-07-17 Revision 3, May 2010. Prepared by University of New Brunswick for Intera Engineering Ltd.

Emerson, D., 1990, Notes on mass properties of rocks? density, porosity, permeability: Exploration geophysics, v. 21, no. 4, p. 209-216.

Fitzgerald, G., 1947, An Investigation in Adumbration, or the Factors that Control Geometric Unsharpness: J. Am. Dent. Assoc, v. 34, p. 1-20.

Gebureck, P., Petermann, D., and Stegemann, D., 1989, Determination of the focal spot size of microfocus X-ray sources, Non-Destructive Testing, Elsevier, p. 42-47.

Ketcham, R. A., and Carlson, W. D., 2001, Acquisition, optimization and interpretation of X-ray computed tomographic imagery: applications to the geosciences: Computers & Geosciences, v. 27, no. 4, p. 381-400.

Nunn, J. A., Xiang, Y., and Al, T. A., 2018, Investigation of partial water saturation effects on diffusion in shale: Applied Geochemistry, v. 97, p. 93-101.

Smith, D., Pivonka, P., Jungnickel, C., and Fityus, S., 2004, Theoretical analysis of anion exclusion and diffusive transport through platy-clay soils: Transport in porous media, v. 57, no. 3, p. 251-277.